Improved Dynamic Modeling and Robust Control of Autonomous Underwater Vehicles

Scott B. Gibson

Dissertation submitted to the Faculty of the
Virginia Polytechnic Institute and State University
in partial fulfillment of the requirements for the degree of

Doctor of Philosophy
in
Electrical Engineering

Daniel J. Stilwell, Chair
Stefano Brizzolara
Allen B. MacKenzie
Pratap Tokekar
Craig A. Woolsey

June 11, 2018
Blacksburg, Virginia

Keywords: autonomous vehicles, dynamics, parameter estimation, H_∞ control,
time-inhomogeneous Markov jump linear systems

Improved Dynamic Modeling and Robust Control of Autonomous Underwater Vehicles

Scott B. Gibson

ABSTRACT

In this dissertation, we seek to improve the dynamic modeling and control of autonomous underwater vehicles (AUVs). We address nonlinear hydrodynamic modeling, simplifying modeling assumptions, and robust control for AUVs. In the literature, various hydrodynamic models exist with varying model complexity and with no universally accepted model. We compare various hydrodynamic models traditionally employed to predict the motion of AUVs by estimating model coefficients using least-squares and adaptive identifier techniques. Additionally, we derive several dynamic models for an AUV employing varying sets of simplifying assumptions. We experimentally assess the efficacy of invoking typical assumptions to simplify the equations of motion.

For robust control design, we develop a procedure for designing robust attitude controllers based on loop-shaping ideas. We specifically address the challenge of adjusting the desired actuator bandwidth in a loop-shaping design framework. Finally, we present a novel receding horizon H_∞ control algorithm to improve the control of autonomous vehicle systems working in high-disturbance environments, employing a Markov jump linear system framework to model the stochastic and non-stationary disturbances experienced by the vehicle. Our main results include a new Bounded Real Lemma for stability analysis and an output feedback H_∞ control synthesis algorithm.

This work uses numerical simulations and extensive field trials of autonomous underwater vehicles to identify and verify dynamic models and to validate control algorithms developed herein.

Improved Dynamic Modeling and Robust Control of Autonomous Underwater Vehicles

Scott B. Gibson

GENERAL AUDIENCE ABSTRACT

In this dissertation, we seek to improve the dynamic modeling and control of autonomous underwater vehicles (AUVs). We compare different models employed to predict the motion of AUVs, and we derive several dynamic models for an AUV employing varying sets of simplifying assumptions. We experimentally assess the efficacy of invoking typical assumptions to simplify the equations of motion.

For robust control design, we develop a procedure for designing robust controllers that do not produce excessive fin movements. Finally, we present a novel robust control algorithm to improve the control of autonomous vehicle systems working in high-disturbance environments.

This work uses numerical simulations and extensive field trials of autonomous underwater vehicles to identify and verify dynamic models and to validate control algorithms developed herein.

To Kate, Chuck, and Theo

Acknowledgments

I express my sincere appreciation to my advisor, Dr. Stilwell, for his time and guidance throughout my studies. His constant encouragement motivated me to become a better writer, presenter, and researcher. I am especially grateful for his belief in a healthy work/life balance and his reminders of what matters most in life. I would like to thank my committee for their teaching excellence which significantly impacted my education. Their advice and suggestions for my research improved the quality of my work.

I would like to thank all members of the Autonomous Systems and Control Laboratory. I am grateful for their knowledge and help. I am thankful for all the unforgettable times during field trials and for my friends truly making work enjoyable. A special thanks to Michael Kepler, Brian McCarter, and Collin Lutz for their research collaboration on various portions of the work presented herein.

I am grateful for the love and support from my parents Brian and Alice whose encouragement made this work possible. I would also like to thank my siblings, especially Chris, for their support and for giving me an excuse to take vacations. I would like to express my deep love and appreciation for my children. They taught me the importance of time management and helped me maintain a great work/life balance. Finally, I would like to express my deepest gratitude to my wife Kate for her love and support. Her constant encouragement inspired me throughout my graduate studies. Thank you, with all my heart.

DISTRIBUTION STATEMENT A. Approved for public release; distribution is unlimited. AMRDEC control number PR 3743. Approved for public release.

Contents

List of Figures

List of Tables

Chapter 1

Introduction

In this dissertation, we seek to improve the dynamic modeling and control of autonomous underwater vehicles (AUVs). We address nonlinear hydrodynamic modeling, simplifying modeling assumptions, and robust control for AUVs. This work uses numerical simulations and extensive field trials of autonomous underwater vehicles to identify and verify dynamic models and to validate control algorithms developed herein.

1.1 Contributions

The main contributions of this dissertation are

1) the comparison of various hydrodynamic models traditionally employed to predict the motion of AUVs, where the estimation of model coefficients is performed using least-squares and adaptive identifier techniques;

2) the analysis of conventional simplifying model assumptions used for torpedo-shaped AUVs specifically applied to an AUV with an unconventional shape;

3) the development of a robust H_∞ loop-shaping design procedure for attitude control of AUVs to address the issue of control bandwidth, including the trade-off between performance tracking and actuator control effort; and

4) the derivation of a novel receding horizon H_∞ control algorithm with formal robustness guarantees for an autonomous vehicle modeled as a hidden Markov jump linear system

where the scheduling parameter or Markov chain is not directly observed.

We present field trial data and/or simulation results in all cases.

1.2 Research Platforms

Various AUVs have been developed by members of the Autonomous Systems and Controls Laboratory at Virginia Tech. The vehicles are used as research platforms to perform experiments and acquire field data. Experimental data sets presented in this dissertation were acquired using the vehicle systems shown in Figure 1.1.

(a) Virginia Tech 690 AUV (b) Virginia Tech 690S AUV (c) Virginia Tech TRSMAUV

Figure 1.1: Vehicles used as research platforms.

The Virginia Tech 690 AUV, in Figure 1.1a, is named after its hull diameter of 6.90 inches [46]. The 690 AUV is a general purpose AUV equipped with side-scan sonars for bathymetric surveys. The Virginia Tech 690S AUV, in Figure 1.1b, is a shorter variant of the 690 AUV with the same hull diameter. The Trawl-Resistant Self-Mooring AUV (TRSMAUV), in Figure 1.1c, is designed to deliver a trawl-resistant bottom mount to the sea floor [68]. The vehicle consists of a top half that contains vehicle propulsion and control surfaces and a bottom half which is the trawl-resistant bottom mount that sits on the sea floor. All vehicles have a depth rating of 500 meters.

This work seeks to improve the dynamic modeling and control of these vehicles to enable successful completion of mission objectives. As such, we seek to better understand the

dynamic models and simplifying assumptions used to describe the motion of these vehicles. With improved knowledge of the vehicle's dynamic models, we develop advanced model-based control algorithms and procedures to achieve mission requirements.

1.3 Motivation

1.3.1 Hydrodynamic Parameter Estimation

In the literature, various hydrodynamic models exist with no universally accepted model. Software tools for computational fluid dynamics (CFD) can be used to compute many terms including added mass and hydrodynamic coefficients, but computational cost is prohibitively large for practical applications. We use experimental data obtained from a streamlined AUV to estimate the hydrodynamic coefficients for various dynamic models found in the literature.

Hydrodynamic damping models for streamlined autonomous underwater vehicles characterize the forces and moments on an AUV due to hydrodynamic damping, which includes potential damping, skin friction, vortex shedding, and lift forces [23]. We compare the damping models by accuracy of the predicted motion of an AUV and by model complexity.

Additionally, we investigate the efficacy of estimating forces and moments due to control surfaces with the same data from which damping parameters are estimated. We then directly compare the results of estimated control surface forces and moments with those obtained using high-fidelity software tools. We use an offline least-squares method and an adaptive identifier method to approximate model coefficients from data obtained from field trials. Data acquired from field trials using the 690 AUV and the 690S AUV are presented.

1.3.2 Analysis of Conventional Simplifying Assumptions

The equations of motion for an AUV can be written compactly by invoking several simplifying assumptions, such as top-bottom symmetry. For a typical streamlined tail-controlled autonomous underwater vehicle, the simplifying assumptions are well-motivated. Simplifying assumptions that are often invoked for underwater vehicles include modeling the added mass as a prolate spheroid [4, 23, 26, 34]; omitting the off-diagonal elements of the inertia matrix [4, 54, 57]; neglecting the hydrodynamic coupling between the vehicle's roll, pitch, and yaw [22, 57]; and presuming the vehicle possesses three planes of symmetry to further simplify the equations of motion even if the vehicle is not symmetric about all three axes. For vehicles that possess an unconventional shape, the same simplifying assumptions may not be appropriate.

Some simplifying assumptions are questionable when applied to the TRSMAUV, shown in Figure 1.1c, due to the large appendages and the sharp edges on the exterior shape. Moreover, the TRSMAUV possesses port-starboard symmetry, but not the top-bottom symmetry that is often assumed for conventional AUVs. We derive several dynamic models for the TRSMAUV employing varying sets of simplifying assumptions to determine if the conventional assumptions are appropriate for the TRSMAUV. We experimentally assess the efficacy of invoking typical assumptions to simplify the equations of motion. Using data acquired during field trials, we show that the simplified equations of motion adequately represent the motion of the TRSMAUV.

1.3.3 Robust H_∞ Loop-Shaping Attitude Control Design

Previously designed attitude controllers for our AUVs emphasize minimizing the effect of coupled motion [53] and cause excessive fin movement. Sometimes mission objectives may require less energy consumption (e.g. actuator motion) and allow the tracking performance

requirements to be relaxed. To easily cater to these mission objectives, we develop a procedure for designing robust attitude controllers based on loop-shaping ideas for a streamlined tail-controlled AUV. We specifically address the challenge of adjusting the desired actuator bandwidth in a loop-shaping design framework.

We adopt the loop-shaping design ideas introduced by McFarlane and Glover [49]. We present two control topologies and procedures for designing robust attitude controllers for streamlined AUVs. We describe how to achieve a desired controller bandwidth during the design process using open-loop shaping guidelines. Our results are verified by evaluating performance in the field of several attitude controllers that are designed for the 690S AUV. The experimental results also show the trade-off between reference tracking performance and control effort.

1.3.4 Receding Horizon H_∞ Control

We consider the scenario of autonomous vehicle systems operating in a high-disturbance environment where the disturbances are non-stationary. For example, suppose there is an AUV conducting a robotic inspection of a bridge. In a tidal or river current, a bridge pier sheds vortices that disturb the water downstream of the pier [2, 30, 50]. The AUV conducting surveys of the piers will experience additional forces and moments due to the water disturbances in the wake of the pier. Also consider the indoor flight of an aerial vehicle. As the aerial vehicle nears the ground or flies through a doorway, prop-wash effects can destabilize the aerial vehicle. Self-generated disturbances and ground effects for confined indoor flight are discussed in [60, 61]. A control algorithm designed with probabilistic knowledge of future disturbances could provide better tracking performance in both scenarios.

We present a novel receding horizon H_∞ control algorithm to improve the control of autonomous vehicle systems working in high-disturbance environments. We employ a Markov

jump linear system framework to model the stochastic and non-stationary disturbances experienced by the vehicle. We address stability analysis and control synthesis for time-inhomogeneous Markov jump linear systems with partial observations of the Markov chain where the Markov parameter transition probabilities are non-stationary. We assume that the transition probabilities vary in a finite set and consider the case where a finite sequence of future transition probabilities is known. We use a detector-based approach to formally guarantee stability and expected l_2 performance where the Markov chain state or scheduling parameter is indirectly measured through a detector [12, 17]. Our main results include a new Bounded Real Lemma for stability analysis and an output feedback H_∞ control synthesis algorithm expressed as a finite set of linear matrix inequalities that can be efficiently solved. To conclude, a numerical simulation example is presented to validate our analysis.

1.4 Organization

This dissertation is organized as follows. In Chapter 2, the notation used throughout the dissertation is presented including naming conventions, coordinate systems, and equations of motion for an underwater vehicle. Additionally, standard results from matrix theory, systems theory, and Markov jump linear systems are presented for completeness. Different hydrodynamic parameter models are investigated in Chapter 3, and we present a least-squares and an adaptive identifier technique to estimate the model parameters. We experimentally evaluate the merits of various hydrodynamic damping and control surface models to accurately predict the motion of streamlined tail-controlled AUVs. In Chapter 4, conventional simplifying modeling assumptions for a conventional torpedo-shaped AUV are examined to determine the applicability of the assumptions for a less conventional vehicle. In Chapter 5, a process for designing a robust attitude controller based on loop-shaping ideas is presented for a streamlined tail-controlled AUV. The approach uses a loop-shaping procedure where

the open-loop frequency response of the system is shaped to achieve desired closed-loop performance and robustness goals. We specifically address the challenge of adjusting the desired control bandwidth in a loop-shaping design framework, and we discuss the trade-off between tracking performance and control effort. The receding horizon H_∞ controller is presented in Chapter 6. We provide stability results and an output feedback H_∞ control synthesis algorithm expressed as a finite set of linear matrix inequalities that can be efficiently solved. In Chapter 7, we give closing remarks and discuss potential extensions of the work presented herein.

Chapter 2

Preliminaries

2.1 Introduction

In this chapter, we present the equations of motion for an AUV used throughout the dissertation. Additionally, we establish notation and include standard results from matrix theory, systems theory, and discrete-time Markov jump linear systems used in the following chapters.

2.2 Equations of Motion

We formulate the rigid body AUV equations of motion as in [23, 27, 48]. Let $\eta_1 = [x\ y\ z]^\mathsf{T}$ represent the AUV's position in an earth-fixed inertial frame [23], and let $\eta_2 = [\phi\ \theta\ \psi]^\mathsf{T}$ be the attitude of the AUV represented using Euler angles where ϕ, θ, and ψ are roll, pitch, and yaw, respectively. The AUV body frame is defined in Figure 2.1. Let $\nu_1 = [u\ v\ w]^\mathsf{T}$ represent the AUV body frame linear velocity, and let $\nu_2 = [p\ q\ r]^\mathsf{T}$ be the body angular velocity where p, q, and r are roll rate, pitch rate, and yaw rate, respectively. We define $\eta = [\eta_1^\mathsf{T}\ \eta_2^\mathsf{T}]^\mathsf{T}$ and $\nu = [\nu_1^\mathsf{T}\ \nu_2^\mathsf{T}]^\mathsf{T}$ where η, $\nu \in \mathbb{R}^{6\times 1}$.

Sometimes it is convenient to express the vehicle's body frame linear velocities in terms of $[V, \beta, \alpha]^\mathsf{T}$ where V represents the speed of the vehicle, α is the angle of attack, and β is the side-slip angle (see Figure 2.1). The transformation is given by

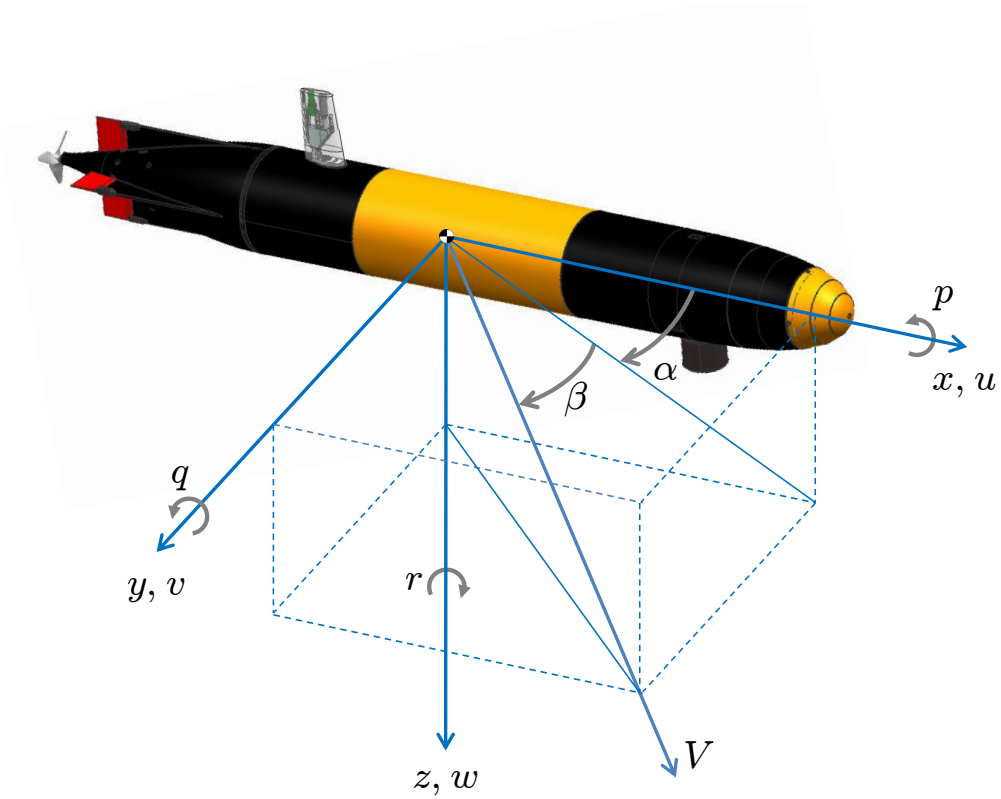

Figure 2.1: The AUV body frame is a body-fixed coordinate frame where the origin is located at the center of buoyancy, the x-axis points out the nose of the vehicle, the y-axis points out the starboard side of the vehicle, and the z-axis points out the bottom of the vehicle.

$$V = \sqrt{u^2 + v^2 + w^2}, \qquad u = V \cos\alpha \cos\beta, \tag{2.1a}$$

$$\beta = \arcsin \frac{v}{\sqrt{u^2 + v^2 + w^2}}, \qquad v = V \sin\beta, \tag{2.1b}$$

$$\alpha = \arctan \frac{w}{u}, \qquad w = V \sin\alpha \cos\beta. \tag{2.1c}$$

The kinematic model of the AUV is a rotation of body frame velocities to the inertial frame expressed

$$\dot{\eta} = \begin{bmatrix} R_1(\eta_2) & 0_{3\times3} \\ 0_{3\times3} & R_2(\eta_2) \end{bmatrix} \nu \tag{2.2}$$

where

$$R_1(\eta_2) = \begin{bmatrix} \cos\theta\cos\psi & \sin\phi\sin\theta\cos\psi - \cos\phi\sin\psi & \cos\phi\sin\theta\cos\psi + \sin\phi\sin\psi \\ \cos\theta\sin\psi & \sin\phi\sin\theta\sin\psi + \cos\phi\cos\psi & \cos\phi\sin\theta\sin\psi - \sin\phi\cos\psi \\ -\sin\theta & \sin\phi\cos\theta & \cos\phi\cos\theta \end{bmatrix} \tag{2.3}$$

$$R_2(\eta_2) = \begin{bmatrix} 1 & \sin\phi\tan\theta & \cos\phi\tan\theta \\ 0 & \cos\phi & -\sin\phi \\ 0 & \frac{\sin\phi}{\cos\theta} & \frac{\cos\phi}{\cos\theta} \end{bmatrix} \tag{2.4}$$

represent the rotation from the body frame to the inertial frame and the relationship between body frame rates and Euler angle rates, respectively.

We model the AUV with added mass, Coriolis, damping, gravitational, buoyancy and control forces. The dynamic model for the AUV in the body frame is

$$M\dot{\nu} = \mathcal{H}_C(M\nu)\nu + D(\nu) + \mathcal{G}(R_1(\eta_2)) + U_{CS}(\delta) + U_{Prop} \tag{2.5}$$

where

$$\mathcal{G}(R_1(\eta_2)) = \begin{bmatrix} (g+b)R_1^{\mathsf{T}}(\eta_2)e_3 \\ r_G \times (gR_1^{\mathsf{T}}(\eta_2)e_3) + r_B \times (bR_1^{\mathsf{T}}(\eta_2)e_3) \end{bmatrix}, \tag{2.6}$$

$$e_3 = \begin{bmatrix} 0 \\ 0 \\ 1 \end{bmatrix},$$

$g \in \mathbb{R}$ is the gravitational force on the vehicle, $b \in \mathbb{R}$ is the buoyancy force on the vehicle, $r_G = [x_G \ y_G \ z_G]^{\mathsf{T}} \in \mathbb{R}^{3\times1}$ is the vector from the origin to the vehicle's center of gravity, $r_B = [x_B \ y_B \ z_B]^{\mathsf{T}} \in \mathbb{R}^{3\times1}$ is the vector from the origin to the vehicle's center of buoyancy, $M \in \mathbb{R}^{6\times6}$ is the mass matrix consisting of the rigid-body inertia matrix plus the added

mass matrix $M = M_{RB} + M_A$, $D(\nu) \in \mathbb{R}^{6\times 1}$ represents the damping forces and moments, $\delta = [\delta_e \ \delta_r]^{\mathsf{T}} \in \mathbb{R}^{2\times 1}$ is the elevator and rudder angle, $U_{CS} \in \mathbb{R}^{6\times 1}$ represents the forces and moments due to the control surfaces, $U_{Prop} \in \mathbb{R}^{6\times 1}$ represents the forces and moments due to the propeller, and $\mathcal{H}_C(M\nu)\nu$ represents the Coriolis forces and moments. The functions $\mathcal{J} : \mathbb{R}^3 \to \mathbb{R}^{3\times 3}$ and $\mathcal{H}_C : \mathbb{R}^6 \to \mathbb{R}^{6\times 6}$ are

$$\mathcal{J}\left(\begin{bmatrix} \omega 1 \\ \omega 2 \\ \omega 3 \end{bmatrix}\right) = \begin{bmatrix} 0 & -\omega_3 & \omega_2 \\ \omega_3 & 0 & -\omega_1 \\ -\omega_2 & \omega_1 & 0 \end{bmatrix}$$
$$\mathcal{H}_C\left(\begin{bmatrix} \nu_1 \\ \nu_2 \end{bmatrix}\right) = \begin{bmatrix} 0_{3\times 3} & \mathcal{J}(\nu_1) \\ \mathcal{J}(\nu_1) & \mathcal{J}(\nu_2) \end{bmatrix}.$$

The rigid-body mass matrix M_{RB} is

$$M_{RB} = \begin{bmatrix} m & 0 & 0 & 0 & mz_G & -my_G \\ 0 & m & 0 & -mz_G & 0 & mx_G \\ 0 & 0 & m & my_G & -mx_G & 0 \\ 0 & -mz_G & my_G & J_x & -J_{xy} & -J_{xz} \\ mz_G & 0 & -mx_G & -J_{yx} & J_y & -J_{yz} \\ -my_G & mx_G & 0 & -J_{zx} & -J_{zy} & J_z \end{bmatrix} \tag{2.7}$$

where m is the mass of the vehicle and J represents the moments of inertia.

Property 2.1. (See [23, Property 2.2]) The parameterization of the rigid-body inertia matrix M_{RB} (2.7) is unique and it satisfies

$$M_{RB} = M_{RB}^{\mathsf{T}} > 0, \qquad \dot{M}_{RB} = 0.$$

2.3 Matrix Theory

Let the elements of $A \in \mathbb{R}^{n\times m}$ be denoted $A_{(i,j)}$ with $i \in [1,n]$ and $j \in [1,m]$. Let the j-th column of $A \in \mathbb{R}^{n\times m}$ be denoted $\mathrm{col}_j(A)$.

Definition 2.2. (See [6, Section 7.1]) For $A \in \mathbb{R}^{n\times m}$ define the vec operator as

$$\mathrm{vec}\ A \triangleq \begin{bmatrix} \mathrm{col}_1(A) \\ \vdots \\ \mathrm{col}_m(A) \end{bmatrix} \in \mathbb{R}^{nm\times 1} \tag{2.8}$$

which is the column vector of size $nm \times 1$ obtained by stacking the columns of A. The matrix A is recovered from vec A by writing

$$A = \mathrm{vec}^{-1}(\mathrm{vec}A). \tag{2.9}$$

Definition 2.3. (See [6, Section 7.1]) Let $A \in \mathbb{R}^{n\times m}$ and $B \in \mathbb{R}^{l\times k}$. Then the *Kronecker product* $A \otimes B \in \mathbb{R}^{nl\times mk}$ of A is the partitioned matrix

$$A \otimes B \triangleq \begin{bmatrix} A_{(1,1)}B & A_{(1,2)}B & \cdots & A_{(1,m)}B \\ \vdots & \vdots & \ddots & \vdots \\ A_{(n,1)}B & A_{(n,2)}B & \cdots & A_{(n,m)}B \end{bmatrix}. \tag{2.10}$$

Proposition 2.4. *(See [6, Proposition 7.1.9]) Let $A \in \mathbb{R}^{n\times m}$, $B \in \mathbb{R}^{m\times l}$, and $C \in \mathbb{R}^{l\times k}$. Then,*

$$\mathrm{vec}(ABC) = (C^{\mathsf{T}} \otimes A)\mathrm{vec}\ B. \tag{2.11}$$

2.3.1 Linear Matrix Inequalities

A linear matrix inequality (LMI) is an inequality of the form

$$F(y) = F_0 + \sum_{i=1}^{m} y_i F_i > 0 \tag{2.12}$$

where F_i are constant symmetric matrices for $i = 0, \ldots, m$, and $y \in \mathbb{R}^m$ is the variable. LMIs are an important theoretical tool and can be solved efficiently by readily available software solvers [3, 41].

Theorem 2.5. *[Schur Complement] (See [19, Theorem 1.10]) Suppose that A, B, and C are real matrices and that A and B are symmetric. Then the following are equivalent if the matrices are conformable:*

1. *The matrix inequalities $A > 0$ and $C - B^{\mathsf{T}} A^{-1} B > 0$ both hold.*
2. *The matrix inequalities $C > 0$ and $A - B C^{-1} B^{\mathsf{T}} > 0$ both hold.*
3. *The matrix inequality $\begin{bmatrix} A & B \\ B^{\mathsf{T}} & C \end{bmatrix} > 0$ is satisfied.*

Lemma 2.6. *[Projection Lemma] (See [24, Lemma 3.1]) Given a symmetric matrix $\mathcal{H} \in \mathbb{R}^{n \times n}$ and two matrices P and Q of column dimension n, consider the problem of finding some matrix K of compatible dimensions such that*

$$\mathcal{H} + Q^{\mathsf{T}} K^{\mathsf{T}} P + P^{\mathsf{T}} K Q < 0. \tag{2.13}$$

Denote by W_P and W_Q any matrices whose columns form bases of the null spaces of P and

Q, respectively. Then (2.13) is solvable for K if and only if the following two conditions hold

$$W_P^{\mathsf{T}}\mathcal{H}W_P < 0$$
$$W_Q^{\mathsf{T}}\mathcal{H}W_Q < 0.$$

2.4 Systems Theory

Lemma 2.7. *(See [35, Lemma 3.2.3]) A function $f(t)$ that is bounded from below and is nonincreasing has a limit as $t \to \infty$.*

Definition 2.8. (See [37]) A function $f(x,t)$ is locally Lipschitz in x on $D \times [a,b] \subset \mathbb{R}^n \times \mathbb{R}$ if each point $x \in D$ has a neighborhood D_0 such that f satisfies

$$\|f(x_1,t) - f(x_2,t)\| \leq L\|x_1 - x_2\| \tag{2.14}$$

for all $x_1, x_2 \in D_0$ and $t \in [a,b]$ with some Lipschitz constant L.

Theorem 2.9. *[Lyapunov's Stability Theorem for Time-Varying Systems] (See [37, Theorem 4.8]) Consider the system*

$$\dot{x} = f(x,t) \tag{2.15}$$

where $f : D \times [0,\infty) \to \mathbb{R}^n$ is piecewise continuous in t and locally Lipschitz in x on $D \times [0,\infty)$, and $D \subset \mathbb{R}^n$ is a domain that contains the origin $x = 0$. Let $x = 0$ be an equilibrium point. Let $V : D \times [0,\infty) \to \mathbb{R}$ be a continuously differentiable function such that

$$W_1(x) \leq V(x,t) \leq W_2(x)$$
$$\frac{dV}{dt} = \frac{\partial V}{\partial t} + \frac{\partial V}{\partial x} f(x,t) \leq 0$$

for all $t \geq 0$ and $x \in D$ where $W_1(x)$ and $W_2(x)$ are continuous positive-definite functions

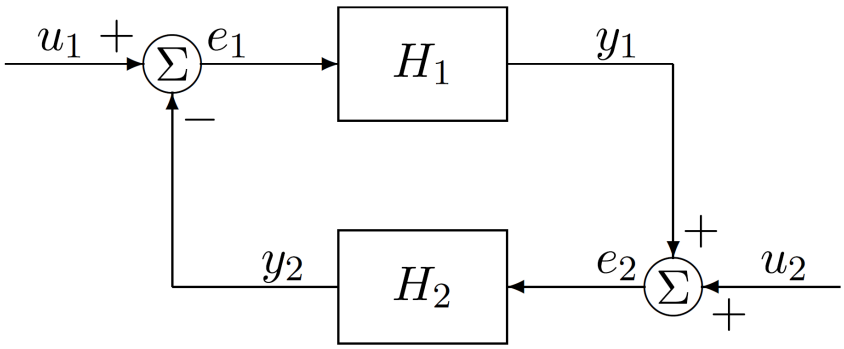

Figure 2.2: Feedback Connection

on D. Then, the origin is uniformly stable.

Definition 2.10. The function $f(t) : \mathbb{R} \to \mathbb{R}^n$ is in $\mathcal{L}_\infty$ or $f \in \mathcal{L}_\infty$ if

$$\|f\|_{\mathcal{L}_\infty} = \sup_{t \geq 0} \|f(t)\| < \infty.$$

The function $f(t) : \mathbb{R} \to \mathbb{R}^n$ is square-integrable or $f \in \mathcal{L}_2$ if

$$\|f\|_{\mathcal{L}_2} = \sqrt{\int_0^\infty f^\mathsf{T}(t) f(t) dt} < \infty.$$

The function $f(t) : \mathbb{R} \to \mathbb{R}^n$ is in $\mathcal{L}_p$ or $f \in \mathcal{L}_p$ if

$$\|f\|_{\mathcal{L}_p} = \left(\int_0^\infty \|f(t)\|^p dt \right)^{1/p} < \infty.$$

Lemma 2.11. *(See [35, Lemma 3.2.5]) If f, $\dot{f} \in \mathcal{L}_\infty$ and $f \in \mathcal{L}_p$ for some $p \in [1, \infty)$, then $f(t) \to 0$ as $t \to \infty$. Note: This lemma is a special case of Barbalat's Lemma.*

The small-gain theorem [35, 37] is a way to study the robustness of a system. It enables the analysis of input-output stability of feedback connections in a system and formally guarantees robustness to model uncertainties or exogenous disturbances.

Definition 2.12. The operator $H : \mathcal{L} \to \mathcal{L}$ is finite-gain $\mathcal{L}$ stable if there exists a nonnegative constant γ such that

$$\|y\|_{\mathcal{L}} \leq \gamma \|u\|_{\mathcal{L}}$$

for all $u \in \mathcal{L}$ where $y = Hu$.

Theorem 2.13. *[Small Gain Theorem] (See [37, Theorem 5.6]) Consider the feedback connection in Figure 2.2, where $H_1 : \mathcal{L} \to \mathcal{L}$ is a stable nominal system, γ_1 is the finite-gain of H_1, $H_2 : \mathcal{L} \to \mathcal{L}$ is a stable perturbation, and γ_2 is the finite-gain of H_2. Then the feedback connection in Figure 2.2 is finite-gain stable if $\gamma_1\gamma_2 < 1$.*

Therefore, the feedback connection is stable if the finite-gain of the stable perturbation H_2 satisfies $\gamma_2 < 1/\gamma_1$ where $\|y_2\| \leq \gamma_2 \|e_2\|$.

2.5 Discrete-Time Markov Jump Linear Systems

A Markov jump linear system is a discrete-time linear state equation whose coefficient matrices are indexed by a Markov chain,

$$\mathbb{G} : \left\{ \begin{bmatrix} x(k+1) \\ z(k) \end{bmatrix} = \begin{bmatrix} A(\vartheta(k)) & B(\vartheta(k)) \\ C(\vartheta(k)) & D(\vartheta(k)) \end{bmatrix} \begin{bmatrix} x(k) \\ w(k) \end{bmatrix} \right. \tag{2.16}$$

where k is the discrete-time index, $x(k) \in \mathbb{R}^n$ is the state vector, $w(k) \in \mathbb{R}^{m_1}$ is the disturbance input, $z(k) \in \mathbb{R}^{p_1}$ is the error output, $\vartheta(k) \in \mathcal{N}$ is the scheduling parameter that varies with time in a finite set $\mathcal{N} = \{1, \ldots, N\}$, and $\mathbb{G} = \{(A(i), B(i), C(i), D(i)) : i \in \mathcal{N}\}$ is the set of a finite number of system matrices. For notational convenience, let $\vartheta(k) = \vartheta_k$ and $\vartheta(k+1) = \vartheta_{k+1}$.

The sequence of parameters ϑ_k are a Markov chain where the transition probabilities are denoted by $p_{ij}(k) = \mathbf{P}\{\vartheta_{k+1} = j | \vartheta_k = i\}$ and satisfy $\sum_{j=1}^{N} p_{ij}(k) = 1$ for all k. For the case

of time-inhomogeneous Markov chains, the transition probabilities are non-stationary and are denoted by $p_{ij}(k)$.

Definition 2.14. The *transition probability matrix* for a time-inhomogeneous Markov chain is

$$\Pi(k) = \begin{bmatrix} p_{11}(k) & p_{12}(k) & \cdots & p_{1N}(k) \\ p_{21}(k) & p_{22}(k) & \cdots & p_{2N}(k) \\ \vdots & \vdots & \ddots & \vdots \\ p_{N1}(k) & p_{N2}(k) & \cdots & p_{NN}(k) \end{bmatrix} \in \mathbb{R}^{N\times N} \tag{2.17}$$

where the notation $p_{ij}(k) = \mathbf{P}\{\vartheta_{k+1} = j | \vartheta_k = i\}$ denotes the ij-th element of the matrix $\Pi(k)$.

We define the usual space of square summable stochastic sequences

$$\ell_2 = \{\{x(k)\}_{k=0}^{\infty} : \|x\|_{\ell_2} < \infty\}$$

where

$$\|x\|_{\ell_2}^2 = \sum_{k=0}^{\infty} \mathbf{E}[x^{\mathsf{T}}(k)x(k)].$$

Definition 2.15. Uniformly exponentially mean square stable (UEMSS): The Markov jump linear system (2.16) is *uniformly exponentially mean square stable* if there exist $c \geq 1$ and $0 < \lambda < 1$ such that for every initial state (x_0, ϑ_0) and all $k \geq 0$

$$\mathbf{E}\left[\|x(k; x_0, \vartheta_0)\|_{\ell_2}^2 | x_0, \vartheta_0\right] \leq c\lambda^k \|x_0\|_{\ell_2}^2 \tag{2.18}$$

Definition 2.16. (See [59, Definition 2]) Assume that system (2.16) is UEMSS. Let $x(0) = 0$.

The H_∞ norm of system (2.16) is defined to be

$$\|\mathbb{G}\|_\infty = \sup_{\vartheta(0)\in\mathcal{N}} \sup_{0\neq w\in\ell_2} \frac{\|z\|_{\ell_2}}{\|w\|_{\ell_2}}. \tag{2.19}$$

Definition 2.17. (See [59, Definition 3]) The system (2.16) is weakly controllable if for every initial state/mode, (x_0, ϑ_0), and any final state/mode, (x_f, ϑ_f), there exists a finite time T_c and an input $w_c(k)$ such that $\mathbf{P}\{x(T_c) = x_f \text{ and } \vartheta(T_c) = \theta_f\} > 0$.

2.5.1 Stability and Disturbance Attenuation Results

Infinite-dimensional results

Let $\mathbb{S}_n^+$ be the set of symmetric positive-definite matrices, and let $\mathbb{N}$ and $\mathbb{N}_0$ be the set of all positive and nonnegative integers, respectively.

Lemma 2.18. *(See [1, 43]) Assume that the system $\mathbb{G}$ is weakly controllable and $\mathbf{P}\{\vartheta_k = i\} > 0$ for all $i \in \mathcal{N}$ and $k \in \mathbb{N}_0$. The time-inhomogeneous Markov jump linear system (2.16) is UEMSS and $\|\mathbb{G}\|_\infty < \gamma$ if an only if there exist $\eta, \rho, \nu > 0$ and a function $X : \mathcal{N} \times \mathbb{N}_0 \to \mathbb{S}_n^+$ such that*

$$\eta I \leq X(i,k) \leq \rho I \tag{2.20}$$

$$\begin{bmatrix} A(i) & B(i) \\ C(i) & D(i) \end{bmatrix}^{\mathsf{T}} \begin{bmatrix} \tilde{X}(i,k+1) & 0 \\ 0 & I \end{bmatrix} \begin{bmatrix} A(i) & B(i) \\ C(i) & D(i) \end{bmatrix} - \begin{bmatrix} X(i,k) & 0 \\ 0 & \gamma^2 I \end{bmatrix} < -\nu I \tag{2.21}$$

for all $i \in \mathcal{N}$ and all $k \in \mathbb{N}_0$ where $\tilde{X}(i,k+1) = \sum_{j=1}^{N} p_{ij}(k+1)X(j,k+1)$.

Remark 2.19. Note that solving for the matrix variable X in Lemma 2.18 possibly requires solving an infinite number of LMIs due to the time-varying probability $p_{ij}(k+1)$.

Finite-dimensional results

Let $\varphi \in \Psi$ be a possible switching sequence where $\varphi(k) \in \{1, 2, \ldots, J\}$ and Ψ is the set of possible switching sequences. Consider the case where the sequence of transition probability matrices varies in a finite set $\{\Pi(\varphi(k)) \mid \varphi(k) \in \{1, 2, \ldots, J\}\}$. The notation $\pi_{ij}(\varphi(k))$ denotes the ij-th element of the matrix $\Pi(\varphi(k))$ and is equal to the probability $\mathbf{P}\{\vartheta_{k+1} = j | \vartheta_k = i\}$. We define $r_M(k) := [\varphi(k+1), \varphi(k+2), \ldots, \varphi(k+M)]$ to be the next M values of the switching sequence at time k and Ψ_M to be the set of all sequences of length M. By convention, if $M = 0$ then the empty sequence is given by $r_0(k) = \emptyset$ and the singleton set is given by $\Psi_0 = \{\emptyset\}$.

Stability and disturbance attenuation of time-inhomogeneous Markov jump linear systems where the transition probability matrices vary in a finite set is established in [44] using a finite-future dependent Lyapunov function. The following results rely on solving a finite number of LMIs.

Theorem 2.20. *(See [44, Theorem 4]) System (2.16) is UEMSS if and only if there exist an $M \in \mathbb{N}_0$ and a function $X : \mathcal{N} \times \Psi_M \to \mathbb{S}_n^+$ such that*

$$A^{\mathsf{T}}(i) \sum_{j=1}^{N} \pi_{ij}(r_1(k)) X(j, r_M(k+1)) A(i) - X(i, r_M(k)) < 0 \tag{2.22}$$

for any $r_M(k), r_M(k+1) \in \Psi_M$ and $i \in \mathcal{N}$.

Theorem 2.21. *(See [44, Theorem 22]) Assume $\mathbf{P}\{\vartheta_k = i\} > 0$ for all $\varphi \in \Psi$, $i \in \mathcal{N}$, and $k \in \mathbb{N}_0$. System (2.16) is UEMSS with $\|\mathbb{G}\|_\infty < \gamma$ if and only if there exist an $M \in \mathbb{N}_0$ and*

a function $X : \mathcal{N} \times \Psi_M \to \mathbb{S}_n^+$ *such that*

$$\begin{bmatrix} A(i) & B(i) \\ C(i) & D(i) \end{bmatrix}^{\mathsf{T}} \begin{bmatrix} \sum_{j=1}^{N} \pi_{ij}(r_1(k)) X(j, r_M(k+1)) & 0 \\ 0 & I \end{bmatrix} \begin{bmatrix} A(i) & B(i) \\ C(i) & D(i) \end{bmatrix} - \begin{bmatrix} X(i, r_M(k)) & 0 \\ 0 & \gamma^2 I \end{bmatrix} < 0 \tag{2.23}$$

for any $r_M(k), r_M(k+1) \in \Psi_M$ *and* $i \in \mathcal{N}$.

Chapter 3

Hydrodynamic Parameter Estimation

3.1 Introduction

The goal of this chapter is to experimentally evaluate the merits of various hydrodynamic damping models for streamlined tail-controlled autonomous underwater vehicles (AUVs). We seek damping models that can be used to accurately predict the motion of a streamlined AUV, but do not possess unnecessary complexity. Moreover, we seek methods for estimating the dynamical model of a streamlined AUV, including damping parameters.

Lumped-parameter models are often derived from experimental performance data [52, 56]. They are characterized by each axis of motion (e.g., pitch or yaw axis) being modeled by a second-order system that is decoupled from other axes of motion [10, 23, 56]. Lumped-parameter models are often sufficient for control design, but more complete dynamical models may be needed for other purposes, including the design of control systems that are aware of coupling between axes of motion [53].

Hydrodynamic damping models for streamlined autonomous underwater vehicles characterize the forces and moments on an AUV due to hydrodynamic damping. In the literature, various hydrodynamic damping models exist with no universally accepted model. We seek to use experimental data from a streamlined AUV to identify model coefficients. Software tools for computational fluid dynamics (CFD) can be used to compute many terms including added mass and added inertia, but computational requirements are prohibitively large.

Since we seek to obtain a dynamic model from experimental data, we assume that added

mass and inertia can be modeled by that of a prolate spheroid whose shape and volume are related to that of the AUV [4, 23, 31, 34]. Other terms, including those due to gravity and buoyancy, are estimated or computed from direct measurement of the physical characteristics of the AUV. Damping parameters are estimated from data obtained during free-swimming experiments. The effect of control surfaces in the tail can be estimated from analysis in high-fidelity software tools [8] or from lift and drag of similar airfoil shapes [4]. Because we seek to estimate a complete model from data acquired during free-swimming experiments, we also investigate the efficacy of estimating forces due to control surfaces with the same data from which damping parameters are estimated. That is, we propose a model for control surface forces and estimate the parameters of the model while also estimating hydrodynamic parameters. We then directly compare the results of estimated control surface forces with that obtained using a high-fidelity software tool. Specifically, we use the Virginia Tech 690 high-fidelity control surface model created using the DRDC Submarine Simulation Program (DSSP) [45] from [8, Appendix A.2.2]. We propose a linear-quadratic control surface (LQCS) model to represent the asymmetric and nonlinear forces generated by the DSSP tool.

Hydrodynamic damping includes potential damping, skin friction, vortex shedding, and lift forces [23]. As in [27, 47], we compare the following hydrodynamic damping models: McFarland-Whitcomb, pitch-yaw, Gertler-Hagen, linear, Coe, Prestero, uncoupled, and Fossen. To the best of our knowledge, the proposed eight hydrodynamic damping models provide a thorough representation of hydrodynamic damping models in the literature. As shown in [47], each model varies in complexity and derivation. The McFarland-Whitcomb hydrodynamic model is fully coupled and assumes a sign-preserved quadratic relationship between velocity and force. The pitch-yaw model is constructed by superimposing separate models for pitch and yaw. The Gertler-Hagen model, as proposed in [26], comes from a U.S. Navy techinical report intending to standardize the equations of motion for a submarine. The linear model assumes a linear relationship between velocity and force. The Coe model,

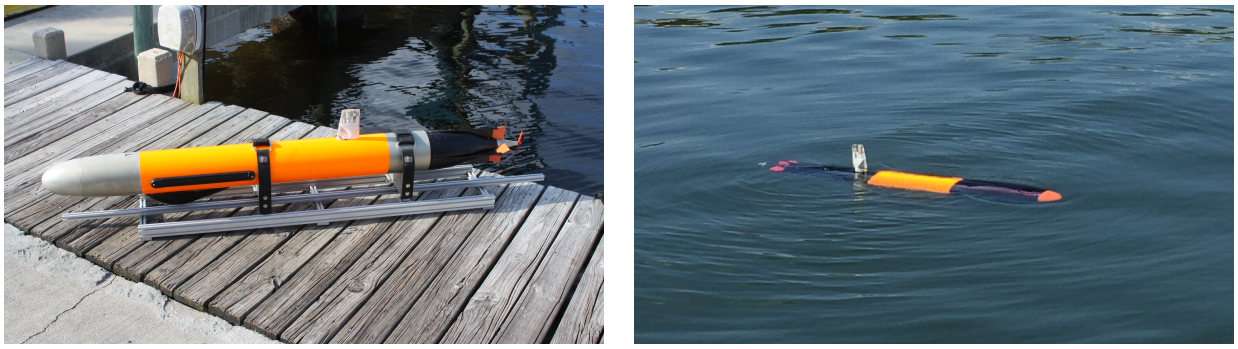

(a) Virginia Tech 690 AUV (b) Virginia Tech 690S AUV

Figure 3.1: Vehicles used for parameter estimation and data collection

presented in [8], is based on a Taylor series expansion and assumes port/starboard vehicle symmetry. The Prestero model, shown in [56], includes axial drag, crossflow drag, and body lift. The uncoupled model assumes that motion in each axis is only dependent on velocity in that dimension. The Fossen model, as proposed in [23], is uncoupled, but retains both linear and quadratic terms. In this chapter, we include a way to represent different models with the same equations of motion.

We use a least-squares method and an adaptive identifier method to approximate damping model coefficients and the control surface parameters. Angular acceleration measurements are required for the least-squares method. If angular acceleration is not directly measured, then it must be inferred from other measurements. As shown in [27, 48], the adaptive identifier method is another way to compute the coefficients of each model. The adaptive identifier does not require the vehicle's angular acceleration. We specialize the general identifier proposed in [48] for our application and show that the estimation error dynamics of the identifier are locally asymptotically stable.

Experimental data sets were acquired by the Virginia Tech 690 AUV [46] shown in Figure 3.1a and the Virginia Tech 690S AUV shown in Figure 3.1b. Both vehicles are streamlined tail-controlled AUVs with a single propeller at the stern. Our results show that the linear model has comparable performance to more complex models but employs fewer parameters.

We also compare a high-fidelity control surface model with estimating the parameters of a linear-quadratic control surface model. Our results confirm that both identification methods produce similar results.

3.2 Problem Statement

3.2.1 Equations of Motion

We model the kinematic (2.2) and dynamic (2.5) equations of motion for an AUV as in Chapter 2.

Assumption 3.1. The model has the following characteristics:

(a) The AUV body velocities ν are bounded.

(b) The gravitational force g and buoyancy force b are known and constant.

3.2.2 Damping Model Structure

In order to compare damping models, we implement the following damping model structure. Let

$$D(\nu) = \begin{bmatrix} D^{\mathrm{X}}(\nu) \\ D^{\mathrm{Y}}(\nu) \\ D^{\mathrm{Z}}(\nu) \\ D^{\mathrm{K}}(\nu) \\ D^{\mathrm{M}}(\nu) \\ D^{\mathrm{N}}(\nu) \end{bmatrix} \tag{3.1}$$

model damping forces and moments on the AUV. We express each scalar function in (3.1) as a linear combination of basis functions, which represent all possible combinations of linear

and angular velocity for which force and moment due to hydrodynamic damping might be dependent. For example, the heave force $D^{\mathrm{Z}}(\nu)$ might be modeled as a function of heave velocity w and sway velocity v, $D^{\mathrm{Z}}(\nu) = \mathrm{Z_v} v + \mathrm{Z_w} w$, which can be expressed

$$D^{\mathrm{Z}}(\nu) = K_D^{\mathrm{Z}} \xi_D^{\mathrm{Z}}(\nu)$$

with coefficients $K_D^{\mathrm{Z}} = [0 \ \mathrm{Z_v} \ \mathrm{Z_w}]$ and velocity basis functions $\xi_D^{\mathrm{Z}}(\nu) = [u \ v \ w]^{\mathsf{T}}$. A generic damping model can be expressed as

$$D(\nu) = \begin{bmatrix} D^{\mathrm{X}}(\nu) \\ D^{\mathrm{Y}}(\nu) \\ D^{\mathrm{Z}}(\nu) \\ D^{\mathrm{K}}(\nu) \\ D^{\mathrm{M}}(\nu) \\ D^{\mathrm{N}}(\nu) \end{bmatrix} = \begin{bmatrix} K_D^{\mathrm{X}} \xi_D(\nu) \\ K_D^{\mathrm{Y}} \xi_D(\nu) \\ K_D^{\mathrm{Z}} \xi_D(\nu) \\ K_D^{\mathrm{K}} \xi_D(\nu) \\ K_D^{\mathrm{M}} \xi_D(\nu) \\ K_D^{\mathrm{N}} \xi_D(\nu) \end{bmatrix} = \begin{bmatrix} K_D^{\mathrm{X}} \\ K_D^{\mathrm{Y}} \\ K_D^{\mathrm{Z}} \\ K_D^{\mathrm{K}} \\ K_D^{\mathrm{M}} \\ K_D^{\mathrm{N}} \end{bmatrix} \xi_D(\nu) = K_D \xi_D(\nu),$$

where $\xi_D(\nu) \in \mathbb{R}^{n_{\xi_D} \times 1}$ is a vector that includes all n_{ξ_D} basis functions from all the damping models and $K_D \in \mathbb{R}^{6 \times n_{\xi_D}}$ is the damping coefficient matrix. Each damping model has a unique constant K_D that selects the appropriate basis functions from $\xi_D(\nu)$.

Assumption 3.2. The vector of basis functions, $\xi_D(\nu)$, is bounded if ν is bounded.

3.2.3 Damping Models

Viscous hydrodynamic damping models describe the dissipative forces caused by potential damping, drag, lift, body oscillations, and vortex shedding [23]. As in [27], we compare the following hydrodynamic damping models: McFarland-Whitcomb, pitch-yaw, Gertler-Hagen, linear, Coe, Prestero, uncoupled, and Fossen.

Linear

The linear damping model assumes a linear relationship between velocity and damping forces and moments. The damping force D^{X} along the surge axis is expressed

$$D^{\mathrm{X}}(\nu) = \mathrm{X_u}u + \mathrm{X_v}v + \mathrm{X_w}w + \mathrm{X_p}p + \mathrm{X_q}q + \mathrm{X_r}r,$$

where damping forces and moments D^{Y}, D^{Z}, D^{K}, D^{M}, and D^{N} are defined by replacing X with Y, Z, K, M, and N.

McFarland-Whitcomb

The McFarland-Whitcomb damping model [48] is fully coupled and assumes a sign-preserved quadratic relationship between velocity and force. The damping force D^{X} along the surge axis is expressed

$$\begin{aligned}
D^{\mathrm{X}}(\nu) = {} & \mathrm{X}_{u|u|}u|u| + \mathrm{X}_{u|v|}u|v| + \mathrm{X}_{u|w|}u|w| + \mathrm{X}_{u|p|}u|p| + \mathrm{X}_{u|q|}u|q| + \mathrm{X}_{u|r|}u|r| \\
& + \mathrm{X}_{v|u|}v|u| + \mathrm{X}_{v|v|}v|v| + \mathrm{X}_{v|w|}v|w| + \mathrm{X}_{v|p|}v|p| + \mathrm{X}_{v|q|}v|q| + \mathrm{X}_{v|r|}v|r| \\
& + \mathrm{X}_{w|u|}w|u| + \mathrm{X}_{w|v|}w|v| + \mathrm{X}_{w|w|}w|w| + \mathrm{X}_{w|p|}w|p| + \mathrm{X}_{w|q|}w|q| + \mathrm{X}_{w|r|}w|r| \\
& + \mathrm{X}_{p|u|}p|u| + \mathrm{X}_{p|v|}p|v| + \mathrm{X}_{p|w|}p|w| + \mathrm{X}_{p|p|}p|p| + \mathrm{X}_{p|q|}p|q| + \mathrm{X}_{p|r|}p|r| \\
& + \mathrm{X}_{q|u|}q|u| + \mathrm{X}_{q|v|}q|v| + \mathrm{X}_{q|w|}q|w| + \mathrm{X}_{q|p|}q|p| + \mathrm{X}_{q|q|}q|q| + \mathrm{X}_{q|r|}q|r| \\
& + \mathrm{X}_{r|u|}r|u| + \mathrm{X}_{r|v|}r|v| + \mathrm{X}_{r|w|}r|w| + \mathrm{X}_{r|p|}r|p| + \mathrm{X}_{r|q|}r|q| + \mathrm{X}_{r|r|}r|r|,
\end{aligned}$$

where damping forces and moments D^{Y}, D^{Z}, D^{K}, D^{M}, and D^{N} are defined by replacing X with Y, Z, K, M, and N.

Pitch-yaw

The pitch-yaw damping model is constructed by superimposing separate models for pitch and yaw. Note that the model assumes no x-axis damping moment will occur due to x-axis angular velocity p, which means that all the entries in D^{K} are zero. The damping force D^{X} along the surge axis and the damping force D^{Y} along the sway axis are expressed

$$\begin{aligned}
D^{\mathrm{X}}(\nu) = {} & \mathrm{X_q}q + \mathrm{X_r}r + \mathrm{X_u}u + \mathrm{X_v}v + \mathrm{X_w}w + \mathrm{X_{qq}}q^2 + \mathrm{X_{|r|}}|r| + \mathrm{X_{uu}}u^2 + \mathrm{X_{u|r|}}u|r| \\
& + \mathrm{X_{ww}}w^2 + \mathrm{X_{|v|}}|v| + \mathrm{X_{vv}}v^2 + \mathrm{X_{q|w|}}q|w| + \mathrm{X_{r|v|}}r|v| + \mathrm{X_{v|r|}}v|r| + \mathrm{X_{vr}}vr \\
& + \mathrm{X_{u|v|}}u|v| + \mathrm{X_{u|w|}}u|w| + \mathrm{X_{v|v|}}v|v| + \mathrm{X_{w|w|}}w|w| + \mathrm{X_{ur}}ur + \mathrm{X_{w|q|}}w|q| \\
& + \mathrm{X_{wq}}wq + \mathrm{X_{uv}}uv + \mathrm{X_{uw}}uw + \mathrm{X_{q|q|}}q|q| + \mathrm{X_{r|r|}}r|r| + \mathrm{X_{q|u|}}q|u| + \mathrm{X_{u|q|}}u|q|, \\
D^{\mathrm{Y}}(\nu) = {} & \mathrm{Y_r}r + \mathrm{Y_v}v + \mathrm{Y_{rr}}r^2 + \mathrm{Y_{|r|}}|r| + \mathrm{Y_{uu}}u^2 + \mathrm{Y_{vv}}v^2 + \mathrm{Y_{|u|}}|u| + \mathrm{Y_{|v|}}|v| \\
& + \mathrm{Y_{u|r|}}u|r| + \mathrm{Y_{r|v|}}r|v| + \mathrm{Y_{v|r|}}v|r| + \mathrm{Y_{u|v|}}u|v| + \mathrm{Y_{v|v|}}v|v| + \mathrm{Y_{ur}}ur \\
& + \mathrm{Y_{vr}}vr + \mathrm{Y_{uv}}uv + \mathrm{Y_{r|r|}}r|r|,
\end{aligned}$$

where damping moment D^{N} is defined by replacing Y with N. The damping force D^{Z} along the heave axis is expressed

$$\begin{aligned}
D^{\mathrm{Z}}(\nu) = {} & \mathrm{Z_q}q + \mathrm{Z_w}w + \mathrm{Z_{qq}}q^2 + \mathrm{Z_{|q|}}|q| + \mathrm{Z_{uu}}u^2 + \mathrm{Z_{|u|}}|u| + \mathrm{Z_{ww}}w^2 + \mathrm{Z_{|w|}}|w| \\
& + \mathrm{Z_{u|q|}}u|q| + \mathrm{Z_{q|w|}}q|w| + \mathrm{Z_{w|q|}}w|q| + \mathrm{Z_{u|w|}}u|w| + \mathrm{Z_{w|w|}}w|w| + \mathrm{Z_{uq}}uq \\
& + \mathrm{Z_{wq}}wq + \mathrm{Z_{uw}}uw + \mathrm{Z_{q|q|}}q|q|,
\end{aligned}$$

where damping moment D^{M} is defined by replacing Z with M. The damping moment D^{K} about the surge axis is expressed

$$D^{\mathrm{K}}(\nu) = 0.$$

Gertler-Hagen

The Gertler-Hagen damping model, as proposed in [26], is from a U.S. Navy technical report intending to standardize the equations of motion for a submarine. The damping forces and moments are

$$
\begin{aligned}
D^{\mathrm{X}}(\nu) &= \mathrm{X}_{\mathrm{qq}}q^2 + \mathrm{X}_{\mathrm{rr}}r^2 + \mathrm{X}_{\mathrm{uu}}u^2 + \mathrm{X}_{\mathrm{vv}}v^2 + \mathrm{X}_{\mathrm{ww}}w^2 + \mathrm{X}_{\mathrm{vv}\overline{\eta}}v^2(\overline{\eta}-1) \\
&\quad + \mathrm{X}_{\mathrm{ww}\overline{\eta}}w^2(\overline{\eta}-1) + \mathrm{X}_{\mathrm{pr}}pr + \mathrm{X}_{\mathrm{vr}}v\mathrm{V}r + \mathrm{X}_{\mathrm{wq}}w\mathrm{V}q, \\
D^{\mathrm{Y}}(\nu) &= \mathrm{Y}_{\mathrm{uu}}u^2 + \mathrm{Y}_{\mathrm{vV}}v\mathrm{V} + \mathrm{Y}_{\mathrm{pq}}pq + \mathrm{Y}_{\mathrm{qr}}qr + + \mathrm{Y}_{\mathrm{up}}up + \mathrm{Y}_{\mathrm{ur}}ur + \mathrm{Y}_{\mathrm{vq}}v\mathrm{V}q \\
&\quad + \mathrm{Y}_{\mathrm{wp}}w\mathrm{V}p + \mathrm{Y}_{\mathrm{wr}}w\mathrm{V}r + \mathrm{Y}_{\mathrm{uv}}uv + \mathrm{Y}_{\mathrm{vw}}v\mathrm{V}w + \mathrm{Y}_{|\mathrm{r}|\mathrm{V_v}}|r|\mathrm{V_v} + \mathrm{Y}_{\mathrm{p}|\mathrm{p}|}p|p| \\
&\quad + \mathrm{Y}_{\mathrm{vV}\overline{\eta}}v\mathrm{V}(\overline{\eta}-1) + \mathrm{Y}_{\mathrm{ur}\overline{\eta}}ur(\overline{\eta}-1) + \mathrm{Y}_{\mathrm{uv}\overline{\eta}}uv(\overline{\eta}-1), \\
D^{\mathrm{Z}}(\nu) &= \mathrm{Z}_{\mathrm{pp}}p^2 + \mathrm{Z}_{\mathrm{rr}}r^2 + \mathrm{Z}_{\mathrm{uu}}u^2 + \mathrm{Z}_{\mathrm{vv}}v^2 + \mathrm{Z}_{\mathrm{u}|\mathrm{w}|}u|w| + \mathrm{Z}_{\mathrm{wV}}w\mathrm{V} + \mathrm{Z}_{\mathrm{pr}}pr \\
&\quad + \mathrm{Z}_{\mathrm{uq}}uq + \mathrm{Z}_{\mathrm{vp}}vp + \mathrm{Z}_{\mathrm{vr}}v\mathrm{V}r + \mathrm{Z}_{\mathrm{uw}}uw + \mathrm{Z}_{|\mathrm{q}|\mathrm{V_w}}|q|\mathrm{V_w} + \mathrm{Z}_{|\mathrm{w}|\mathrm{V}}|w|\mathrm{V} \\
&\quad + \mathrm{Z}_{\mathrm{wV}\overline{\eta}}w\mathrm{V}(\overline{\eta}-1) + \mathrm{Z}_{\mathrm{uq}\overline{\eta}}uq(\overline{\eta}-1) + \mathrm{Z}_{\mathrm{uw}\overline{\eta}}uw(\overline{\eta}-1), \\
D^{\mathrm{K}}(\nu) &= \mathrm{K}_{\mathrm{uu}}u^2 + \mathrm{K}_{\mathrm{uu}\overline{\eta}}u^2(\overline{\eta}-1) + \mathrm{K}_{\mathrm{vV}}v\mathrm{V} + \mathrm{K}_{\mathrm{pq}}pq + \mathrm{K}_{\mathrm{qr}}qr + \mathrm{K}_{\mathrm{up}}up + \mathrm{K}_{\mathrm{ur}}ur \\
&\quad + \mathrm{K}_{\mathrm{vq}}v\mathrm{V}q + \mathrm{K}_{\mathrm{wp}}w\mathrm{V}p + \mathrm{K}_{\mathrm{wr}}w\mathrm{V}r + \mathrm{K}_{\mathrm{uv}}uv + \mathrm{K}_{\mathrm{vw}}v\mathrm{V}w + \mathrm{K}_{\mathrm{p}|\mathrm{p}|}p|p|, \\
D^{\mathrm{M}}(\nu) &= \mathrm{M}_{\mathrm{pp}}p^2 + \mathrm{M}_{\mathrm{rr}}r^2 + \mathrm{M}_{\mathrm{uu}}u^2 + \mathrm{M}_{\mathrm{vv}}v^2 + \mathrm{M}_{\mathrm{qV}}q\mathrm{V} + \mathrm{M}_{\mathrm{wV}}w\mathrm{V} + \mathrm{M}_{\mathrm{pr}}pr \\
&\quad + \mathrm{M}_{\mathrm{uq}}uq + \mathrm{M}_{\mathrm{vp}}vp + \mathrm{M}_{\mathrm{vr}}v\mathrm{V}r + \mathrm{M}_{\mathrm{uw}}uw + \mathrm{M}_{|\mathrm{w}|\mathrm{V}}|w|\mathrm{V} + \mathrm{M}_{\mathrm{q}|\mathrm{q}|}q|q| \\
&\quad + \mathrm{M}_{\mathrm{u}|\mathrm{w}|}u|w| + \mathrm{M}_{\mathrm{wV}\overline{\eta}}w\mathrm{V}(\overline{\eta}-1) + \mathrm{M}_{\mathrm{uq}\overline{\eta}}uq(\overline{\eta}-1) + \mathrm{M}_{\mathrm{uw}\overline{\eta}}uw(\overline{\eta}-1), \\
D^{\mathrm{N}}(\nu) &= \mathrm{N}_{\mathrm{uu}}u^2 + \mathrm{N}_{\mathrm{rV}}r\mathrm{V} + \mathrm{N}_{\mathrm{vV}}v\mathrm{V} + \mathrm{N}_{\mathrm{pq}}pq + \mathrm{N}_{\mathrm{qr}}qr + \mathrm{N}_{\mathrm{up}}up + \mathrm{N}_{\mathrm{ur}}ur \\
&\quad + \mathrm{N}_{\mathrm{vq}}v\mathrm{V}q + \mathrm{N}_{\mathrm{wp}}w\mathrm{V}p + \mathrm{N}_{\mathrm{wr}}w\mathrm{V}r + \mathrm{N}_{\mathrm{uv}}uv + \mathrm{N}_{\mathrm{vw}}v\mathrm{V}w + \mathrm{N}_{\mathrm{r}|\mathrm{r}|}r|r| \\
&\quad + \mathrm{N}_{\mathrm{vV}\overline{\eta}}v\mathrm{V}(\overline{\eta}-1) + \mathrm{N}_{\mathrm{ur}\overline{\eta}}ur(\overline{\eta}-1) + \mathrm{N}_{\mathrm{uv}\overline{\eta}}uv(\overline{\eta}-1)
\end{aligned}
$$

where $\bar{\eta}$ is the ratio of $u_c(n)$ the nominal forward velocity at level flight for the commanded propeller rate n and V the vehicle speed

$$\bar{\eta} = \frac{u_c(n)}{V}.$$

Coe

The Coe damping model, presented in [8], is based on a Taylor series expansion and assumes port/starboard vehicle symmetry. The damping force D^{X} along the surge axis is expressed

$$\begin{aligned} D^{\mathrm{X}}(\nu) = {} & \mathrm{X_{uu}}u^2 + \mathrm{X_{vv}}v^2 + \mathrm{X_{ww}}w^2 + \mathrm{X_{pp}}p^2 + \mathrm{X_{qq}}q^2 \\ & + \mathrm{X_{rr}}r^2 + \mathrm{X_{u|u|}}u|u| + \mathrm{X_{w|w|}}w|w| + \mathrm{X_{q|q|}}q|q|, \end{aligned}$$

where damping forces and moments D^{Z} and D^{M} are defined by replacing X with Z and M. The damping force D^{Y} along the sway axis is expressed

$$D^{\mathrm{Y}}(\nu) = \mathrm{Y_{v|v|}}v|v| + \mathrm{Y_{p|p|}}p|p| + \mathrm{Y_{r|r|}}r|r|,$$

where damping moments D^{K} and D^{N} are defined by replacing Y with K and N.

Prestero

The Prestero damping model, shown in [56], includes axial drag, crossflow drag, and body lift. The damping force D^{X} along the surge axis and the damping force D^{Y} along the sway axis are expressed

$$\begin{aligned} D^{\mathrm{X}}(\nu) &= \mathrm{X_{qq}}q^2 + \mathrm{X_{wq}}wq + \mathrm{X_{rr}}r^2 + \mathrm{X_{vr}}vr + \mathrm{X_{u|u|}}u|u|, \\ D^{\mathrm{Y}}(\nu) &= \mathrm{Y_{v|v|}}v|v| + \mathrm{Y_{pq}}pq + \mathrm{Y_{ur}}ur + \mathrm{Y_{wp}}wp + \mathrm{Y_{uv}}uv + \mathrm{Y_{r|r|}}r|r|, \end{aligned}$$

where damping moment D^{N} is defined by replacing Y with N. The damping force along the heave axis is expressed

$$D^{\mathrm{Z}}(\nu) = \mathrm{Z_{w|w|}}w|w| + \mathrm{Z_{pr}}pr + \mathrm{Z_{uq}}uq + \mathrm{Z_{vp}}vp + \mathrm{Z_{uw}}uw + \mathrm{Z_{q|q|}}q|q|,$$

where damping moment D^{M} is defined by replacing Z with M. The damping moment D^{K} along the surge axis is expressed

$$D^{\mathrm{K}}(\nu) = \mathrm{K_{p|p|}}p|p|.$$

Uncoupled

The uncoupled damping model assumes that motion in each axis is only dependent on velocity along that axis. The damping forces and moments are expressed

$$\begin{aligned} D(\nu) = {} & \mathrm{diag}([\mathrm{X}_u\ \mathrm{Y}_v\ \mathrm{Z}_w\ \mathrm{K}_p\ \mathrm{M}_q\ \mathrm{N}_r])\nu + \mathrm{diag}([\mathrm{X}_{uu}u\ \mathrm{Y}_{vv}v\ \mathrm{Z}_{ww}w\ \mathrm{K}_{pp}p\ \mathrm{M}_{qq}q\ \mathrm{N}_{rr}r])\nu \\ & + \mathrm{diag}([\mathrm{X}_{|u|}\ \mathrm{Y}_{|v|}\ \mathrm{Z}_{|w|}\ \mathrm{K}_{|p|}\ \mathrm{M}_{|q|}\ \mathrm{N}_{|r|}])|\nu| \\ & + \mathrm{diag}([\mathrm{X}_{u|u|}u\ \mathrm{Y}_{v|v|}v\ \mathrm{Z}_{w|w|}w\ \mathrm{K}_{p|p|}p\ \mathrm{M}_{q|q|}q\ \mathrm{N}_{r|r|}r])|\nu|. \end{aligned}$$

Fossen

The Fossen damping model, as proposed in [23], is uncoupled. The Fossen model assumes that the vehicle is performing non-coupled motions and has three planes of symmetry. The damping forces and moments are expressed

$$D(\nu) = \mathrm{diag}([\mathrm{X}_u\ \mathrm{Y}_v\ \mathrm{Z}_w\ \mathrm{K}_p\ \mathrm{M}_q\ \mathrm{N}_r])\nu + \mathrm{diag}([\mathrm{X}_{u|u|}u\ \mathrm{Y}_{v|v|}v\ \mathrm{Z}_{w|w|}w\ \mathrm{K}_{p|p|}p\ \mathrm{M}_{q|q|}q\ \mathrm{N}_{r|r|}r])|\nu|.$$

3.2.4 Control Surface Model Structure

In order to estimate control surface parameters, we follow a similar structure as in Section 3.2.2. We can express a generic control surface model as

$$U_{CS}(\delta) = \begin{bmatrix} U_{CS}^{\mathrm{X}}(\delta) \\ U_{CS}^{\mathrm{Y}}(\delta) \\ U_{CS}^{\mathrm{Z}}(\delta) \\ U_{CS}^{\mathrm{K}}(\delta) \\ U_{CS}^{\mathrm{M}}(\delta) \\ U_{CS}^{\mathrm{N}}(\delta) \end{bmatrix} = \begin{bmatrix} K_{CS}^{\mathrm{X}}\xi_{CS}(\delta) \\ K_{CS}^{\mathrm{Y}}\xi_{CS}(\delta) \\ K_{CS}^{\mathrm{Z}}\xi_{CS}(\delta) \\ K_{CS}^{\mathrm{K}}\xi_{CS}(\delta) \\ K_{CS}^{\mathrm{M}}\xi_{CS}(\delta) \\ K_{CS}^{\mathrm{N}}\xi_{CS}(\delta) \end{bmatrix} = \begin{bmatrix} K_{CS}^{\mathrm{X}} \\ K_{CS}^{\mathrm{Y}} \\ K_{CS}^{\mathrm{Z}} \\ K_{CS}^{\mathrm{K}} \\ K_{CS}^{\mathrm{M}} \\ K_{CS}^{\mathrm{N}} \end{bmatrix} \xi_{CS}(\delta) = K_{CS}\xi_{CS}(\delta),$$

where $\xi_{CS}(\delta) \in \mathbb{R}^{n_{\xi_{CS}} \times 1}$ is a vector that includes all $n_{\xi_{CS}}$ basis functions from all the control surface models and $K_{CS} \in \mathbb{R}^{6 \times n_{\xi_{CS}}}$ is the control surface coefficient matrix. Each control surface model has a unique constant K_{CS} that selects the appropriate basis functions from $\xi_{CS}(\delta)$.

Assumption 3.3. The vector of basis functions, $\xi_{CS}(\delta)$, is bounded if δ is bounded.

3.2.5 Control Surface Model

In this work, we compare the Virginia Tech 690 high-fidelity control surface model created using the DSSP [45] from [8, Appendix A.2.2] and a linear-quadratic control surface model. We propose a linear-quadratic control surface model because the forces and moments generated by the DSSP tool are asymmetric and nonlinear. The linear-quadratic control surface model assumes that the forces and moments due to the control surfaces have a linear and quadratic relationship with δ. This model will be referred to as the linear-quadratic control

surface model (LQCS).

$$U_{CS}(\delta) = \text{diag}([\text{X}_{\delta_e}\ \text{Y}_{\delta_e}\ \text{Z}_{\delta_e}\ \text{K}_{\delta_e}\ \text{M}_{\delta_e}\ \text{N}_{\delta_e}])\delta_e + \text{diag}([\text{X}_{\delta_r}\ \text{Y}_{\delta_r}\ \text{Z}_{\delta_r}\ \text{K}_{\delta_r}\ \text{M}_{\delta_r}\ \text{N}_{\delta_r}])\delta_r$$
$$+ \text{diag}([\text{X}_{\delta_e^2}\ \text{Y}_{\delta_e^2}\ \text{Z}_{\delta_e^2}\ \text{K}_{\delta_e^2}\ \text{M}_{\delta_e^2}\ \text{N}_{\delta_e^2}])\delta_e^2 + \text{diag}([\text{X}_{\delta_r^2}\ \text{Y}_{\delta_r^2}\ \text{Z}_{\delta_r^2}\ \text{K}_{\delta_r^2}\ \text{M}_{\delta_r^2}\ \text{N}_{\delta_r^2}])\delta_r^2.$$

3.2.6 Problem Statement

We want to verify the results from [27] by using two AUVs. We would like to see if one damping model is superior to other models for the case of streamlined AUVs, and further compare two different methods for estimating the parameters of the models. We also seek to compare control surface DSSP predictions with the LQCS estimation model.

Let $\hat{v} \in \mathbb{R}^{6\times 1}$ be the estimated linear and angular velocities, and let $\overline{n}$ represent the number of estimation coefficients in matrix K_D and K_{CS}. As a performance metric, we utilize the root mean square (RMS) error between $\hat{v}$ and v defined in Section 3.5.3, and the number of estimation coefficients, $\overline{n}$, to gauge model complexity.

3.3 Least-Squares Method

Following a similar approach as in [27, 47], we formulate the method for using least-squares in this section. Using Assumption 3.1 (b) in Section 3.2.1, we rewrite (2.5) and represent the damping and control surface terms, $D(\nu(t))$ and $U_{CS}(\delta(t))$, respectively, as

$$P(\nu(t), \delta(t)) = M\dot{\nu}(t) - \mathcal{H}_C(M\nu(t))\nu(t) - \mathcal{G}(R(t)) - U_{Prop}(t), \tag{3.2}$$

where $P(\nu(t), \delta(t)) = D(\nu(t)) + U_{CS}(\delta(t))$. We define the estimate of the damping and control surface terms as $\hat{P}(\nu(t), \delta(t)) = \hat{D}(\nu(t)) + \hat{U}_{CS}(\delta(t)) = \hat{K}_D\xi_D(\nu(t)) + \hat{K}_{CS}\xi_{CS}(\delta(t))$

and the estimation error $\tilde{P}(t)$ as

$$\tilde{P}(t) = \hat{P}(\nu(t), \delta(t)) - P(\nu(t), \delta(t)) \tag{3.3}$$

$$= \hat{K}_D \xi_D(\nu(t)) + \hat{K}_{CS} \xi_{CS}(\delta(t)) - P(\nu(t), \delta(t)). \tag{3.4}$$

Next, we express the variables that change with time in (3.4) as matrices. These matrices contain all the samples collected for that variable. Let

$$\nu_* = [\nu(0), \nu(1), ..., \nu(n_k)] \in \mathbb{R}^{6 \times n_k}, \tag{3.5}$$

$$\delta_* = [\delta(0), \delta(1), ..., \delta(n_k)] \in \mathbb{R}^{2 \times n_k}, \tag{3.6}$$

$$\tilde{P}_* = [\tilde{P}(0), \tilde{P}(1), ..., \tilde{P}(n_k)] \in \mathbb{R}^{6 \times n_k}, \tag{3.7}$$

$$P_* = [P(0), P(1), ..., P(n_k)] \in \mathbb{R}^{6 \times n_k}, \tag{3.8}$$

$$\xi_{D*} = [\xi_D(\nu(0)), \xi_D(\nu(1)), ..., \xi_D(\nu(n_k))] \in \mathbb{R}^{n_{\xi_D} \times n_k}, \tag{3.9}$$

$$\xi_{CS*} = [\xi_{CS}(\delta(0)), \xi_{CS}(\delta(1)), ..., \xi_{CS}(\delta(n_k))] \in \mathbb{R}^{n_{\xi_{CS}} \times n_k} \tag{3.10}$$

be matrix representations of the time series, where n_k is the number of samples collected, n_{ξ_D} is the number of elements in the damping basis vector, and $n_{\xi_{CS}}$ is the number of elements in the control surface basis vector. By substituting the matrix time series equations (3.5) - (3.10), using the vec$(\cdot)$ operator defined in Definition 2.2, using the Kronecker product

defined in Definition 2.3, and using Proposition 2.4, equation (3.4) is expressed as

$$\begin{aligned}
\tilde{P}_* &= \hat{K}_D \xi_{D*} + \hat{K}_{CS} \xi_{CS*} - P_* \\
&= \begin{bmatrix} \hat{K}_D & \hat{K}_{CS} \end{bmatrix} \begin{bmatrix} \xi_{D*} \\ \xi_{CS*} \end{bmatrix} - P_* \\
&= \hat{K}\xi_* - P_*, \\
\tilde{P}_*^\mathsf{T} &= \xi_*^\mathsf{T} \hat{K}^\mathsf{T} - P_*^\mathsf{T}, \\
\mathrm{vec}(\tilde{P}_*^\mathsf{T}) &= \mathrm{vec}(\xi_*^\mathsf{T} \hat{K}^\mathsf{T} - P_*^\mathsf{T}) \\
&= \mathrm{vec}(\xi_*^\mathsf{T} \hat{K}^\mathsf{T}) - \mathrm{vec}(P_*^\mathsf{T}) \\
&= (I_6 \otimes \xi_*^\mathsf{T}) \mathrm{vec}(\hat{K}^\mathsf{T}) - \mathrm{vec}(P_*^\mathsf{T}),
\end{aligned} \tag{3.11}$$

where $I_6 \in \mathbb{R}^{6\times 6}$ is the identity matrix, $\hat{K} = \begin{bmatrix} \hat{K}_D & \hat{K}_{CS} \end{bmatrix} \in \mathbb{R}^{6\times n_\xi}$, $\xi_* = \begin{bmatrix} \xi_{D*} \\ \xi_{CS*} \end{bmatrix} \in \mathbb{R}^{n_\xi \times 1}$, and $n_\xi = n_{\xi_D} + n_{\xi_{CS}}$ which represents the total number of basis functions from the damping and control surface models.

To represent different damping and control surface models, we introduce a masking matrix $M_m \in \mathbb{B}^{\bar{n}\times 6n_\xi}$, where $\mathbb{B} = \{0, 1\}$. That is, M_m is a matrix composed of only zeros and ones. Each row of M_m has exactly one non-zero element, which is equal to one. The non-zero element selects the corresponding basis function of the specific model. Equation (3.11) can be expressed with this masking matrix as

$$\mathrm{vec}(\tilde{P}_*^\mathsf{T}) = (I_6 \otimes \xi_*^\mathsf{T}) M_m^\mathsf{T} M_m \mathrm{vec}(\hat{K}^\mathsf{T}) - \mathrm{vec}(P_*^\mathsf{T}). \tag{3.12}$$

Using a change of variables, we setup the synthesis model

$$\tilde{\sigma} = \text{vec}(\tilde{P}_*^{\mathsf{T}}) \in \mathbb{R}^{6n_k},$$

$$\sigma = \text{vec}(P_*^{\mathsf{T}}) \in \mathbb{R}^{6n_k},$$

$$\Xi = (I_6 \otimes \xi_*^{\mathsf{T}}) M_m^{\mathsf{T}} \in \mathbb{R}^{6n_k \times \overline{n}},$$

$$\hat{\kappa} = M_m \text{vec}(\hat{K}^{\mathsf{T}}) \in \mathbb{R}^{\overline{n}}, \tag{3.13}$$

$$\tilde{\sigma} = \Xi\hat{\kappa} - \sigma, \tag{3.14}$$

where $\tilde{\sigma} \in \mathbb{R}^{6n_k}$ is the vector of residual forces and moments, $\Xi \in \mathbb{R}^{6n_k \times \overline{n}}$ contains all basis functions for a particular damping model and control surface model, $\hat{\kappa} \in \mathbb{R}^{\overline{n}}$ is the set of coefficients, and $\overline{n}$ is the number of estimation coefficients, which we refer to as the model complexity. The original coefficient matrix $\hat{K}$ is recovered from $\hat{\kappa}$ using

$$\hat{K} = \text{vec}^{-1}(M_m^{\mathsf{T}}\hat{\kappa})^{\mathsf{T}}, \tag{3.15}$$

where $\text{vec}^{-1}(\cdot)$ is defined in Definition 2.2.

Our goal with the least-squares method is to find the coefficient vector $\hat{\kappa}$ that minimizes residual forces and moments column vector $\tilde{\sigma}$ in (3.14). In order to use the least-squares method, $\dot{\nu}$ must be instrumented or inferred from other measurements.

3.4 Adaptive Identifier Method

The adaptive identifier that we use for damping and control surface model estimation is a modest specialization of the adaptive identifier proposed in [48] and an extension of the identifier in [27]. We briefly describe the identifier. For notational convenience, explicit dependence on time is omitted in this section except for the initial time.

3.4.1 Adaptive Identification System

Let $\hat{\nu} \in \mathbb{R}^{6\times 1}$ be the estimated linear and angular velocities. For this section, we assume the damping forces and moments $D(\nu)$ can be expressed as $K_D\xi_D(\nu)$. We also assume the control surface forces and moments $U_{CS}(\delta)$ can be expressed as $K_{CS}\xi_{CS}(\delta)$. Of course, the assumptions $D(\nu) = K_D\xi_D(\nu)$ and $U_{CS}(\delta) = K_{CS}\xi_{CS}(\delta)$ are only approximations of the actual forces and moments, but as shown in our experimental results, the assumptions work reasonably well. Using Assumption 3.1 (a) and (b) from Section 3.2.1, Assumption 3.2 from Section 3.2.2, and Assumption 3.3 from Section 3.2.4, consider the following adaptive identifier for the damping and control surface coefficients based on equation (2.5)

$$M\dot{\hat{\nu}} = \mathcal{H}_C(M\nu)\nu + \hat{K}_D\xi_D(\nu) + \mathcal{G}(R) + \hat{K}_{CS}\xi_{CS}(\delta) + U_{Prop} - a\Delta\nu, \tag{3.16}$$

$$\dot{\hat{K}}_D = -\gamma_D\Delta\nu\xi_D^{\mathsf{T}}(\nu), \tag{3.17}$$

$$\dot{\hat{K}}_{CS} = -\gamma_{CS}\Delta\nu\xi_{CS}^{\mathsf{T}}(\delta), \tag{3.18}$$

where $\hat{K}_D\xi_D(\nu)$ is the estimate of the damping term $D(\nu)$; $\hat{K}_{CS}\xi_{CS}(\delta)$ is the estimate of the control surface term $U_{CS}(\delta)$; $\Delta\nu = \hat{\nu} - \nu$; $\Delta K_D = \hat{K}_D - K_D$; $\Delta K_{CS} = \hat{K}_{CS} - K_{CS}$; a, γ_D, and $\gamma_{CS} \in \mathbb{R}_+$; and $\hat{\nu}(t_0) = \nu(t_0)$. We define an error system by subtracting equation (2.5) from (3.16)

$$\begin{aligned} M\dot{\hat{\nu}} - M\dot{\nu} &= \mathcal{H}_C(M\nu)\nu + \hat{K}_D\xi_D(\nu) + \mathcal{G}(R) + \hat{K}_{CS}\xi_{CS}(\delta) + U_{Prop} - a\Delta\nu \\ &\quad - \mathcal{H}_C(M\nu)\nu - K_D\xi_D(\nu) - \mathcal{G}(R) - K_{CS}\xi_{CS}(\delta) - U_{Prop} \\ &= (\hat{K}_D - K_D)\xi_D(\nu) + (\hat{K}_{CS} - K_{CS})\xi_{CS}(\delta) - a\Delta\nu \end{aligned}$$

from which the error dynamics are expressed

$$M\dot{\Delta}\nu = \Delta K_D\xi_D(\nu) + \Delta K_{CS}\xi_{CS}(\delta) - a\Delta\nu. \tag{3.19}$$

Since K_D and K_{CS} are constant, $\dot{\Delta}K_D = \dot{\hat{K}}_D$ and $\dot{\Delta}K_{CS} = \dot{\hat{K}}_{CS}$. Also, M^{-1} exists because M is a positive-definite matrix. Solving for $\dot{\Delta}\nu$ by multiplying both sides of equation (3.19) by M^{-1} and using (3.17) and (3.18) yields the error system

$$\dot{\Delta}\nu = M^{-1}(\Delta K_D \xi_D(\nu) + \Delta K_{CS}\xi_{CS}(\delta) - a\Delta\nu), \tag{3.20a}$$

$$\dot{\Delta}K_D = -\gamma_D \Delta\nu \xi_D^{\mathsf{T}}(\nu), \tag{3.20b}$$

$$\dot{\Delta}K_{CS} = -\gamma_{CS}\Delta\nu\xi_{CS}^{\mathsf{T}}(\delta). \tag{3.20c}$$

We show that the error system (3.20a) - (3.20c) is uniformly stable at the origin. Using Barbalat's Lemma, we show that $\lim_{t\to\infty}\Delta\nu = 0_{6\times 1}$. Thus the estimated linear and angular velocities converge to the measured values. However, this does not guarantee convergence of the model coefficients to the real coefficients.

3.4.2 Convergence of the Error System

The proof presented here is a specialization of the more general results that appear in [48] and is an extension of the proof given in [27].

Proposition 3.4. *Consider the equilibrium point at the origin* $\Delta\nu = 0_{6\times 1}$, $\Delta K_D = 0_{6\times n_{\xi_D}}$, $\Delta K_{CS} = 0_{6\times n_{\xi_{CS}}}$ *for the nonlinear, nonautonomous system* (3.20). *If* a, γ_D, $\gamma_{CS} \in \mathbb{R}_+$, *and using Assumption 3.1 (a) and (b) from Section 3.2.1, Assumption 3.2 from Section 3.2.2, and Assumption 3.3 from Section 3.2.4, then the*

1. *system* (3.20) *is uniformly stable at the origin*
2. $\lim_{t\to\infty}\Delta\nu = 0_{6\times 1}$
3. $\lim_{t\to\infty}\dot{\Delta}K_D = 0_{6\times n_{\xi_D}}$ *and* $\lim_{t\to\infty}\dot{\Delta}K_{CS} = 0_{6\times n_{\xi_{CS}}}$.

Proof. Choose the following candidate Lyapunov function for the error system (3.20)

$$V = \frac{1}{2}\Delta\nu^{\mathsf{T}} M \Delta\nu + \frac{1}{2\gamma_D}\operatorname{tr}(\Delta K_D \Delta K_D^{\mathsf{T}}) + \frac{1}{2\gamma_{CS}}\operatorname{tr}(\Delta K_{CS}\Delta K_{CS}^{\mathsf{T}}). \tag{3.21}$$

Equation (3.21) is positive-definite, decrescent, smooth, and thus V is equal to zero if and only if $\Delta\nu = 0_{6\times 1}$, $\Delta K_D = 0_{6\times n_{\xi_D}}$, and $\Delta K_{CS} = 0_{6\times n_{\xi_{CS}}}$. Calculating the time derivative along trajectories from equation (3.21) yields

$$\dot{V} = \Delta\nu^{\mathsf{T}} M \dot{\Delta}\nu + \frac{1}{\gamma_D}\operatorname{tr}(\Delta K_D \dot{\Delta} K_D^{\mathsf{T}}) + \frac{1}{\gamma_{CS}}\operatorname{tr}(\Delta K_{CS}\dot{\Delta} K_{CS}^{\mathsf{T}}). \tag{3.22}$$

By substituting (3.20) into (3.22), we write

$$\begin{aligned}
\dot{V} &= \Delta\nu^{\mathsf{T}} M \dot{\Delta}\nu + \frac{1}{\gamma_D}\operatorname{tr}(\Delta K_D \dot{\Delta} K_D^{\mathsf{T}}) + \frac{1}{\gamma_{CS}}\operatorname{tr}(\Delta K_{CS}\dot{\Delta} K_{CS}^{\mathsf{T}}) \\
&= \Delta\nu^{\mathsf{T}} M \left[M^{-1}(\Delta K_D \xi_D(\nu) + \Delta K_{CS}\xi_{CS}(\delta) - a\Delta\nu)\right] \\
&\quad + \frac{1}{\gamma_D}\operatorname{tr}(\Delta K_D \dot{\Delta} K_D^{\mathsf{T}}) + \frac{1}{\gamma_{CS}}\operatorname{tr}(\Delta K_{CS}\dot{\Delta} K_{CS}^{\mathsf{T}}) \\
&= \Delta\nu^{\mathsf{T}}\Delta K_D \xi_D(\nu) + \Delta\nu^{\mathsf{T}}\Delta K_{CS}\xi_{CS}(\delta) - a\Delta\nu^{\mathsf{T}}\Delta\nu \\
&\quad + \frac{1}{\gamma_D}\operatorname{tr}(\Delta K_D \left[-\gamma_D \Delta\nu \xi_D^{\mathsf{T}}(\nu)\right]^{\mathsf{T}}) + \frac{1}{\gamma_{CS}}\operatorname{tr}(\Delta K_{CS}\left[-\gamma_{CS}\Delta\nu\xi_{CS}^{\mathsf{T}}(\delta)\right]^{\mathsf{T}}) \\
&= \Delta\nu^{\mathsf{T}}\Delta K_D \xi_D(\nu) + \Delta\nu^{\mathsf{T}}\Delta K_{CS}\xi_{CS}(\delta) - a\Delta\nu^{\mathsf{T}}\Delta\nu - \operatorname{tr}(\Delta K_D \xi_D(\nu)\Delta\nu^{\mathsf{T}}) \\
&\quad - \operatorname{tr}(\Delta K_{CS}\xi_{CS}(\delta)\Delta\nu^{\mathsf{T}}).
\end{aligned}$$

Using the property $\text{tr}(AB) = \text{tr}(BA)$ for conformable matrices, we can express $\dot{V}$ as

$$\begin{aligned}\dot{V} &= \Delta\nu^{\mathsf{T}}\Delta K_D\xi_D(\nu) + \Delta\nu^{\mathsf{T}}\Delta K_{CS}\xi_{CS}(\delta) - a\Delta\nu^{\mathsf{T}}\Delta\nu - \text{tr}(\Delta\nu^{\mathsf{T}}\Delta K_D\xi_D(\nu)) \\ &\quad - \text{tr}(\Delta\nu^{\mathsf{T}}\Delta K_{CS}\xi_{CS}(\delta)) \\ &= \Delta\nu^{\mathsf{T}}\Delta K_D\xi_D(\nu) + \Delta\nu^{\mathsf{T}}\Delta K_{CS}\xi_{CS}(\delta) - a\Delta\nu^{\mathsf{T}}\Delta\nu - \Delta\nu^{\mathsf{T}}\Delta K_D\xi_D(\nu) - \Delta\nu^{\mathsf{T}}\Delta K_{CS}\xi_{CS}(\delta) \\ &= -a\Delta\nu^{\mathsf{T}}\Delta\nu. \end{aligned} \tag{3.23}$$

$\dot{V}$ is negative semi-definite because it is not a function of all the state variables. By Lyapunov's Direct Method (Theorem 2.9), we conclude that the error system (3.20) is uniformly stable at the origin.

To show that $\lim_{t\to\infty}\Delta\nu = 0_{6\times 1}$, we use Barbalat's Lemma (Lemma 2.11). We need to show that $\Delta\nu$, $\dot{\Delta}\nu \in \mathcal{L}^\infty$ and $\Delta\nu \in \mathcal{L}^p$. Equations (3.21) and (3.23) show that $\Delta\nu$, ΔK_D, and ΔK_{CS} are bounded by Lyapunov's Direct Method. Therefore, $\Delta\nu \in \mathcal{L}^\infty$. Equations (3.21) and (3.23) also imply that V is bounded below and non-increasing. Using Lemma 2.7, we conclude that the $\lim_{t\to\infty} V$ exists. Integrating equation (3.23) from zero to t and taking the limit of t to infinity shows that $\Delta\nu \in \mathcal{L}^2$. Finally, we know that ν, $\Delta\nu$, ΔK_D, and ΔK_{CS} are bounded, where K_D and K_{CS} are constant. This implies that $\hat{\nu}$, $\hat{K}_D$, and $\hat{K}_{CS}$ are bounded. With $\xi(\nu)$ bounded, we conclude from the first equation in (3.20) that $\dot{\Delta}\nu \in \mathcal{L}^\infty$. Thus, $\lim_{t\to\infty}\Delta\nu = 0_{6\times 1}$ by Barbalat's Lemma.

From equation (3.23) and the fact that $\Delta\nu$ converges to 0, we infer that $\lim_{t\to\infty}\dot{V} = 0$. Since $\dot{V}$ converges to 0, ΔK_D and ΔK_{CS} converge to constants and $\lim_{t\to\infty}\dot{\Delta}K_D = 0_{6\times n_{\xi_D}}$ and $\lim_{t\to\infty}\dot{\Delta}K_{CS} = 0_{6\times n_{\xi_{CS}}}$. □

Remark 3.5. The previous theorem only guarantees that damping model and control surface model coefficients converge to constant values. The theorem does not guarantee convergence to the true model parameters.

Table 3.1: Properties of the Virginia Tech 690 and Virginia Tech 690S AUVs

Property	690 AUV	690S AUV
Diameter	6.9 inches	6.9 inches
Length	81.0 inches	60.4 inches
Dry Weight	91.4 pounds	60.6 pounds

3.5 Experimental Results

3.5.1 Experimental Environment

The Virginia Tech 690 AUV (690 AUV) and the Virginia Tech 690S AUV (690S AUV) shown in Figure 3.1 were used to acquire the experimental data. The 690 AUV is described in [46], and the 690S AUV is a shorter variant with different physical properties (see Table 3.1). Field trials were conducted at Claytor Lake, in Dublin, Virginia, where there is negligible water current. We make the reasonable assumption that the water current is zero in these field trials. In this study, we use the 690 AUV to compare the different damping and control surface models. We also use a data set from the 690S AUV to verify our results on a separate vehicle.

Both AUVs have a single propeller at the stern of the vehicle and four control surfaces in a cruciform pattern at the tail. The 690 AUV is equipped with a Doppler velocity log (DVL) that measures bottom relative velocity. The linear velocities for the 690S AUV are estimated from a combination of propeller rotational rate, which is used to estimate body-relative surge velocity, and rate of change of depth measurements, which is used to estimate inertial vertical velocity $\dot{z}$. The 690 AUV and the 690S AUV have an attitude and heading reference sensor (AHRS) that measures attitude, body relative rotation rates, and linear accelerations. Neither vehicle has a sensor that measures angular acceleration. Angular acceleration is estimated by finite differences of angular velocity measurements. The 690 AUV and the 690S AUV employ H_∞ autopilots that minimize pitch and yaw coupling

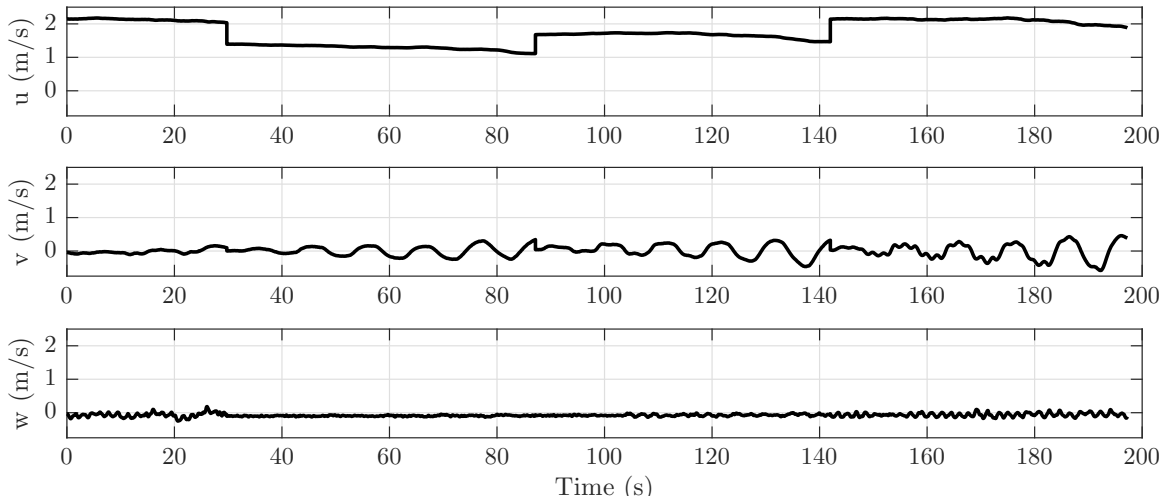

Figure 3.2: Translation velocity damping parameter estimation data set for the 690 AUV

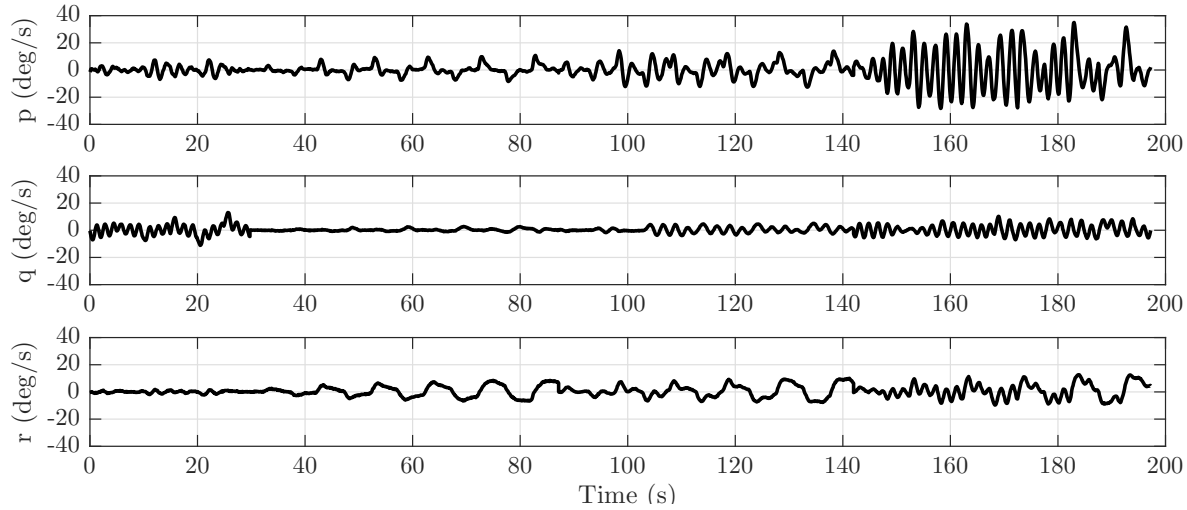

Figure 3.3: Rotational velocity damping parameter estimation data set for the 690 AUV

[53].

In the proposed least-squares and adaptive identifier methods from Sections 3.3 and 3.4, the forces and moments due to inertia, added mass, propulsion, gravity and buoyancy are assumed to be known. The mass matrix M is composed of both mass of the vehicle M_{rb} and added mass M_a where $M = M_{rb} + M_a$ [23]. The mass and inertia of the vehicles are estimated from direct measurements and computed mass distribution from computer-aided design (CAD) software. The inertia tensors are presented in the Appendix Tables A.2 and

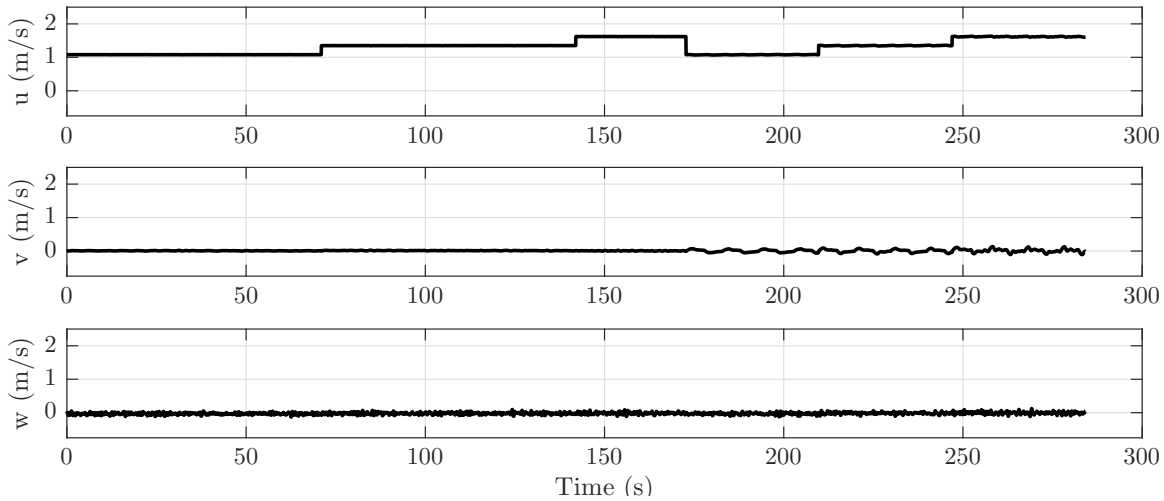

Figure 3.4: Translation velocity damping parameter estimation data set for the 690S AUV

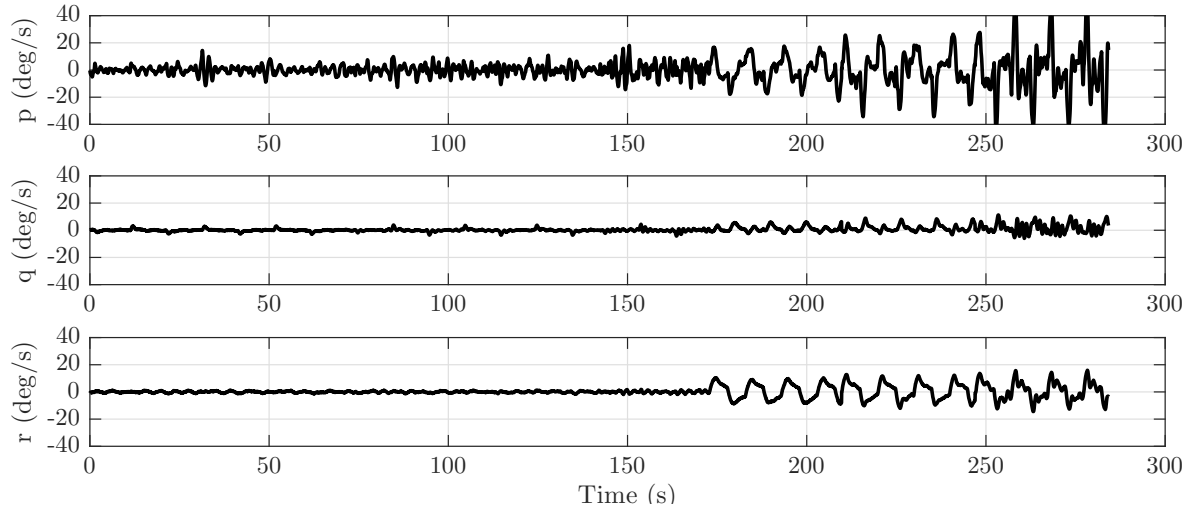

Figure 3.5: Rotational velocity damping parameter estimation data set for the 690S AUV

A.3. The added mass for each vehicle M_a, given in the Appendix Tables A.4 and A.5, are derived from that of a prolate spheroid with the same volume and aspect ratios to that of the AUV [4, 23, 31, 34]. Terms due to gravity and buoyancy are obtained from direct measurements and computed values from CAD software.

The origin for the coordinate system is at the vehicle's center of buoyancy. The propellers used in the experiments were designed using low Reynolds number theory [55]. The 690 AUV and 690S AUV propellers both have three blades and a diameter of 4.73 inches and

3.94 inches, respectively. The propeller model comes from [9] and defines the thrust and torque generated by the propeller. The thrust coefficient K_T, torque coefficient K_Q, and wake fraction are emprically determined as in [8, 18, 55] and are shown in the Appendix Tables A.1, A.6 and A.7. The four control surfaces are the same for both vehicles. The control surface shape is a NACA 0010 airfoil [4] with a chord of 2.18 inches, a leading edge span of 2.00 inches, and a trailing edge span of 2.36 inches. For both vehicles, the DSSP model for the forces and moments due to the control surfaces is derived in [8] and is found in the Appendix Table A.8.

3.5.2 Data Sets

Data were acquired during experiments performed at Claytor Lake, in Dublin, Virginia. The data sets collected from the experiments were partitioned into a set that is used for estimating model parameters and another set that is used to validate estimated parameters. The data set used for parameter estimation is shown in Figures 3.2, 3.3, 3.4, and 3.5.

The 690 AUV estimation data set is a concatenation of four independent data sets. The first data set is composed of a series of step changes in depth commands at a propeller speed of 2600 rpm, and the three remaining sets are composed of a series of step changes in yaw commands at propeller speeds of 1800, 2133, and 2600 rpm, respectively. The concatenation produces discontinuities three times in the data. The 690S AUV estimation data set is a concatenation of six independent data sets. The data set is composed of step changes in depth and yaw at a propeller speed of 1000, 1250, and 1500 rpm. The concatenation produces discontinuities five times in the data.

With the parameter estimation data sets, we apply the least-squares synthesis model (3.13) and (3.14) to find the value of $\hat{\kappa}$ that minimizes the residual force for each hydrodynamic damping model and control surface model that is described in Section 3.2.3 and 3.2.5.

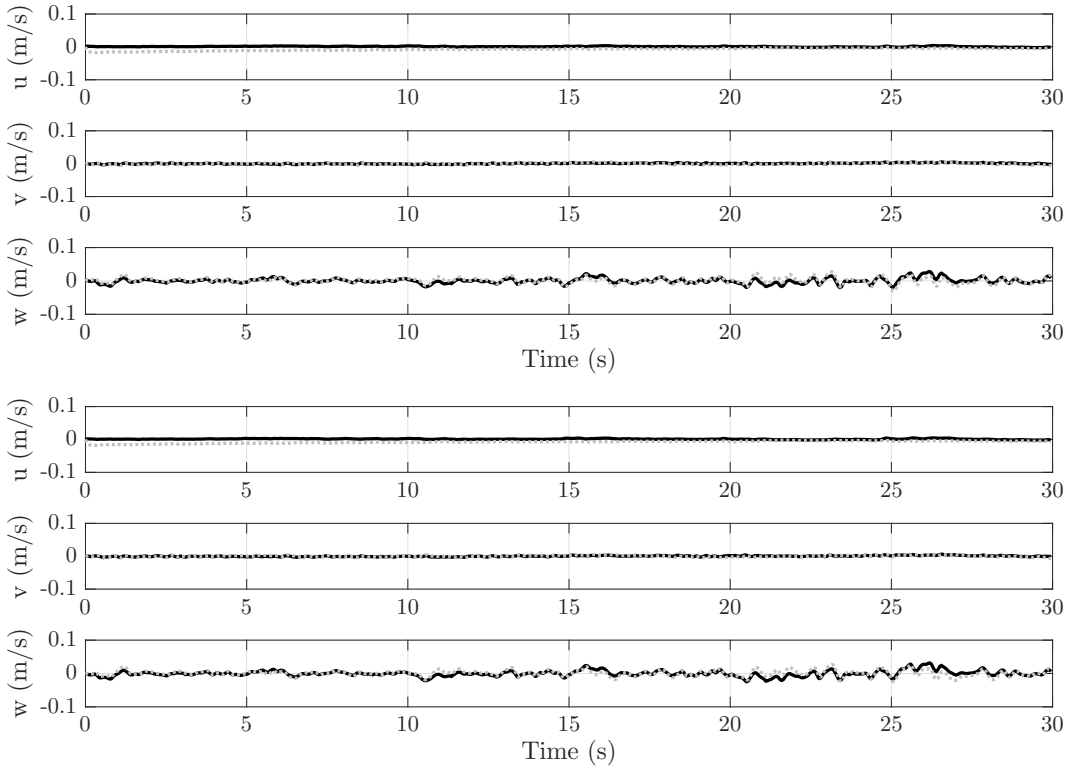

Figure 3.6: Translation velocity error $\Delta\nu$ validation plots for the 690 AUV linear damping model with a DSSP control surface model (top) and linear-quadratic control surface model (bottom). The solid black line is the least-squares estimation error. The dashed grey line is the adaptive identifier estimation error.

From the minimizing value of $\hat{\kappa}$, we construct the coefficient matrix $\hat{K}$ for each model using the inverse equation (3.15).

After estimating the different model parameters, we use the verification data to evaluate the models. The 690 AUV data set reserved for validation has two sections. The first section consists of a series of step changes in depth with constant propeller speed 2133 rpm. The second section contains step changes in yaw at a propeller speed of 1800 rpm. The linear damping model results for step changes in depth are shown in Figures 3.6 and 3.7.

The 690S AUV data set reserved for validation has three sections. The data set is composed of step changes in depth and yaw at a propeller speed of 1000 and 1250 rpm. The linear damping model results for step changes in depth are shown in Figures 3.8 and 3.9.

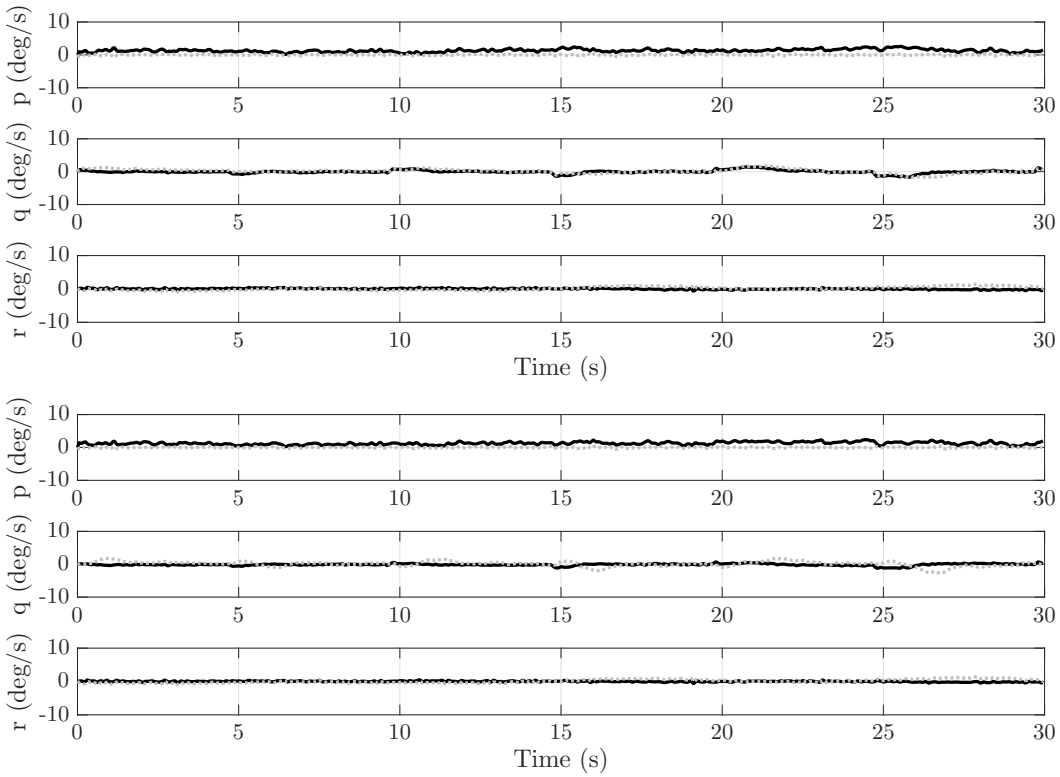

Figure 3.7: Rotational velocity error $\Delta\nu$ validation plots for the 690 AUV linear damping model with a DSSP control surface model (top) and linear-quadratic control surface model (bottom). The solid black line is the least-squares estimation error. The dashed grey line is the adaptive identifier estimation error.

For the other damping models, we show only numerical performance metric results that are described in Section 3.5.3.

3.5.3 Experimental Results

The performance metrics to compare models are model complexity $\overline{n}$, and the root mean square (RMS) error of the linear and the angular velocities. The RMS error is defined by

$$J(\Delta\nu) = \sqrt{\frac{1}{6n_k}\sum_{i=1}^{6n_k}(\text{vec}(\Delta\nu))_i^2}, \tag{3.24}$$

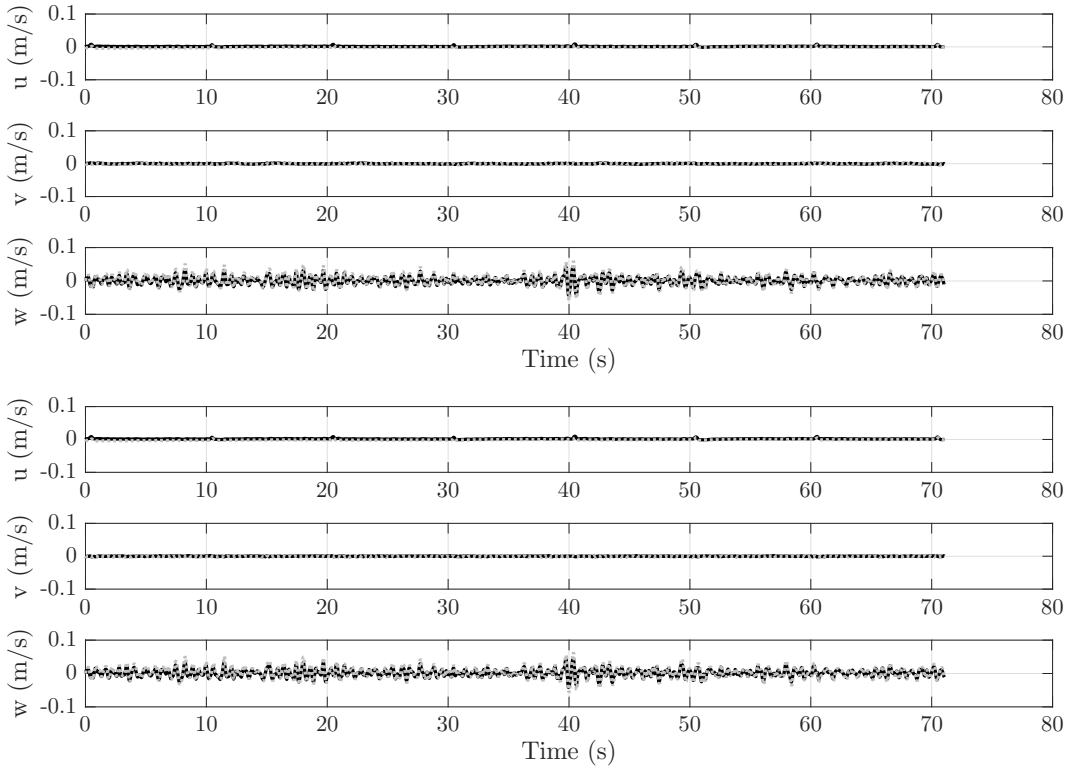

Figure 3.8: Translation velocity error $\Delta\nu$ validation plots for the 690S AUV linear damping model with a DSSP control surface model (top) and linear-quadratic control surface model (bottom). The solid black line is the least-squares estimation error. The dashed grey line is the adaptive identifier estimation error.

where n_k is the number of time samples, $\Delta\nu$ is a 6 element velocity error vector that is a function of time and $\text{vec}(\Delta\nu) \in \mathbb{R}^{6n_k}$ stacks the vectors into one column. Essentially, the RMS error quantifies the error between the predicted and measured velocities where the RMS error unit of measurement is a combination of linear velocities in m/s and angular velocities in deg/s.

For the least-squares method, all the hydrodynamic damping and control surface model coefficients are estimated by (3.14) and (3.15) by minimizing the residual forces and moments from the estimation data set. Using the estimated model parameters $\hat{K}$ and the basis functions ξ from the validation data set, the linear and angular velocities are predicted, and the RMS error for each model is calculated. Similarly for the adaptive identifier method, the

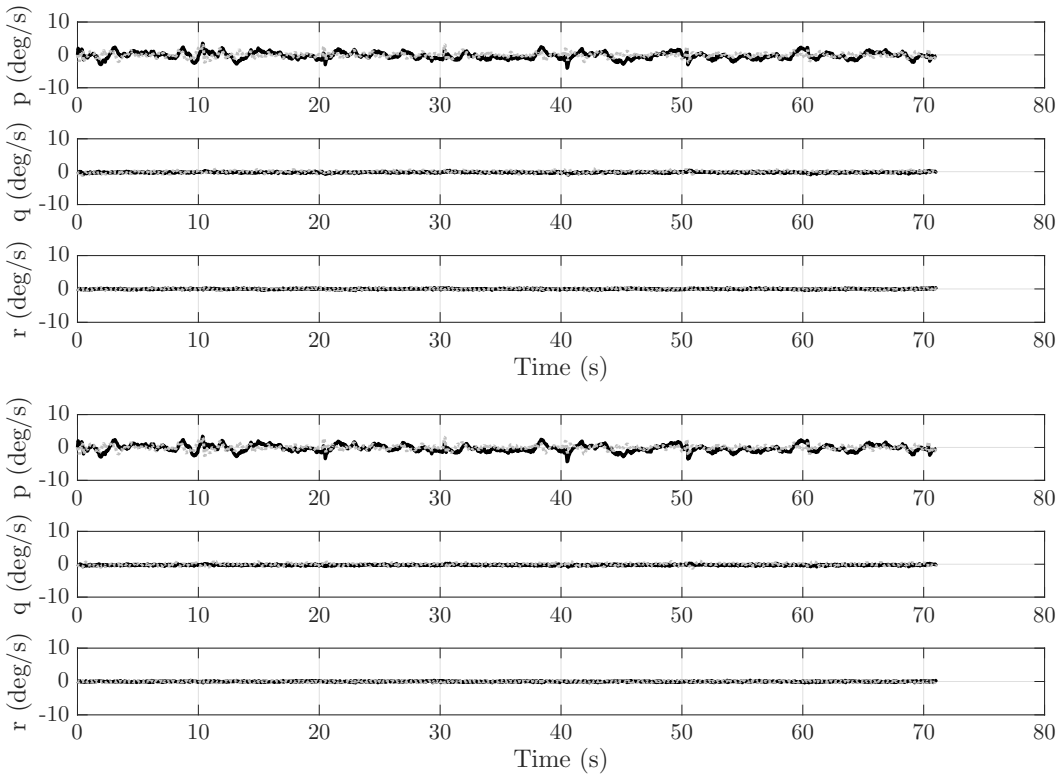

Figure 3.9: Rotational velocity error $\Delta\nu$ validation plots for the 690S AUV linear damping model with a DSSP control surface model (top) and linear-quadratic control surface model (bottom). The solid black line is the least-squares estimation error. The dashed grey line is the adaptive identifier estimation error.

model parameters of the identifier are initialized, and the parameters are adaptively updated using (3.20) and the forces and moments from the validation data set. The adaptive identifier inherently predicts the linear and angular velocities for the validation data set and guarantees velocity convergence under certain assumptions (See Proposition 3.4).

Table 3.2 shows the least-squares and adaptive identifier RMS errors between the predicted and measured velocities for the hydrodynamic damping models using the DSSP control surface model, and Table 3.3 shows the RMS velocity errors for hydrodynamic damping models using the LQCS model. Both tables are ordered by the total number of estimation coefficients $\overline{n}$ for the specific hydrodynamic damping model and control surface model. The two control surface models are labeled DSSP and LQCS for the control surface model gen-

Table 3.2: Root mean square velocity error values for different hydrodynamic damping models using the DSSP model

Damping Model	$\overline{n}$	690 AUV DSSP Model LS error	690 AUV DSSP Model AI error	690S AUV DSSP Model LS error	690S AUV DSSP Model AI error
McFarland-Whitcomb	216	0.35	0.37	0.53	0.36
Pitch-Yaw	100	1.09	1.30	1.81	2.19
Gertler-Hagen	88	0.48	0.37	0.53	0.33
Linear	36	0.49	0.41	0.55	0.40
Coe	33	1.00	1.41	1.56	2.04
Prestero	30	1.15	1.45	1.92	2.13
Uncoupled	24	1.38	1.35	1.65	1.62
Fossen	12	1.48	1.38	1.93	1.95

erated by the DSSP and linear-quadratic control surface model, respectively. Table 3.2 and Table 3.3 also show the RMS errors for the 690 AUV and the 690S AUV. Both vehicles show similar error trends depending on damping model, estimation technique and control surface model.

From Table 3.2 and 3.3, the adaptive identifier method produces similar RMS errors when compared to the least-squares method. For estimating a vehicle's linear and angular velocities, the similar error trends using both methods implies that the specialized adaptive identifier derived in Section 3.4 is an effective alternate velocity estimation method. However, for estimating the damping and control surface model coefficients, the convergence of the model parameters to the true values using the adaptive identifier is not guaranteed.

From Table 3.2 and 3.3, we can make conclusions about the relative performance of the hydrodynamic damping models. The Fossen and uncoupled damping models assume that the damping forces and moments are uncoupled, in that only the velocity in one dimension contributes to the force in that dimension. The error for the Fossen and uncoupled model is high, relative to other models, in most cases. However, the Fossen and uncoupled models have the fewest number of coefficients. A reasonable hypothesis is that the poor performance

Table 3.3: Root mean square velocity error values for different hydrodynamic damping models using the LQCS model

Damping Model	$\overline{n}$	690 AUV LQCS Model LS error	690 AUV LQCS Model AI error	690S AUV LQCS Model LS error	690S AUV LQCS Model AI error
McFarland-Whitcomb	240	0.32	0.33	0.51	0.38
Pitch-Yaw	124	0.82	0.76	1.57	1.44
Gertler-Hagen	112	0.33	0.33	0.53	0.35
Linear	60	0.45	0.37	0.54	0.41
Coe	57	0.67	0.79	1.32	1.43
Prestero	54	0.83	0.83	1.64	1.47
Uncoupled	48	1.02	0.83	1.38	1.15
Fossen	36	1.04	0.83	1.57	1.37

when compared to the other models can be attributed to the coupled nature of hydrodynamic damping.

The Prestero and Coe hydrodynamic damping models attempt to model coupling between axes, but differ in exactly which terms are included and which are eliminated. They assume the third and fourth fewest number of coefficients. Both models assume the vehicle has two axes of symmetry. However, from Table 3.2 and 3.3, the Coe and Prestero model RMS errors are higher than other models with more coefficients and are similar to the Fossen and uncoupled model.

The pitch-yaw damping model performs similar to the four hydrodynamic damping models with the fewest number of coefficients. The model is generated by eliminating terms which are out of plane in independent pitch and yaw models. Consequently, the model assumes no x-axis damping moment will occur and cannot account for any residual x-axis moment. An improved model would allow for x-axis damping moment coefficients and reduce the residual RMS error.

The McFarland-Whitcomb, Gertler-Hagen, and linear damping models have similar error values for both vehicles which supports the results from [27] and [47]. These three damping

models consistently give the lowest RMS error using the least-squares or adaptive identifier estimation method. The Gertler-Hagen and the McFarland-Whitcomb models include numerous coupling and second order terms that do not appear in the other models. The McFarland-Whitcomb model assumes a quadratic relationship between force and velocity while the linear model assumes that the relationship is linear. The relationship is actually more complicated, but from Table 3.2 and 3.3 we can see that the linear and quadratic assumptions give low RMS error. The linear model, with significantly fewer model coefficients than the McFarland-Whitcomb and Gertler-Hagen models, performs well and can be a compromise between model complexity and accuracy.

Comparing Table 3.2 and 3.3, the velocity estimation using the LQCS model instead of the DSSP control surface model either improves or does not significantly change the RMS error. The Coe, Prestero, uncoupled, pitch-yaw, and Fossen damping models have a lower RMS error using the LQCS model. For the McFarland-Whitcomb, Gertler-Hagen, and linear damping models, estimation using the LQCS model does not significantly change the RMS error. These three hydrodynamic damping models can adequately represent the residual forces and moments on the AUVs and adding extra LQCS parameters to the estimation does not improve estimation performance. Thus, a LQCS model can be used to estimate forces and moments due to fins rather than employing a high-fidelity control surface model like the DSSP.

3.6 Conclusion

In this chapter, we verify and expand the results from [27] by using multiple vehicles. For vehicle velocity estimation, the least-squares and adaptive identifier methods produce similar results and either is a suitable estimation technique. The McFarland-Whitcomb and Gertler-Hagen hydrodynamic damping models give the most accurate velocity predictions for the

data sets analyzed in this work but have the most number of model coefficients. The linear damping model, with significantly fewer model coefficients than the McFarland-Whitcomb and Gertler-Hagen models, performs well and can be a compromise between model complexity and accuracy. The other damping models, which all have lower complexity due to fewer coefficients, and which invoke unjustified assumptions about the dynamics of the vehicles (e.g., no coupling between axes), perform worse than the McFarland-Whitcomb, Gertler-Hagen, and linear models.

We extend the estimation results from [27] to include control surface parameter estimation. For other parameters of a dynamic model, such as added mass, it is possible to compute reasonable approximations. By assessing the velocity error of dynamical models for the case of a relatively simple control surface model with respect to a high-fidelity control surface model acquired from the DSSP tool, we show that a relatively simple model is sufficient.

Chapter 4

Analysis of Conventional Simplifying Model Assumptions

In this chapter, we investigate various sets of conventional simplifying assumptions for torpedo-shaped autonomous underwater vehicles (AUVs) with a specific application to the Trawl-Resistant Self-Mooring AUV (TRSMAUV) in Figure 4.1. We derive several dynamic models for the TRSMAUV employing varying sets of simplifying assumptions. We experimentally assess the efficacy of invoking typical assumptions to simplify the equations of motion. Using data acquired during field trials, we show that the simplified equations of motion adequately represent the motion of the TRSMAUV.

4.1 Introduction

Simplifying assumptions are often invoked to reduce the complexity of the equations of motion of underwater vehicles [4, 23, 26, 57]. We seek to determine if the usual assumptions (e.g. symmetry) that are typically invoked for streamlined tail-controlled AUVs are also suitable for a much less conventional vehicle.

Simplifying assumptions that are often invoked for underwater vehicles include modeling the added mass as a prolate spheroid [4, 23, 26, 34]; omitting the off-diagonal elements of the inertia matrix [4, 54, 57]; neglecting the hydrodynamic coupling between the vehicle's roll, pitch, and yaw [22, 57]; and presuming the vehicle possesses three planes of symmetry.

Figure 4.1: Virginia Tech Trawl-Resistant Self-Mooring AUV

However, it is unclear how well these assumptions apply to vehicles that are non-symmetric and possess non-traditional shapes and propulsion.

We have developed the Trawl-Resistant Self-Mooring AUV, shown in Figure 4.1, that delivers a trawl-resistant bottom mount to the sea floor [14, 15]. The vehicle consists of a top half that contains vehicle propulsion and control surfaces and a bottom half which is the trawl-resistant bottom mount that sits on the sea floor. The AUV operates at 2 m/s during transit and moors at a depth of up to 500 m for up to one year. The TRSMAUV has two servo-actuated flaps that control the vehicle pitch angle, and two propellers in the stern that provide vehicle propulsion while controlling the vehicle yaw angle by differential thrust.

Some simplifying assumptions are questionable when applied to the TRSMAUV due to the large appendages and the sharp edges on the exterior shape. Moreover, the TRSMAUV possesses port-starboard symmetry, but not the top-bottom symmetry that is often assumed for conventional AUVs.

This chapter presents the dynamic models of the TRSMAUV with varying sets of simplifying assumptions. Using experimental data sets acquired with the TRSMAUV at Claytor Lake in Dublin, Virginia, the effectiveness of a dynamical model is assessed by comparing

Table 4.1: Vehicle Parameters

Parameter	Value	Parameter	Value
Dry Weight	360.0 lbs	Max Depth	500.0 m
Length	104.0 in	Operating Speed	2.0 m/s
Width	38.0 in	Range	100.0 nmi
Height	27.4 in		

motion estimated by the model to motion that is measured during the field trial. From the data, we utilize the Nelder-Mead simplex method [38] to identify the model parameters for each dynamic model that minimize the error between model predicted motion and sensor measurements. We show that standard simplifying assumptions are appropriate for the TRSMAUV, and that additional model complexity that arises with fewer modeling assumptions does not necessarily result in better models.

4.2 Equations of Motion

In this section, the dynamic models for the TRSMAUV are presented. The derivation of the these models draws from developments found in Chapter 2 and [4, 23, 51, 52, 69]. The origin of the vehicle is assumed to be located at the center of buoyancy (CB) such that $r_B = [0, 0, 0]^\mathsf{T}$, and the location of the center of gravity (CG) with respect to the CB is denoted as $r_G = [x_G, y_G, z_G]^\mathsf{T}$. We derive three dynamic models with sets of varying simplifying assumptions.

1. **Fully Coupled Model:** The fully coupled model is derived assuming the TRSMAUV possesses port-starboard symmetry.

2. **Pitch and Yaw Models:** The pitch and yaw models are derived assuming the TRSMAUV possesses port-starboard symmetry and motion in pitch and yaw are decoupled, meaning motion in the dive plane does not induce motion in the steering plane and

vice-versa.

3. **Fully Decoupled Model**: The fully decoupled model is derived assuming the TRSMAUV possesses three planes of symmetry and motion in pitch and yaw are decoupled.

4.2.1 Fully Coupled Model

In this section, we derive the fully coupled dynamic model for the TRSMAUV assuming the AUV possesses port-starboard symmetry. Taking the time derivative of the transformation from (2.1) yields

$$\begin{bmatrix} \dot{u} \\ \dot{v} \\ \dot{w} \end{bmatrix} = \begin{bmatrix} \cos(\beta)\cos(\alpha) & V\sin(\beta)\cos(\alpha) & -V\cos(\beta)\sin(\alpha) \\ \sin(\beta) & V\cos(\beta) & 0 \\ \cos(\beta)\sin(\alpha) & -V\sin(\beta)\sin(\alpha) & V\cos(\beta)\cos(\alpha) \end{bmatrix} = \tilde{\mathcal{T}}(\chi) \begin{bmatrix} \dot{V} \\ \dot{\beta} \\ \dot{\alpha} \end{bmatrix}$$

which relates $[\dot{V}, \dot{\beta}, \dot{\alpha}]^\mathsf{T}$ to $[\dot{u}, \dot{v}, \dot{w}]^\mathsf{T}$. The complete expression for $\mathcal{T}(\chi)$ is

$$\mathcal{T}(\chi) = \begin{bmatrix} \tilde{\mathcal{T}}(\chi) & 0_{3\times3} \\ 0_{3\times3} & I_{3\times3} \end{bmatrix} \tag{4.1}$$

which relates $[\dot{V}, \dot{\beta}, \dot{\alpha}, \dot{p}, \dot{q}, \dot{r}]^\mathsf{T}$ to $\dot{\nu}$.

We define a new state vector be $\chi = [V, \beta, \alpha, p, q, r]^\mathsf{T}$, where V, β, α denote the magnitude of the vehicle velocity, side-slip angle, and angle of attack, respectively. Using (4.1) and

modifying (2.5), the equations of motion for the TRSMAUV are expressed

$$M\mathcal{T}(\chi)\dot{\chi} = \mathcal{R}(\chi) + \mathcal{T}(\chi)D(\chi) + \mathcal{G}(R_1(\eta_2)) + \mathcal{T}(\chi)U_{CS}(\delta) + U_{Prop}(\delta) \tag{4.2}$$

where $\mathcal{R}(\chi)$ represents the Coriolis forces and moments. Equation (2.2) models the vehicle kinematics and (4.2) models the dynamics. Each term in (4.2) will be derived in the sequel.

For a vehicle with port-starboard symmetry, $y_G = 0$. The simplified expression for the rigid-body inertia matrix is

$$M_{RB} = \begin{bmatrix} m & 0 & 0 & 0 & mz_G & 0 \\ 0 & m & 0 & -mz_G & 0 & mx_G \\ 0 & 0 & m & 0 & -mx_G & 0 \\ 0 & -mz_G & 0 & J_{xx} & 0 & -J_{zx} \\ mz_G & 0 & -mx_G & 0 & J_{yy} & 0 \\ 0 & mx_G & 0 & -J_{zx} & 0 & J_{zz} \end{bmatrix}$$

where vehicle mass is denoted as m, and J is the moment of inertia corresponding to its subscript. The inertial terms due to added mass for a vehicle with port-starboard symmetry [23, Section 2.5] are

$$M_A = \begin{bmatrix} -X_{\dot{u}} & 0 & -X_{\dot{w}} & 0 & -X_{\dot{q}} & 0 \\ 0 & -Y_{\dot{v}} & 0 & -Y_{\dot{p}} & 0 & -Y_{\dot{r}} \\ -X_{\dot{w}} & 0 & -Z_{\dot{w}} & 0 & -Z_{\dot{q}} & 0 \\ 0 & -Y_{\dot{p}} & 0 & -K_{\dot{p}} & 0 & -K_{\dot{r}} \\ -X_{\dot{q}} & 0 & -Z_{\dot{q}} & 0 & -M_{\dot{q}} & 0 \\ 0 & -Y_{\dot{r}} & 0 & -K_{\dot{r}} & 0 & -N_{\dot{r}} \end{bmatrix}.$$

Together, the inertia matrix is given by

$$
\begin{aligned}
M &= M_{RB} + M_A \\
&= \begin{bmatrix}
m - X_{\dot{u}} & 0 & -X_{\dot{w}} & 0 & mz_G - X_{\dot{q}} & 0 \\
0 & m - Y_{\dot{v}} & 0 & -mz_G - Y_{\dot{p}} & 0 & mx_G - Y_{\dot{r}} \\
-X_{\dot{w}} & 0 & m - Z_{\dot{w}} & 0 & -mx_G - Z_{\dot{q}} & 0 \\
0 & -mz_G - Y_{\dot{p}} & 0 & J_{xx} - K_{\dot{p}} & 0 & -J_{zx} - K_{\dot{r}} \\
mz_G - X_{\dot{q}} & 0 & -mx_G - Z_{\dot{q}} & 0 & J_{yy} - M_{\dot{q}} & 0 \\
0 & mx_G - Y_{\dot{r}} & 0 & -J_{zx} - K_{\dot{r}} & 0 & J_{zz} - N_{\dot{r}}
\end{bmatrix}
\end{aligned}
\tag{4.3}
$$

which can be partitioned into

$$
M = \begin{bmatrix} M_{11} & M_{21}^{\mathsf{T}} \\ M_{21} & M_{22} \end{bmatrix} \tag{4.4}
$$

where M_{11}, M_{21}, $M_{22} \in \mathbb{R}^{3\times 3}$.

Following the procedure in [4], the expression for $\mathcal{R}(\nu)$ is given by

$$
\mathcal{R}(\nu) = \begin{bmatrix} \left(M_{11}\nu_1 + M_{21}^{\mathsf{T}}\nu_2\right) \times \nu_2 \\ \left(M_{21}\nu_1 + M_{22}\nu_2\right) \times \nu_2 + \left(M_{11}\nu_1 + M_{21}^{\mathsf{T}}\nu_2\right) \times \nu_1 \end{bmatrix}. \tag{4.5}
$$

By carrying out the matrix multiplication, performing the cross products, and substituting

in the transformation from (2.1), the full expression for $\mathcal{R}(\chi)$ can be computed as

$$\mathcal{R}(\chi) = \begin{bmatrix} -pr(mz_G + Y_{\dot{p}}) + V\left(m_y r \sin\beta - m_z q \cos\beta \sin\alpha + q X_{\dot{w}} \cos\beta \cos\alpha\right) \dots \\ \quad + q^2(mx_G + Z_{\dot{q}}) + r^2(mx_G - Y_{\dot{r}}) \\ -qr(mz_G - X_{\dot{q}}) + V\left([m_z p + r X_{\dot{w}}] \cos\beta \sin\alpha - [p X_{\dot{w}} + m_x r] \cos\beta \cos\alpha\right) \dots \\ \quad - pq(mx_G + Z_{\dot{q}}) \\ -pr(mx_G - Y_{\dot{r}}) + V\left(m_x q \cos\beta \cos\alpha - m_y p \sin\beta - q X_{\dot{w}} \cos\beta \sin\alpha\right) \dots \\ \quad + q^2(mz_G - X_{\dot{q}}) + p^2(mz_G + Y_{\dot{p}}) \\ qr(\tilde{J}_{yy} - \tilde{J}_{zz}) + pq(J_{zx} + K_{\dot{r}}) + V^2\left([m_y - m_z] \cos\beta \sin\beta \sin\alpha\right) \dots \\ \quad + V\left(r\left[mz_G - X_{\dot{q}}\right] \cos\beta \cos\alpha - [p(mz_G + Y_{\dot{p}}) + r(Y_{\dot{r}} + Z_{\dot{q}})] \cos\beta \sin\alpha\right) \dots \\ \quad + Vq\left(Y_{\dot{r}} + Z_{\dot{q}}\right) \sin\beta + V^2 X_{\dot{w}} \cos\beta \sin\beta \cos\alpha \\ pr(\tilde{J}_{zz} - \tilde{J}_{xx}) + (r^2 - p^2)(J_{zx} + K_{\dot{r}}) + V^2\left([m_z - m_x] \cos^2\beta \cos\alpha \sin\alpha\right) \dots \\ \quad + V^2 X_{\dot{w}} \cos^2\beta \left(\sin^2\alpha - \cos^2\alpha\right) - Vq(mx_G + Z_{\dot{q}}) \cos\beta \cos\alpha \dots \\ \quad - Vq(mz_G - X_{\dot{q}}) \cos\beta \sin\alpha + V(p\left[mx_G - Y_{\dot{r}}\right] + r\left[mz_G + Y_{\dot{p}}\right]) \sin\beta \\ pq(\tilde{J}_{xx} - \tilde{J}_{yy}) - qr(J_{zx} + K_{\dot{r}}) + V^2\left([m_x - m_y] \cos\beta \sin\beta \cos\alpha\right) \dots \\ \quad - V^2 X_{\dot{w}} \cos\beta \sin\beta \sin\alpha + V\left([p(X_{\dot{q}} + Y_{\dot{p}}) - r(mx_G - Y_{\dot{r}})] \cos\beta \cos\alpha\right) \dots \\ \quad + Vp(mx_G + Z_{\dot{q}}) \cos\beta \sin\alpha - Vq(X_{\dot{q}} + Y_{\dot{p}}) \sin\beta \end{bmatrix} \tag{4.6}$$

where

$$m_x = m - X_{\dot{u}}, \qquad m_y = m - Y_{\dot{v}}, \qquad m_z = m - Z_{\dot{w}},$$
$$\tilde{J}_{xx} = J_{xx} - K_{\dot{p}}, \qquad \tilde{J}_{yy} = J_{yy} - M_{\dot{q}}, \qquad \tilde{J}_{zz} = J_{zz} - N_{\dot{r}}.$$

We follow a similar treatment as in [51] and model the damping forces and moments $D(\chi)$ due to vehicle drag, lift, and side-slip. We assume that the vehicle is not operating in a stalled condition. Due to the lack of three planes of symmetry, the quadratic approximation

for drag as a function of angle of attack is different than the approximation for drag as a function of side-slip. The damping forces acting on the vehicle are expressed

$$F_D(V,\alpha,\beta) = \frac{1}{2}\rho V^2 A_b \left[C_{D_{b2\alpha}}\alpha^2 + C_{D_{b0\alpha}} + C_{D_{b2\beta}}\beta^2 + C_{D_{b0\beta}}\right] \tag{4.7a}$$

$$F_L(V,\alpha) = \frac{1}{2}\rho V^2 A_b C_{L_\alpha}\alpha \tag{4.7b}$$

$$F_S(V,\beta) = \frac{1}{2}\rho V^2 A_b C_{L_\beta}\beta \tag{4.7c}$$

where A_b is the reference surface area of the body, ρ is the density of water, and $C_{L_{(\cdot)}}$, $C_{D_{(\cdot)}}$ are the respective lift and drag coefficients. The drag coefficients as a function of angle of attack and side-slip are not equal in general, meaning

$$C_{D_{b2\alpha}} \neq C_{D_{b2\beta}}$$

$$C_{D_{b0\alpha}} \neq C_{D_{b0\beta}}.$$

As in [5], [51], and [64], the damping moments are expressed

$$L_p(V,\beta,p) = \frac{1}{2}\rho V^2 A_b L_v \left[C_{l_\beta}\beta + C_{l_p}p\right] \tag{4.8a}$$

$$M_q(V,\alpha,q) = \frac{1}{2}\rho V^2 A_b L_v \left[C_{m_\alpha}\alpha + C_{m_q}q\right] \tag{4.8b}$$

$$N_r(V,\beta,r) = \frac{1}{2}\rho V^2 A_b L_v \left[C_{n_\beta}\beta + C_{n_r}r\right] \tag{4.8c}$$

where L_v is the reference length of the vehicle. The drag coefficients $C_{D_{b2\alpha}}$, $C_{D_{b0\alpha}}$, $C_{D_{b2\beta}}$, and $C_{D_{b0\beta}}$ are negative because drag forces counteract vehicle motion. The lift coefficient C_{L_α} is negative because a positive angle of attack produces a negative lift force (up). The damping moment coefficients C_{m_α} and C_{n_β} are referred to as the pitch and yaw static stability coefficients, respectively [5]. By definition of α and β (see Figure 2.1), the vehicle's body generates a negative restoring moment about the pitch axis for $\alpha > 0$, and a positive restoring

moment about the yaw axis for $\beta > 0$. This implies that $C_{m_\alpha} < 0$ and $C_{n_\beta} > 0$. The damping moment coefficient C_{l_β} is the roll static stability coefficient and is associated with an AUV's CG and CB separation. For static stability in roll with a zero roll angle, the vehicle's center of gravity r_G must be below the vehicle's center of buoyancy r_B. A negative roll coefficient $C_{l_\beta} < 0$ will result in rolling moments that roll the AUV away from the direction of the side-slip angle which will drive the side-slip angle to zero [5]. The coefficients C_{l_p}, C_{m_q}, and C_{n_r} are the roll, pitch, and yaw damping coefficients, respectively [5]. These damping coefficients are usually negative $C_{l_p} < 0$, $C_{m_q} < 0$, and $C_{n_r} < 0$, meaning that a moment is produced that opposes the direction of motion [5]. Combining (4.7) and (4.8), we model the damping forces and moments as

$$D(\chi) = \begin{bmatrix} F_D(V, \alpha, \beta) \\ F_S(V, \beta) \\ F_L(V, \alpha) \\ L_p(V, \beta, p) \\ M_q(V, \alpha, q) \\ N_r(V, \beta, r) \end{bmatrix}. \tag{4.9}$$

Control inputs for the TRSMAUV are represented by $\delta = [\delta_e, n_p^2, n_s^2]$, where δ_e is the elevator flap deflection angle, n_p is the rotation rate of the port motor, and n_s is the rotation rate of the starboard motor. The flap drag and lift forces are approximated as

$$F_{D\delta_e}(V, \delta_e) = \frac{1}{2}\rho V^2 A_f \left[C_{D\delta_e 0} + C_{D\delta_e}\delta_e^2\right] \tag{4.10a}$$

$$F_{L\delta_e}(V, \delta_e) = \frac{1}{2}\rho V^2 A_f C_{L\delta_e}\delta_e \tag{4.10b}$$

where $C_{D\delta_e}$ is the flap drag coefficient, $C_{L\delta_e}$ is the flap lift coefficient, and A_f is the reference

surface area of the flap. It is assumed that drag forces from the flaps at zero deflection are negligible, so $C_{D\delta_e 0} = 0$. The pitch moment generated by a elevator flap deflection is expressed as

$$M_{q\delta_e}(V, \delta_e) = \frac{1}{2}\rho V^2 A_f C_{m\delta_e}\delta_e \tag{4.11}$$

where $C_{m\delta_e}$ is the flap pitch moment control coefficient. The flap drag coefficient $C_{D\delta_e}$ is negative because drag forces counteract vehicle motion. The flap lift coefficient $C_{L\delta_e}$ is also negative because a positive elevator flap deflection produces a negative lift force (up). The flap moment coefficient $C_{m\delta_e}$ is referred to as a primary control coefficient [5]. The control coefficient can be thought of as a gain; the larger the control coefficient, the larger the magnitude of the moment produced for an elevator deflection [5]. For the TRSMAUV, the moment control coefficient is negative $C_{m\delta_e} < 0$ as a positive deflection angle produces a negative pitch moment. Using (4.10) and (4.11), we express the forces and moments due to the elevator flap as

$$U_{CS}(\delta) = \begin{bmatrix} F_{D\delta_e}(V, \delta_e) \\ 0 \\ F_{L\delta_e}(V, \delta_e) \\ 0 \\ M_{q\delta_e}(V, \delta_e) \\ 0 \end{bmatrix}. \tag{4.12}$$

The starboard and port thrust forces are modeled as

$$F_{ts} = C_{ts} n_s |n_s| \tag{4.13a}$$

$$F_{tp} = C_{tp} n_p |n_p| \tag{4.13b}$$

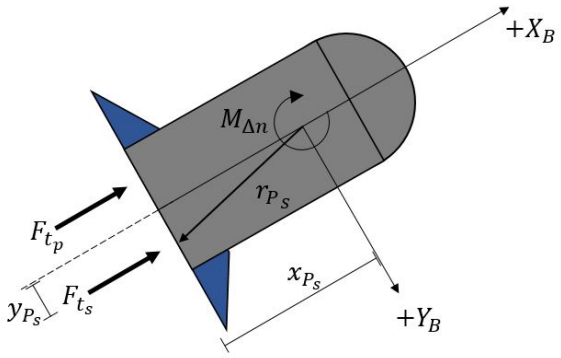

Figure 4.2: Illustration for the derivation of $M_{\Delta n}$

where C_{ts} and C_{tp} are starboard and port thrust coefficients, respectively [69]. The total vehicle thrust force is simply the summation $F_t = F_{ts} + F_{tp}$. The roll moment generated by the propellers is the summation of the two propeller torques $Q = Q_s + Q_p$ where Q_s and Q_p are the torques of the starboard and port propellers, respectively. The TRSMAUV has counter-rotating propellers to minimize the moment due to propeller torque. A yaw moment is generated by the propellers if they are rotating at different rates. The difference in thrust is used to steer the vehicle. From Figure 4.2, we can derive the yaw moment due to the difference in thrust. Let $r_{P_p} = [-x_P, -y_P, 0]^\mathsf{T}$ and $r_{P_s} = [-x_P, y_P, 0]^\mathsf{T}$ denote the positions of the port and starboard propellers, respectively, relative to the origin of the vehicle. The moment due to the starboard propeller N_{rn_s} is

$$\begin{aligned} N_{rn_s} &= \begin{bmatrix} -x_P \\ y_P \\ 0 \end{bmatrix} \times \begin{bmatrix} F_{ts} \\ 0 \\ 0 \end{bmatrix} \\ &= -y_P C_{ts} n_s^2. \end{aligned}$$

Similarly, the moment due to the port propeller N_{rn_p} is

$$\begin{aligned} N_{rn_p} &= \begin{bmatrix} -x_P \\ -y_P \\ 0 \end{bmatrix} \times \begin{bmatrix} F_{tp} \\ 0 \\ 0 \end{bmatrix} \\ &= y_P C_{tp} n_p^2. \end{aligned}$$

Then the total yaw moment due to the difference in thrust is

$$\begin{aligned} N_{r\Delta n} &= N_{rn_s} + N_{rn_p} \\ &= y_P(C_{tp} n_p^2 - C_{ts} n_s^2). \end{aligned} \tag{4.14}$$

Using (4.13), Q, and (4.14), the forces and moments due to the TRSMAUV propellers are

$$U_{Prop}(\delta) = \begin{bmatrix} F_t \\ 0 \\ 0 \\ Q \\ 0 \\ y_P(C_{tp} n_p^2 - C_{ts} n_s^2) \end{bmatrix}. \tag{4.15}$$

Expressions for the hydrostatic forces and moments $\mathcal{G}(R_1(\eta_2))$ can be readily obtained from (2.6) by taking $r_B = [0, 0, 0]^\mathsf{T}$.

We proceed by augmenting the state vector χ with the Euler angles

$$x = [V, \beta, \alpha, p, q, r, \phi, \theta, \psi]^\mathsf{T}$$

to combine the kinematics and dynamics into one nonlinear system of equations

$$\mathrm{MT}(x)\dot{x} = \mathrm{R}(x) + \mathrm{T}(x)D(x) + \mathrm{G}(x) + \mathrm{T}(x)\mathrm{U}_{\mathrm{CS}}(\delta) + \mathrm{U}_{\mathrm{Prop}}(\delta) \tag{4.16}$$

where

$$\mathrm{M} = \begin{bmatrix} M & 0_{3\times3} \\ 0_{3\times3} & I_{3\times3} \end{bmatrix}, \qquad \mathrm{T}(x) = \begin{bmatrix} \mathcal{T}(\chi) & 0_{3\times3} \\ 0_{3\times3} & I_{3\times3} \end{bmatrix}, \qquad \mathrm{R}(x) = \begin{bmatrix} \mathcal{R}(\chi) \\ \mathrm{R}_1(\eta_2)\nu_2 \end{bmatrix},$$
$$\mathrm{G}(x) = \begin{bmatrix} \mathcal{G}(R_1(\eta_2)) \\ 0_{3\times1} \end{bmatrix}, \qquad \mathrm{U}_{\mathrm{CS}}(\delta) = \begin{bmatrix} U_{CS}(\delta) \\ 0_{3\times1} \end{bmatrix}, \qquad \mathrm{U}_{\mathrm{Prop}}(\delta) = \begin{bmatrix} U_{Prop}(\delta) \\ 0_{3\times1} \end{bmatrix}.$$

Linearizing (4.16) about the steady state conditions

$$x = [V_0, 0, 0, 0, 0, 0, 0, 0, 0]^{\mathsf{T}}, \qquad \delta = [0, n_0^2, n_0^2]^{\mathsf{T}}, \qquad g = b,$$

yields the linear system $\dot{x} = Ax + B\delta$ where g is gravitational force, b is the buoyancy force, V_0 is the nominal speed, n_0 is the nominal propeller rotation rate, and

$$A = \begin{bmatrix} a_{11} & a_{12} & a_{13} & a_{14} & a_{15} & a_{16} & a_{17} & a_{18} & 0 \\ a_{21} & a_{22} & a_{23} & a_{24} & a_{25} & a_{26} & a_{27} & a_{28} & 0 \\ a_{31} & a_{32} & a_{33} & a_{34} & a_{35} & a_{36} & a_{37} & a_{38} & 0 \\ a_{41} & a_{42} & a_{43} & a_{44} & a_{45} & a_{46} & a_{47} & a_{48} & 0 \\ a_{51} & a_{52} & a_{53} & a_{54} & a_{55} & a_{56} & a_{57} & a_{58} & 0 \\ a_{61} & a_{62} & a_{63} & a_{64} & a_{65} & a_{66} & a_{67} & a_{68} & 0 \\ 0 & 0 & 0 & 1 & 0 & 0 & 0 & 0 & 0 \\ 0 & 0 & 0 & 0 & 1 & 0 & 0 & 0 & 0 \\ 0 & 0 & 0 & 0 & 0 & 1 & 0 & 0 & 0 \end{bmatrix}, \qquad B = \begin{bmatrix} b_{11} & b_{12} & b_{13} \\ b_{21} & b_{22} & b_{23} \\ b_{31} & b_{32} & b_{33} \\ b_{41} & b_{42} & b_{43} \\ b_{51} & b_{52} & b_{53} \\ b_{61} & b_{62} & b_{63} \\ 0 & 0 & 0 \\ 0 & 0 & 0 \\ 0 & 0 & 0 \end{bmatrix}.$$

The coefficients in the A and B matrices are expressions comprising of the physical parameters that make up (4.3)-(4.15). Since the expressions do not provide additional insight into the system identification, these expressions have been omitted due to their large size. See [51, 54] for examples of these expressions.

4.2.2 Pitch and Yaw Models

To develop the pitch-axis model, the motion of the vehicle is restricted to the dive plane by setting $v = p = r = \phi = \psi = 0$. This restriction allows for the truncation of the state vector to $x_\theta = [V, \alpha, q, \theta]^\mathsf{T}$, the control input to $\delta = \delta_e$, and reduces the terms in (4.16) to

$$\mathrm{M} = \begin{bmatrix} m - X_{\dot{u}} & -X_{\dot{w}} & mz_G - X_{\dot{q}} & 0 \\ -X_{\dot{w}} & m - Z_{\dot{w}} & -mx_G - Z_{\dot{q}} & 0 \\ mz_G - X_{\dot{q}} & -mx_G - Z_{\dot{q}} & J_{yy} - M_{\dot{q}} & 0 \\ 0 & 0 & 0 & 1 \end{bmatrix}, \quad \mathrm{T}(x_\theta) = \begin{bmatrix} \cos\alpha & -V\sin(\alpha) & 0 & 0 \\ \sin(\alpha) & V\cos(\alpha) & 0 & 0 \\ 0 & 0 & 1 & 0 \\ 0 & 0 & 0 & 1 \end{bmatrix},$$

$$\mathrm{R}(x_\theta) = \begin{bmatrix} \mathcal{R}_1(x_\theta) \\ \mathcal{R}_3(x_\theta) \\ \mathcal{R}_5(x_\theta) \\ q \end{bmatrix}, \qquad \mathrm{G}(x_\theta) = \begin{bmatrix} \mathcal{G}_1(R_1(\eta_2)) \\ \mathcal{G}_3(R_1(\eta_2)) \\ \mathcal{G}_5(R_1(\eta_2)) \\ 0 \end{bmatrix},$$

$$\mathrm{U_{CS}}(\delta_e) = \begin{bmatrix} U_{CS_1}(\delta_e) \\ U_{CS_3}(\delta_e) \\ U_{CS_5}(\delta_e) \\ 0 \end{bmatrix}, \qquad \mathrm{U_{Prop}}(\delta_e) = \begin{bmatrix} U_{Prop_1}(\delta_e) \\ U_{Prop_3}(\delta_e) \\ U_{Prop_5}(\delta_e) \\ 0 \end{bmatrix},$$

where the numeric subscripts in the terms $\mathcal{R}_{(\cdot)}$, $\mathcal{G}_{(\cdot)}$, $U_{CS_{(\cdot)}}$, and $U_{Prop_{(\cdot)}}$ denote the i^{th} expression of the vector. Essentially, we truncate the states pertaining to the steering plane and keep the dive plane states. To obtain the system to be identified, (4.16) is linearized about the steady-state conditions

$$x_\theta = [V_0, 0, 0, 0]^\mathsf{T}, \qquad \delta_e = 0, \qquad g = b,$$

yielding the linear system

$$\dot{x}_\theta = A_\theta x_\theta + B_\theta \delta_e \tag{4.17}$$

where

$$A_\theta = \begin{bmatrix} a_{11} & a_{12} & a_{13} & a_{14} \\ a_{21} & a_{22} & a_{23} & a_{24} \\ a_{31} & a_{32} & a_{33} & a_{34} \\ 0 & 0 & 1 & 0 \end{bmatrix}, \qquad B_\theta = \begin{bmatrix} b_{11} \\ b_{21} \\ b_{31} \\ 0 \end{bmatrix}.$$

Derivation of a yaw-axis model proceeds in manner that parallels the derivation of the pitch-axis model. Although in the case of the yaw-axis model we assume that $w = p = q = \phi = \theta = 0$. The state vector is $x_\psi = [V, \beta, r, \psi]^\mathsf{T}$, and the control inputs are $\delta_\psi = [n_p^2, n_s^2]^\mathsf{T}$. The terms in (4.16) reduce to

$$\mathrm{M} = \begin{bmatrix} m - X_{\dot{u}} & 0 & 0 & 0 \\ 0 & m - Y_{\dot{v}} & mx_G - Y_{\dot{r}} & 0 \\ 0 & mx_G - Y_{\dot{r}} & J_{zz} - N_{\dot{r}} & 0 \\ 0 & 0 & 0 & 1 \end{bmatrix}, \quad \mathrm{T}(x_\psi) = \begin{bmatrix} \cos(\beta) & -V\sin(\beta) & 0 & 0 \\ \sin(\beta) & V\cos(\beta) & 0 & 0 \\ 0 & 0 & 1 & 0 \\ 0 & 0 & 0 & 1 \end{bmatrix},$$

$$\mathrm{R}(x_\psi) = \begin{bmatrix} \mathcal{R}_1(x_\psi) \\ \mathcal{R}_2(x_\psi) \\ \mathcal{R}_6(x_\psi) \\ r \end{bmatrix}, \qquad \mathrm{G}(x_\psi) = \begin{bmatrix} \mathcal{G}_1(R_1(\eta_2)) \\ \mathcal{G}_2(R_1(\eta_2)) \\ \mathcal{G}_6(R_1(\eta_2)) \\ 0 \end{bmatrix},$$

$$\mathrm{U}_{\mathrm{CS}}(\delta_\psi) = \begin{bmatrix} U_{CS_1}(\delta_\psi) \\ U_{CS_2}(\delta_\psi) \\ U_{CS_6}(\delta_\psi) \\ 0 \end{bmatrix}, \qquad \mathrm{U}_{\mathrm{Prop}}(\delta_\psi) = \begin{bmatrix} U_{Prop_1}(\delta_\psi) \\ U_{Prop_2}(\delta_\psi) \\ U_{Prop_6}(\delta_\psi) \\ 0 \end{bmatrix},$$

Linearizing (4.16) about the steady-state conditions

$$x_\psi = [V_0, 0, 0, 0]^\mathsf{T}, \qquad \delta_\psi = [n_0^2, n_0^2]^\mathsf{T},$$

yields the yaw-axis model

$$\dot{x}_\psi = A_\psi x_\psi + B_\psi \delta_\psi \tag{4.18}$$

where

$$A_\psi = \begin{bmatrix} a_{11} & a_{12} & a_{13} & 0 \\ a_{21} & a_{22} & a_{23} & 0 \\ a_{31} & a_{32} & a_{33} & 0 \\ 0 & 0 & 1 & 0 \end{bmatrix}, \qquad B_\psi = \begin{bmatrix} b_{11} & b_{12} \\ b_{21} & b_{22} \\ b_{31} & b_{32} \\ 0 & 0 \end{bmatrix}.$$

To assess the utility of the pitch-axis model (4.17) and the yaw-axis model (4.18), their ability to accurately predict the motion of the AUV given knowledge of control inputs is compared to that of the model derived in [51], wherein simplifying assumptions are invoked, on the basis of vehicle symmetry, to reduce model complexity.

4.2.3 Fully Decoupled Model

A fully decoupled model assumes three planes of symmetry as in [23, 51, 52, 57]. In [51] the author derives a 6 DOF model, and then restricts motion, to form a pitch-axis model. The derivation of the previous models in this work were based on these developments. The vehicle in [51] was assumed to possess three planes of symmetry. With this symmetry, the off-diagonal terms of the inertia matrix become negligible such that for the pitch and yaw models M simplifies to

$$\mathrm{M}_\theta = \begin{bmatrix} m - X_{\dot{u}} & 0 & 0 & 0 \\ 0 & m - Z_{\dot{w}} & 0 & 0 \\ 0 & 0 & J_{yy} - M_{\dot{q}} & 0 \\ 0 & 0 & 0 & 1 \end{bmatrix}, \quad \mathrm{M}_\psi = \begin{bmatrix} m - X_{\dot{u}} & 0 & 0 & 0 \\ 0 & m - Y_{\dot{v}} & 0 & 0 \\ 0 & 0 & J_{zz} - N_{\dot{r}} & 0 \\ 0 & 0 & 0 & 1 \end{bmatrix}$$

Additionally the AUV is assumed to be neutrally buoyant such that the angle of attack and pitch angle are asssumed to be zero. For the yaw-axis model, the side-slip angle is

assumed to be zero. The transformation matrices become

$$\mathrm{T}_\theta(x_\theta) = \mathrm{T}_\psi(x_\psi) = \begin{bmatrix} 1 & 0 & 0 & 0 \\ 0 & V & 0 & 0 \\ 0 & 0 & 1 & 0 \\ 0 & 0 & 0 & 1 \end{bmatrix}$$

All other expressions are the same as the previous pitch-axis and yaw-axis models from Section 4.2.2. Linearizing (4.16) about the same steady state conditions as was done previously, the pitch-axis and yaw-axis models are

$$\dot{x}_\theta = A_\theta x_\theta + B_\theta \delta_e$$
$$\dot{x}_\psi = A_\psi x_\psi + B_\psi \delta_\psi$$

where

$$A_\theta = \begin{bmatrix} a_{11} & 0 & 0 & 0 \\ 0 & a_{22} & a_{23} & 0 \\ 0 & a_{32} & a_{33} & a_{34} \\ 0 & 0 & 1 & 0 \end{bmatrix}, \; B_\theta = \begin{bmatrix} 0 \\ b_1 \\ b_2 \\ 0 \end{bmatrix}, \; A_\psi = \begin{bmatrix} a_{11} & 0 & 0 & 0 \\ 0 & a_{22} & a_{23} & 0 \\ 0 & a_{32} & a_{33} & 0 \\ 0 & 0 & 1 & 0 \end{bmatrix}, \; B_\psi = \begin{bmatrix} 0 & 0 \\ 0 & 0 \\ b_{31} & b_{32} \\ 0 & 0 \end{bmatrix}.$$

The magnitude of the velocity V decouples from all the other state variables, allowing for the truncation of the state space to

$$A_\theta = \begin{bmatrix} a_{22} & a_{23} & 0 \\ a_{32} & a_{33} & a_{34} \\ 0 & 1 & 0 \end{bmatrix}, \; B_\theta = \begin{bmatrix} b_1 \\ b_2 \\ 0 \end{bmatrix}, \; A_\psi = \begin{bmatrix} a_{22} & a_{23} & 0 \\ a_{32} & a_{33} & 0 \\ 0 & 1 & 0 \end{bmatrix}, \; B_\psi = \begin{bmatrix} 0 & 0 \\ b_{31} & b_{32} \\ 0 & 0 \end{bmatrix}.$$

Similar decoupled models can be found in [11, 23, 57, 62, 66].

4.3 Experimental Results

4.3.1 Experimental Environment

The TRSMAUV shown in Figure 4.1 was used to acquire experimental data. In order to satisfy mission requirements, the TRSMAUV has a non-traditional shape with sharp edges to deflect trawl nets and weighs approximately 360 pounds in air. The AUV has two independently actuated horizontal flaps in the stern to control pitch-axis motion, and it has two propellers at the stern to produce thrust and control yaw-axis motion. The vehicle is equipped with an attitude and heading reference system (AHRS) to measure vehicle body rates and Euler angles; a pressure sensor to measure depth; two motor encoders to measure rotational speed of the propellers; a GPS receiver to measure the location of the vehicle; and a Iridium satellite communication receiver, and a 900MHz spread spectrum radio for vehicle communication.

Various experiments were performed at Claytor Lake in Pulaski County, Virginia. The experiments included fully submerged step changes in depth and yaw to excite the pitch and yaw dynamics of the TRSMAUV. These maneuvers are also known as the classical zig-zag maneuver in the dive and steering planes. For all experiments, the TRSMAUV operated at a propeller speed of 1300 RPM that corresponds to a surge velocity of approximately 1.25 meters/sec.

4.3.2 System Identification

From the data acquired at Claytor Lake, the parameters from the models presented in Section 4.2 can be identified. Experiments with step changes in depth are used to identify

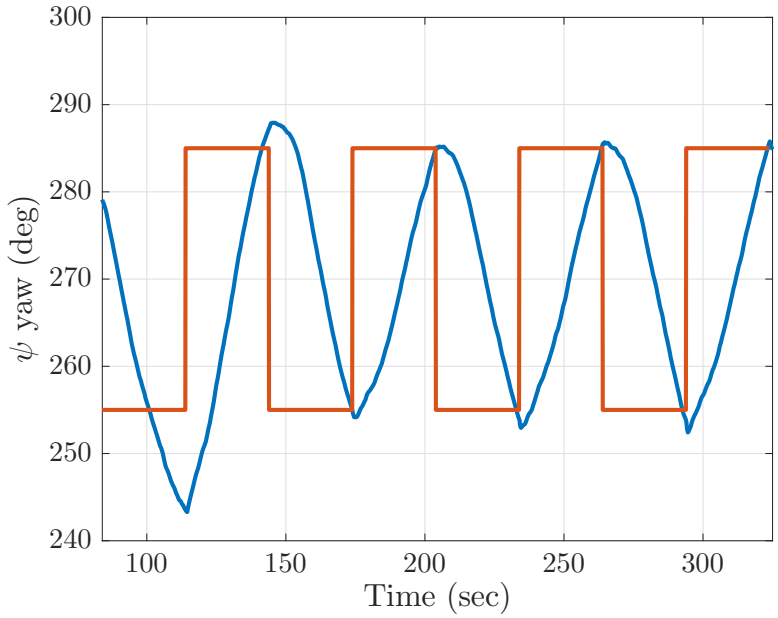

Figure 4.3: Step changes in yaw. Yaw angle is shown in blue and commanded yaw is shown in orange.

parameters in pitch models while experiments with step changes in yaw are used to identify parameters in yaw models. At each time step, the TRSMAUV uses an AHRS to measure most of the states in the state vector specifically pitch angle, yaw angle, pitch rate, and yaw rate. To identify the parameters in the dynamic models, we employ the same identification technique from [54] to match the input-output behavior of the TRSMAUV. We utilize the Nelder-Mead simplex method to identify the model parameters for each dynamic model that minimize the following cost functions for decoupled models

$$J_\theta = \sum_{k=1}^{n} \|\theta(k) - \hat{\theta}(k)\|^2 + \|q(k) - \hat{q}(k)\|^2$$

$$J_\psi = \sum_{k=1}^{n} \|\psi(k) - \hat{\psi}(k)\|^2 + \|r(k) - \hat{r}(k)\|^2$$

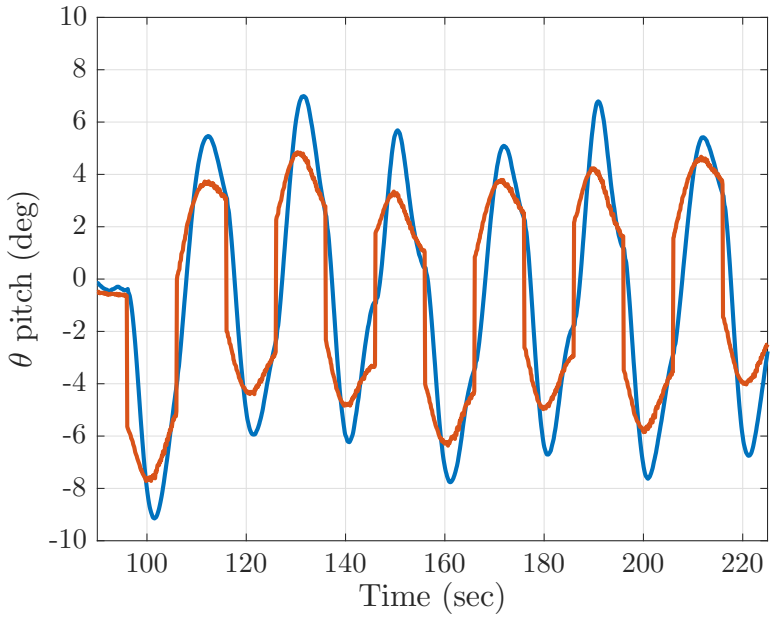

Figure 4.4: Pitch angle is shown in blue and commanded pitch is shown in orange.

and the following cost function for the coupled model

$$J = J_\theta + J_\psi$$

where n is the number of data samples, q is the vehicle pitch rate, r is the vehicle yaw rate, and state estimates are denoted with a hat. Step changes in yaw are shown in Figure 4.3 and step changes in pitch as a result of step changes in depth command are shown in Figure 4.4.

Using the data from the step changes in depth and yaw, the parameters for the dynamic models from Section 4.2 are identified, and the cost for each model is presented in Table 4.2. For the fully coupled model, the identification utilized experimental data with step changes in depth and yaw. For the other models, the identification utilized experimental data with either step changes in depth or step changes in yaw.

Fully Coupled Model

The parameters identified using the fully coupled model are

$$A = \begin{bmatrix} -0.28 & 0.32 & -0.00 & 0.21 & 0.58 & -0.16 & 0.00 & -0.63 & 0 \\ -0.08 & -1.10 & 0.10 & -0.01 & 0.20 & 0.02 & -0.06 & 0.65 & 0 \\ -0.03 & 0.23 & -0.21 & 0.00 & 0.01 & -0.01 & 0.48 & -0.08 & 0 \\ -0.00 & -2.45 & 0.02 & -4.31 & 0.01 & -0.01 & -0.02 & -2.06 & 0 \\ -0.01 & 0.00 & 0.01 & 0.11 & -0.07 & -0.03 & -0.01 & -0.01 & 0 \\ -0.00 & 0.00 & 0.03 & 0.05 & 0.03 & -2.66 & 0.08 & 0.04 & 0 \\ 0 & 0 & 0 & 1.00 & 0 & 0 & 0 & 0 & 0 \\ 0 & 0 & 0 & 0 & 1.00 & 0 & 0 & 0 & 0 \\ 0 & 0 & 0 & 0 & 0 & 1.00 & 0 & 0 & 0 \end{bmatrix},$$

$$B = \begin{bmatrix} -0.0001 & -0.0000 & 0.0003 \\ 0.0003 & -0.0001 & 0.0000 \\ -0.0001 & -0.0001 & 0.0001 \\ 0.0001 & -0.0001 & 0.0002 \\ -0.0216 & -0.0000 & -0.0000 \\ -0.0035 & 0.0001 & 0.0001 \\ 0 & 0 & 0 \\ 0 & 0 & 0 \\ 0 & 0 & 0 \end{bmatrix}.$$

Pitch and Yaw Models

The parameters identified using the pitch-axis and yaw-axis models are

$$A_\theta = \begin{bmatrix} -1.28 & -1.66 & -1.36 & 1.78 \\ 0.96 & 1.22 & -0.05 & -0.14 \\ -0.30 & -0.61 & -3.90 & -7.16 \\ 0 & 0 & 1.00 & 0 \end{bmatrix}, \qquad B_\theta = \begin{bmatrix} 0.06 \\ 0.32 \\ 0.49 \\ 0 \end{bmatrix}.$$

$$A_\psi = \begin{bmatrix} -0.30 & -0.00 & -0.03 & 0 \\ -0.05 & -0.25 & -0.10 & 0 \\ -0.00 & 0.03 & -0.42 & 0 \\ 0 & 0 & 1.00 & 0 \end{bmatrix}, \qquad B_\psi = \begin{bmatrix} -0.00001 & 0.00001 \\ -0.00000 & 0.00000 \\ 0.00003 & 0.00003 \\ 0 & 0 \end{bmatrix}.$$

Fully Decoupled Model

The parameters identified using the fully decoupled pitch and yaw models are

$$A_\theta = \begin{bmatrix} -1.45 & 2.07 & 0 \\ 1.75 & -2.55 & -0.26 \\ 0 & 1.00 & 0 \end{bmatrix}, \qquad B_\theta = \begin{bmatrix} -0.08 \\ 0.05 \\ 0 \end{bmatrix},$$

$$A_\psi = \begin{bmatrix} -0.14 & 5.40 & 0 \\ 0.06 & -6.68 & 0 \\ 0 & 1.00 & 0 \end{bmatrix}, \qquad B_\psi = \begin{bmatrix} 0 & 0 \\ 0.0003 & 0.0004 \\ 0 & 0 \end{bmatrix}.$$

4.3.3 Verification

For verification of the identified models, additional step changes in depth and yaw experiments were performed. The additional data sets are solely used for verification and not

Table 4.2: Identification cost values for different models

Dynamic Model	Parameters	J_θ	J_ψ	J
Fully Decoupled	13	0.89	0.74	1.63
Pitch and Yaw	30	0.70	0.83	1.53
Fully Coupled	66	0.41	0.65	1.07

Table 4.3: Verification cost values for different models

Dynamic Model	Parameters	J_θ	J_ψ	J
Fully Decoupled	13	0.39	1.04	1.43
Pitch and Yaw	30	0.72	1.13	1.85
Fully Coupled	66	1.50	4.67	6.17

used for parameter identification. The elevator and RPM commands from the experiments are applied to each of the dynamic models, and the outputs are recorded. The plots of the measured and predicted motion using the verification data set are shown in Figures 4.5, 4.6, 4.7, and 4.8. As a performance indicator, the cost functions presented earlier are employed, and the results are shown in Table 4.3.

From Table 4.2 and Table 4.3, we can draw preliminary conclusions about using conventional simplifying assumptions for the TRSMAUV. The fully coupled model uses more parameters, and the identification cost is lower than the other models employing simplifying assumptions. However during verification, Table 4.3 indicates that the models with fewer parameters have a lower cost to the fully coupled model. The higher verification cost of the fully coupled model indicates an over-fit with the identification data. The identification and verification cost values for the fully decoupled model and the pitch-axis and yaw-axis models are similar. Therefore standard simplifying assumptions are appropriate for the TRSMAUV, and the additional model complexity that arises with fewer modeling assumptions does not necessarily result in a better model.

4.4 Conclusion

We confirm that conventional simplify modeling assumptions are appropriate for the non-traditionally shaped TRSMAUV when performing decoupled motion. Future work includes designing and implementing attitude controllers for the TRSMAUV based on the systems identified in this chapter and investigating coupled depth and yaw motion.

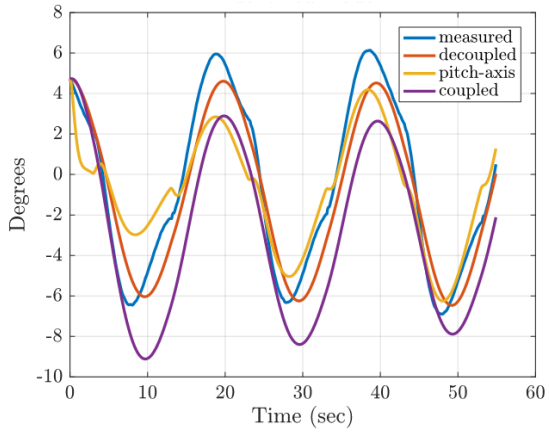

Figure 4.5: Pitch angle verification plot.

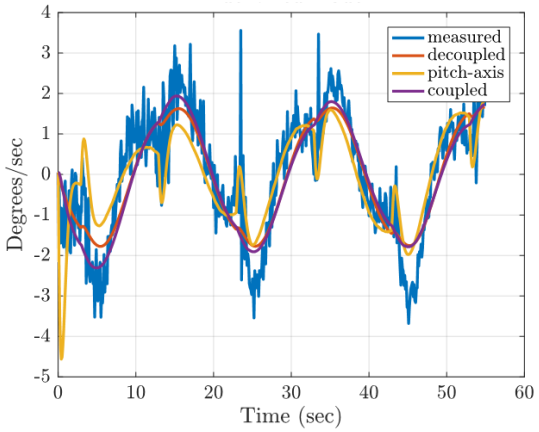

Figure 4.6: Pitch rate verification plot.

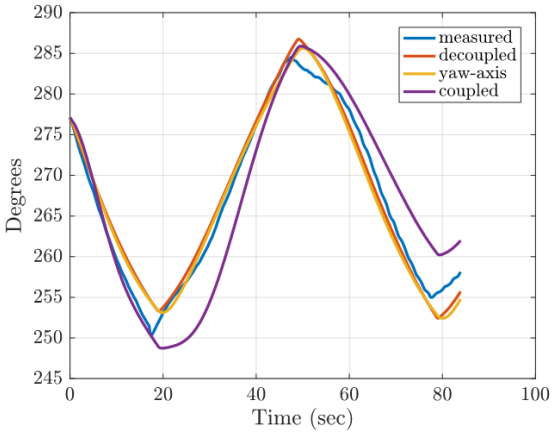

Figure 4.7: Yaw angle verification plot.

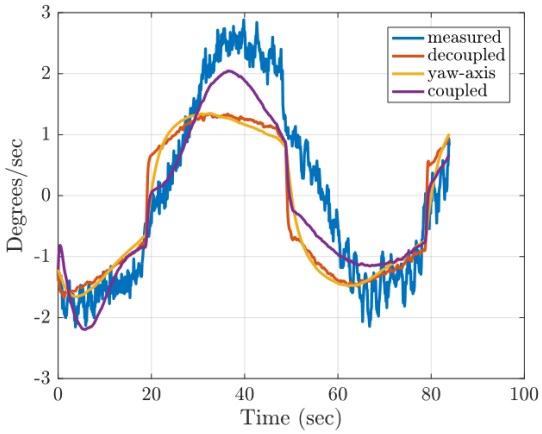

Figure 4.8: Yaw rate verification plot.

Chapter 5

Robust H_∞ Loop-Shaping Attitude Control Design

5.1 Introduction

An attitude controller for an autonomous underwater vehicle (AUV) uses actuators to stabilize the vehicle's heading and pitch while in motion. The principal contribution of our work is a process for designing a robust attitude controller based on loop-shaping ideas for a streamlined tail-controlled AUV. Our approach uses a loop-shaping procedure where the open-loop frequency response of the system is shaped to achieve desired closed-loop performance and robustness goals. We specifically address the challenge of adjusting the desired actuator bandwidth in a loop-shaping design framework. We present two control topologies that enable the designer to reduce or increase actuator bandwidth.

As the actuator bandwidth of an attitude control system increases, a system will generally exhibit improved tracking performance at the expense of actuators using more energy and wearing out sooner. For applications where tracking performance can be relaxed, actuator bandwidth can be smaller, leading to slower actuator movement and lower energy consumption. The trade-off between tracking performance and energy efficiency introduces a design requirement for actuator bandwidth guided by mission objectives.

Robust H_∞ control design has been addressed previously in [22, 36, 42, 53, 62, 67], but loop-shaping designs have not previously been considered for streamlined AUV applications.

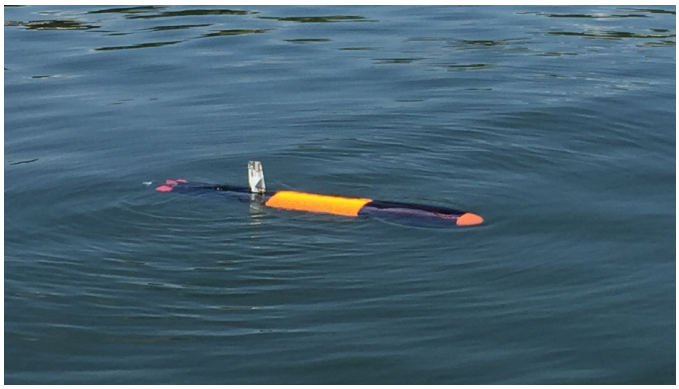

Figure 5.1: Virginia Tech 690S AUV

We use a loop-shaping design procedure proposed by McFarlane and Glover [49] that has been successfully implemented in a variety of applications such as [32] and [33]. The design procedure synthesizes an H_∞ controller to robustly stabilize the vehicle with respect to coprime factor uncertainty using classical loop-shaping techniques [28]. Weighting filters are selected to shape the open-loop response of the plant. We provide a method of choosing the weighting filters to shape the plant and adjust the actuator bandwidth.

A second topology, referred to as a two degree of freedom controller, is proposed by Hoyle [29] and Limebeer [40]. For this controller, the commands and feedback enter the controller separately and are independently processed. A reference model is introduced and represents the desired closed-loop transfer function. The two degree of freedom controller requires more design elements, but can be used if input tracking requirements are not satisfied by the loop-shaping design proposed by McFarlane and Glover.

In both control topologies, the prefilter normally includes an integrator. In some conditions, the integrator can wind up due to actuator saturation and compromise the stability of the AUV. For practical applications, we also present an anti-windup scheme that prevents integrator windup in the event that the vehicle's actuators saturate.

The Virginia Tech 690S AUV is shown in Figure 5.1 and is a smaller variant of the Virginia Tech 690 AUV presented in [46]. A series of attitude controllers are designed for

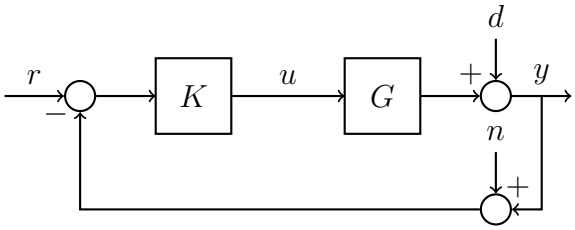

Figure 5.2: Control system topology

the Virginia Tech 690S AUV, using both of the approaches proposed herein, and evaluated experimentally. We present experimental data that confirms the efficacy of our proposed design procedures and our ability to achieve the required actuator bandwidth. Our results confirm that a controller with lower actuator bandwidth reduces actuator movement compared to a controller with higher actuator bandwidth. The results also demonstrate the trade-off between reference tracking performance and energy efficiency.

5.2 Loop-Shaping Methodology

A simple control loop topology is shown in Figure 5.2 where G is the system to be controlled, K is the controller, r is the reference input, u is the control input to the system, d is the output disturbance, y is the output, n is the output noise, and GK is the open-loop transfer function. From the block diagram, we can calculate the sensitivity function $S = (I + GK)^{-1}$ and the closed-loop transfer function $T = GK(I + GK)^{-1}$. With the sensitivity function and the closed-loop transfer function, we form the output and control input equations,

$$Y(s) = T(s)R(s) + S(s)D(s) - T(s)N(s) \tag{5.1}$$

$$U(s) = K(s)S(s)[R(s) - N(s) - D(s)]. \tag{5.2}$$

The maximum and minimum singular values of a matrix are denoted $\overline{\sigma}(\cdot)$ and $\underline{\sigma}(\cdot)$, respectively. From (5.1) and (5.2), we determine that for disturbance rejection $\overline{\sigma}(S)$ must be

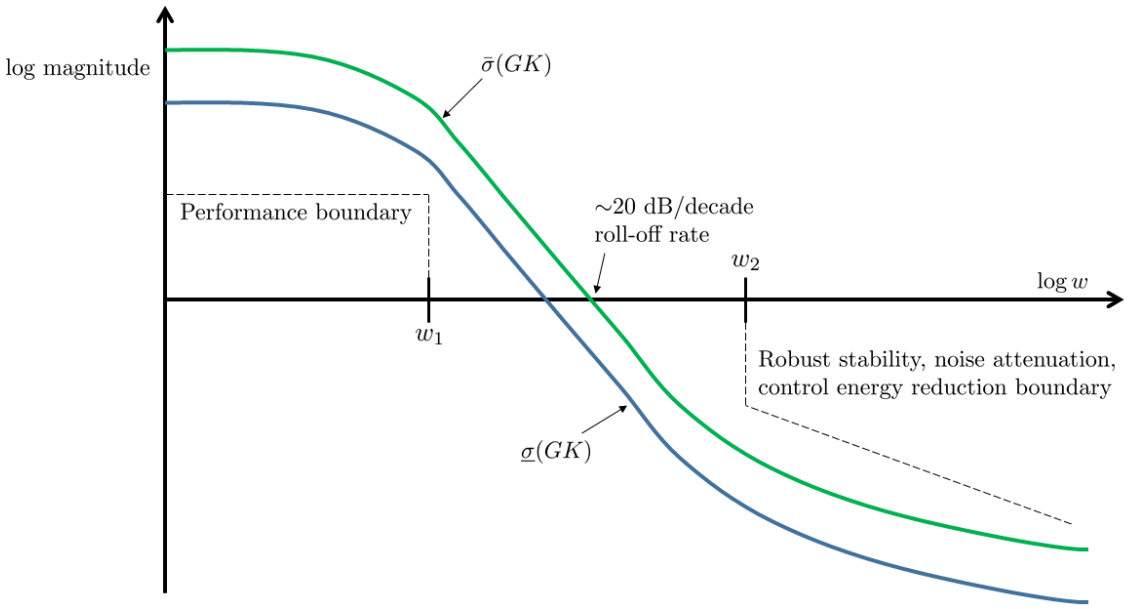

Figure 5.3: Classical loop-shaping methodology.

small for the frequency range of the disturbance, for noise attenuation $\overline{\sigma}(T)$ must be small in the frequency range of the noise, for reference tracking $\overline{\sigma}(T) \approx \underline{\sigma}(T) \approx 1$, and for lower bandwidth or control effort $\overline{\sigma}(KS)$ must be small. The closed-loop requirements for $\overline{\sigma}(S)$, $\sigma(T)$, and $\overline{\sigma}(KS)$ cannot be satisfied simultaneously. However, the closed-loop requirements can be achieved over certain frequency ranges. For example, noise is usually relevant at high frequencies, while disturbance rejection is important at low frequencies.

In classical loop-shaping, the magnitude of the open-loop transfer function GK is modified by appending weighting filters to the open-loop system GK. The largest singular values of S and T are related to the singular values of the open-loop system by approximating

$$\overline{\sigma}(S) \approx 1/\underline{\sigma}(GK) \tag{5.3}$$

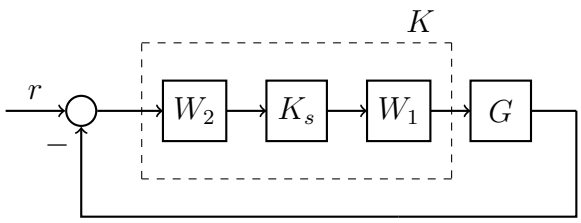

Figure 5.4: Shaped plant and controller.

at frequencies where $\underline{\sigma}(GK) \gg 1$ and

$$\overline{\sigma}(T) \approx \overline{\sigma}(GK) \tag{5.4}$$

when $\overline{\sigma}(GK) \ll 1$ [63]. The closed-loop requirements can be converted to open-loop objectives using (5.3) and (5.4). When shaping the open-loop transfer function GK at frequencies where $GK \gg 1$, $\underline{\sigma}(GK)$ must be large for good disturbance rejection and good reference tracking. When shaping the open-loop transfer function GK at frequencies where $GK \ll 1$, $\overline{\sigma}(GK)$ must be small for good noise attenuation and $\overline{\sigma}(K)$ must be small for energy efficiency. For single-input single-output systems, closed-loop stability is related to the roll-off rate, open-loop gain and open-loop phase near the crossover frequency [63]. Figure 5.3 shows how the singular values of the open-loop transfer function should be shaped.

5.3 Loop-Shaping Design Procedure

We adopt the loop-shaping design procedure proposed by McFarlane and Glover [49]. The procedure shapes the plant G with a prefilter W_1 and a postfilter W_2 shown in Figure 5.4 where $G_s = W_2 G W_1$. The open-loop singular values of the shaped plant G_s are shaped according to the classical shaping guidelines mentioned in Section 5.2 to achieve the desired performance.

After shaping G_s by selection of W_1 and W_2, an H_∞ controller K_s is synthesized that

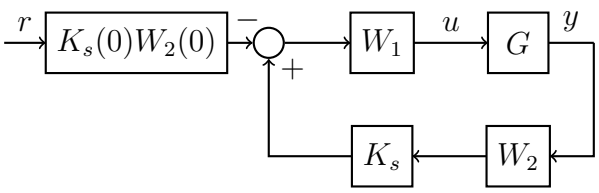

Figure 5.5: Alternate loop-shaping controller topology

robustly stabilizes the system with respect to the normalized coprime factorization for the shaped plant $G_s = M_s^{-1}N_s$. The H_∞ controller K_s can be synthesized by using the expressions in [28]. The final controller for the plant G is $K = W_1K_sW_2$ as shown in Figure 5.4. After generating K, the coprime uncertainty γ is computed as shown in [28]. For robust stability, $\gamma \geq 1$ should be as small as possible, and usually $\gamma < 4$ is required [63] which corresponds to 25% allowed coprime uncertainty.

A systematic approach to selecting the weighting filters W_1 and W_2 is presented in [32] and [63]. To satisfy the open-loop objectives, the singular values of $G_s = W_2GW_1$ usually require high gain at low frequencies, roll-off rate of about 20 dB/decade at the crossover frequency, and low gain at high frequencies. The postfilter W_2 is normally chosen to be a constant matrix. The weights in W_2 indicate the relative importance of signals to be controlled. The prefilter $W_1 = W_{bw}W_pW_i$ contains the dynamic shaping and is chosen to include integrators, phase-advance, phase-lag, and bandwidth gain. The integral terms in W_i increase tracking performance at low frequencies. Phase-advance W_p reduces the roll-off rate at the desired crossover frequency. Phase-lag W_p increases the roll-off rate at higher frequencies. The bandwidth gain W_{bw} is applied last to change the crossover frequency of the singular values. Some iteration is required to shape the singular values of G_s.

An alternate topology shown in Figure 5.5 is proposed by [32]. The alternate topology moves the synthesized H_∞ controller K_s to the feedback path so that changes in the reference commands do not excite the dynamics of the controller. Moving the controller to the feedback path can reduce large overshoot caused by changes in reference commands. Assuming integral

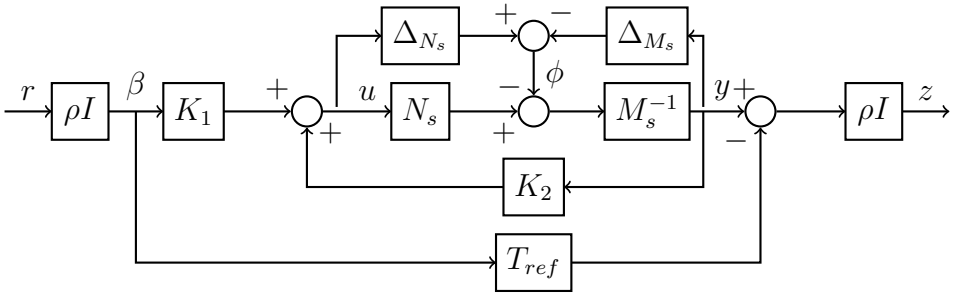

Figure 5.6: Two degree of freedom design configuration

terms in W_1 or G, a gain $K_s(0)W_2(0)$ is added to achieve a zero steady-state error. However, the input to the controller K is no longer the error between the reference command r and the measurement y. For an attitude controller using the alternate topology, improper command and measurement angle wrapping will cause unexpected controller behavior.

5.4 Two Degree of Freedom Controller

If strict time-domain requirements exist, the loop-shaping design procedure may not be sufficient. In Section 5.3, the loop-shaping design procedure produces a one degree of freedom controller that only utilizes the error signal between a reference command and a measurement. A two degree of freedom controller inputs both the feedback and the commands. An extension to the H_∞ loop-shaping design procedure of McFarlane and Glover is proposed by [29] and [40] for the two degree of freedom case. The problem is to find a stabilizing controller K for the shaped plant $G_s = M_s^{-1}N_s$ which minimizes the H_∞ norm between $[r^\mathsf{T}\ \phi^\mathsf{T}]^\mathsf{T}$ and $[u^\mathsf{T}\ y^\mathsf{T}\ z^\mathsf{T}]^\mathsf{T}$ where ϕ represents the uncertainty in the nominal plant model G and z is the output of the design configuration shown in Figure 5.6. The two degree of freedom controller design procedure employs a reference model T_{ref} chosen by the designer for the closed-loop system to follow. Another parameter ρ is also introduced to weigh relative importance of robust stabilization as compared with model reference matching. A thorough treatment of

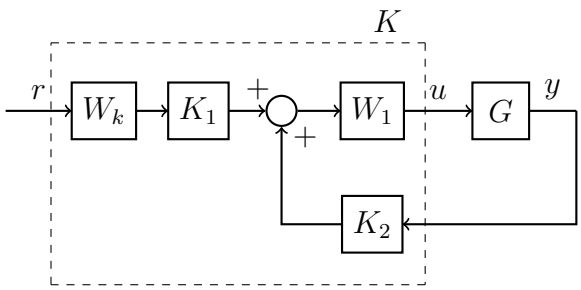

Figure 5.7: Two degree of freedom controller topology

the theory presented by [29] and [40] is omitted from this chapter. However, a systematic design procedure is presented and follows the proposed procedure in [63].

First, the open-loop singular values of G_s are shaped by designing a pre-compensating filter W_1 as explained in Section 5.3. Then a desired closed-loop reference model T_{ref} is chosen that represents the desired dynamic relationship between the commands and the outputs. The speed of the response of the closed-loop reference model T_{ref} must be realistic, or the closed-loop system will have poor robust stability properties and the controller will produce excessive control signals [29]. The design parameter ρ is selected between 1 and 3 to emphasize robust stability or model matching. With these design choices, one can setup the standard Ricatti equations associated with H_∞ controller synthesis whose solutions yield K_1 and K_2 in the Figure 5.7. A pre-filter W_k is required to achieve good model matching at steady-state where $W_k = [(I - G_s(0)K_2(0))^{-1}G_s(0)K_1(0)]^{-1}T_{ref}(0)$. In our iterative approach, the performance of the synthesized controller is evaluated and the values of ρ, W_1, and T_{ref} are adjusted if another control design iteration is required.

5.5 Anti-Windup Scheme

Windup occurs by the interaction of actuator saturation and integral action of a controller. When an actuator saturates, a controller with an integrator will continue to integrate the error and may cause the integral term to become large, which is known as wind-up.

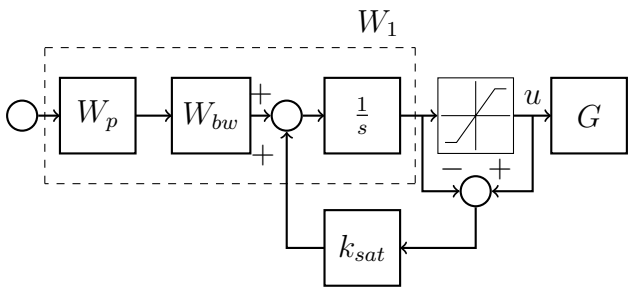

Figure 5.8: W_1 with anti-windup topology

In this work, we implement a back calculation anti-windup scheme. The weighting filter W_1 from Section 5.3 usually has an integrator to improve low frequency tracking performance. The integrator from W_1 can be separated as shown in the block diagram in Figure 5.8. When an actuator saturates, the difference between the control input after saturation u and the control input before saturation is multiplied by a saturation gain k_{sat}. The output of the block k_{sat} is added before the integrator. With a sufficiently large k_{sat}, the back calculation scheme prevents integrator wind-up.

5.6 690S Controller Design

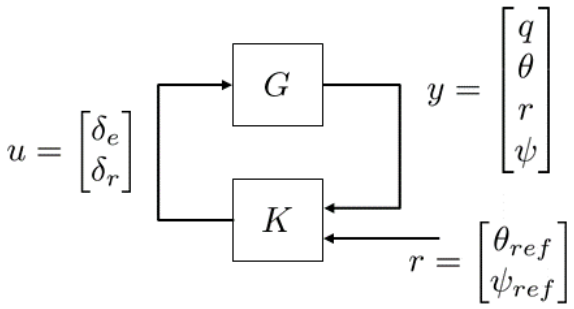

Figure 5.9: Block diagram of the Virginia Tech 690S plant G and controller K.

The Virginia Tech 690S AUV shown in Figure 5.1 is used to evaluate the controller design procedure proposed herein. The AUV diameter is 17.53 centimeters (6.90 inches), length is 1.55 meters, and weight is 27.67 kilograms. It is ballasted to be slightly positively buoyant.

The Virginia Tech 690S AUV has a single propeller at the stern of the vehicle, and it has four control surfaces at the tail. The vehicle also has an attitude and heading reference sensor (AHRS) that measures attitude, body relative rotation rates, and translation accelerations.

The system identification technique presented in [54] is used to generate the 690S AUV system model given in (B.2). For the 690S dynamic model, there are two actuator commands $u = [\delta_e \ \delta_r]^\mathsf{T}$ and four measurements $y = [q \ \theta \ r \ \psi]^\mathsf{T}$, where δ_e is the elevator deflection, δ_r is the rudder deflection, q is the AUV body pitch rate, θ is the AUV pitch angle, r is the AUV body yaw rate, and ψ is the AUV heading or yaw angle. The largest singular values of the nominal system plant G are plotted in Figure 5.10a.

In the following sections, the designs of one and two degree of freedom controllers with actuator bandwidths of 1.0 rad/sec, 1.5 rad/sec, and 2.0 rad/sec are presented for the Virginia Tech 690S AUV. All 690S attitude controllers are designed to control the pitch angle θ and yaw angle ψ of the vehicle. The weighting filter W_2 is the same for all controllers. Figure 5.9 shows the block diagram of the interconnection between the Virginia Tech 690S plant G and controller K.

5.6.1 Loop-Shaping Design Procedure

Recall that $W_1 = W_{bw} W_p W_i$. For good tracking performance and disturbance rejection, the smallest singular values at low frequencies must be large. An integrator increases the singular values at low frequencies and thus improves low frequency tracking performance. Both pitch and yaw channels include an integrator $W_i = 1/s$. The roll-off rate increases due to the addition of an integrator. The weight

$$W_p = \frac{(s + 0.5)(s + 0.6)}{s + 2} \tag{5.5}$$

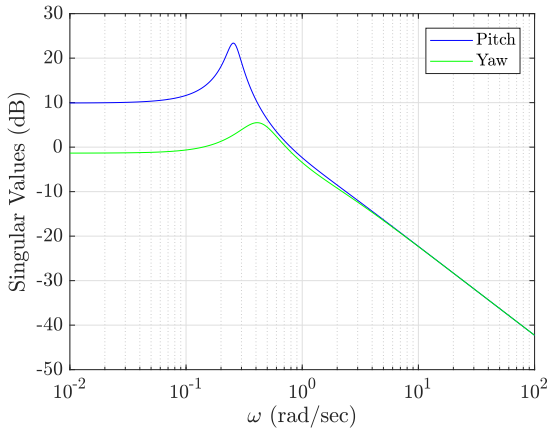

(a) Nominal largest singular values for the pitch and yaw channels

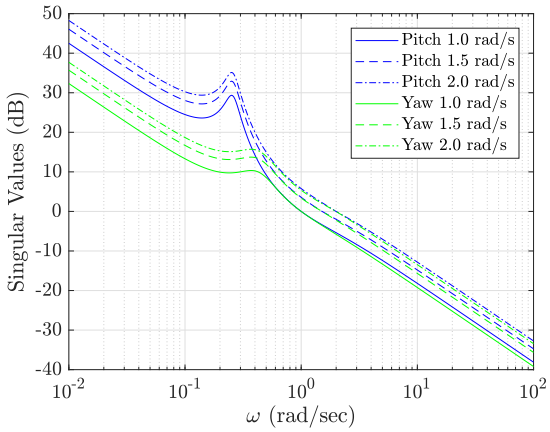

(b) Largest singular values of the shaped plants for the pitch and yaw channels at bandwidths of 1.0 rad/sec (solid line), 1.5 rad/sec (dashed line), and 2.0 rad/sec (dashed-dot line)

Figure 5.10: Plant singular values

Table 5.1: The coprime uncertainty γ for each controller design

Procedure	1.0 rad/sec	1.5 rad/sec	2.0 rad/sec
One degree of freedom	2.1363	2.0115	1.9559
Two degree of freedom	2.6118	2.3877	2.2896

is used to add phase-lead that reduces the roll-off rate at the desired crossover frequency and to add phase-lag that increases the roll-off rate at high frequencies. Desired controller bandwidths are selected to be 1.0 rad/sec, 1.5 rad/sec, and 2.0 rad/sec to confirm that a controller with lower actuator bandwidth reduces actuator movement compared to a controller with a higher bandwidth. By plotting the largest singular values of GW_pW_i, we chose the bandwidth gain W_{bw} to move the crossover frequency to the desired controller bandwidth. For the pitch channel, bandwidth gains of $W_{bw} = 3.073$ dB, $W_{bw} = 6.637$ dB, and $W_{bw} = 8.843$ dB change the open-loop bandwidth of our system to 1.0 rad/sec, 1.5 rad/sec, and 2.0 rad/sec, respectively. Similarly for the yaw channel, bandwidth gains $W_{bw} = 4.164$ dB, $W_{bw} = 7.544$ dB, and $W_{bw} = 9.534$ dB change the open-loop bandwidth of our system to 1.0 rad/sec, 1.5 rad/sec, and 2.0 rad/sec, respectively.

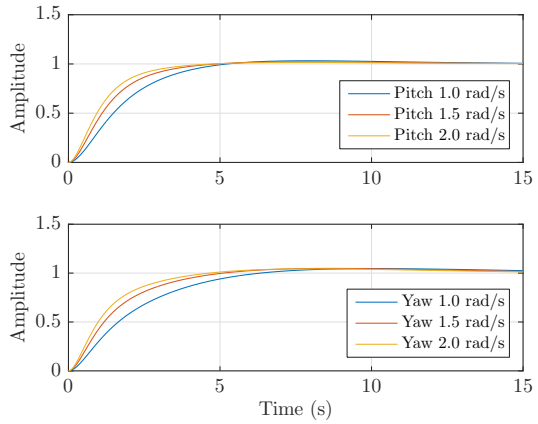

(a) Step responses using the loop-shaping design procedure for the pitch and yaw channels at bandwidths of 1.0 rad/sec, 1.5 rad/sec, and 2.0 rad/sec

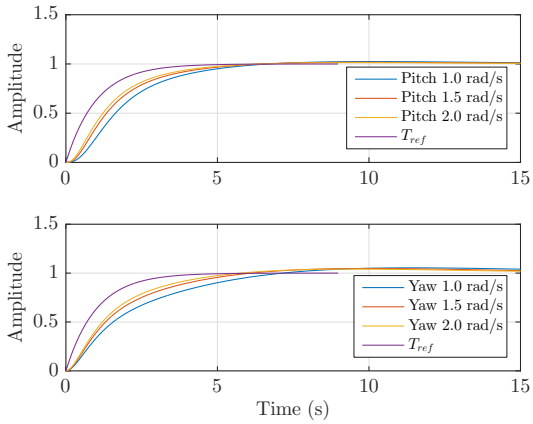

(b) Step responses using a two degree of freedom design for the pitch and yaw channels at bandwidths of 1.0 rad/sec, 1.5 rad/sec, and 2.0 rad/sec

Figure 5.11: Closed-loop step responses for one and two degree of freedom controllers

Finally, we select $W_2 = \text{diag}\{1, 2, 1, 2\}$ because pitch and yaw angle tracking are more important than nonzero angular rates. The largest open-loop singular values of the shaped plant $G_s = W_2 G W_1$ are shown in Figure 5.10b. With the shaped plants G_s designed with different crossover frequencies, an H_∞ controller is synthesized for each shaped plant. The coprime uncertainty γ is $\gamma = 2.1363$, $\gamma = 2.0115$, and $\gamma = 1.9559$ for controller bandwidths of 1.0 rad/sec, 1.5 rad/sec, and 2.0 rad/sec, respectively. The step responses for the alternate control topology using the synthesized H_∞ controllers are shown in Figure 5.11a.

5.6.2 Two Degree of Freedom Controller

If the controller developed using the loop-shaping design procedure proposed by McFarlane and Glover does not meet performance requirements, a two degree of freedom controller can be designed. For our purposes, we seek to design controllers with the same bandwidths as the one degree of freedom controller and compare actuator movement. As such, we select a

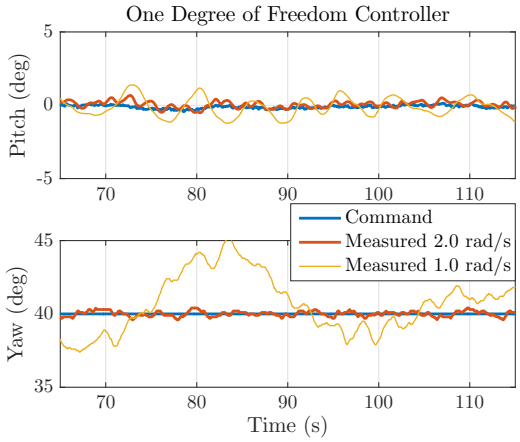

(a) Attitude tracking at a steady-state depth for the one degree of freedom controllers.

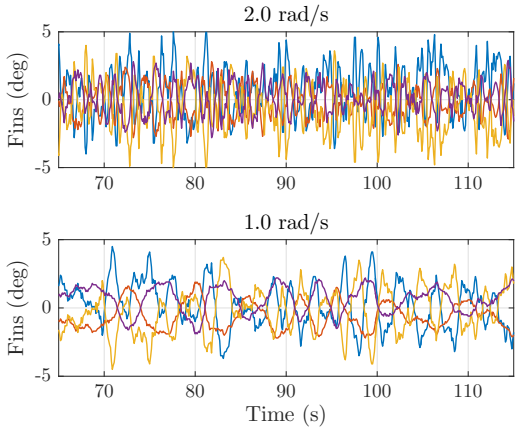

(b) Fin angles at a steady-state depth for the one degree of freedom controllers.

Figure 5.12: Attitude and fin angle at a steady-state depth using a one degree of freedom controller design.

reference model

$$T_{ref} = \frac{1}{s+1} \tag{5.6}$$

for a good closed-loop response that is achievable and a $\rho = 1$ for more emphasis on robust stability. A higher value of ρ would put more emphasis on reference model matching. Using T_{ref}, ρ, and the same prefilter W_1 from Section 5.6.1, an H_∞ controller is synthesized for each shaped plant. The coprime uncertainty γ is $\gamma = 2.6118$, $\gamma = 2.3877$, and $\gamma = 2.2896$ for controller bandwidths of 1.0 rad/sec, 1.5 rad/sec, and 2.0 rad/sec, respectively. After synthesizing the H_∞ controller, the step responses using the synthesized H_∞ controllers are shown in Figure 5.11b.

5.7 Field Trials

After generating the controllers from Section 5.6.1 and Section 5.6.2, the controllers were implemented on the Virginia Tech 690S AUV and subsequently evaluated in the field. Data sets were acquired during experiments performed at Claytor Lake in Pulaski County, Vir-

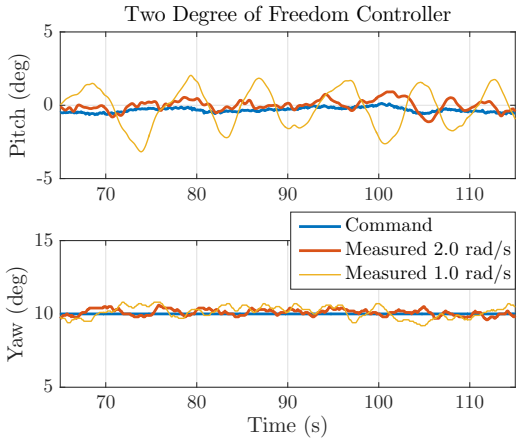

(a) Attitude tracking at a steady-state depth for the two degree of freedom controllers.

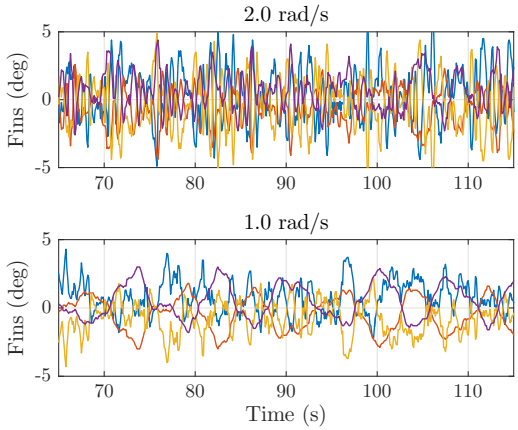

(b) Fin angles at a steady-state depth for the two degree of freedom controllers.

Figure 5.13: Attitude and fin angle at a steady-state depth using a two degree of freedom controller design.

ginia. The data collected from the experiments consisted of level-flight at a 2.0 meter depth for 3 minutes. For all controllers, the 690S operated at a propeller speed of 1500 rpm, which corresponds to a surge velocity of approximately 1.65 meters/sec. Only the results for the 1.0 rad/sec and 2.0 rad/sec controllers are shown to illustrate differences between tracking performance and actuator movement.

For a performance metric to compare controllers, we employ the average of the squared values defined

$$P(e) = \frac{\sum_{j=1}^{n} [e(j)]^2}{n} \tag{5.7}$$

where n is the number of samples and $e(j)$ is the performance signal. We use pitch error θ_e, yaw error ψ_e, elevator rate $\dot{\delta_e}$, and rudder rate $\dot{\delta_r}$ as performance signals $e(j)$ to compare the attitude controllers. For example, $P(\theta_e)$ would be the would be the average of the squared pitch error.

Figure 5.12a and 5.13a show the one and two degree of freedom attitude tracking results after achieving a steady-state depth. Figure 5.12b and 5.13b show the value of the four fin

Table 5.2: Virginia Tech 690S AUV controller performance P

Controller	$P(\theta_e)$	$P(\psi_e)$	$P(\dot{\delta}_e)$	$P(\dot{\delta}_r)$
1D 1.0 rad/sec	0.384	9.036	28.978	3.476
1D 2.0 rad/sec	0.065	0.041	145.285	38.688
2D 1.0 rad/sec	1.322	0.333	36.905	1.954
2D 2.0 rad/sec	0.185	0.056	178.912	58.451

command angles after achieving a steady-state depth. For all the controllers evaluated, the 690S AUV is able to achieve and maintain stable flight in response to reference commands. Our results show that both design procedures generate robust stabilizing attitude controllers.

For both the one and two degree of freedom controllers, the fin movement in Figure 5.12b and 5.13b is reduced as the controller bandwidth decreases. Comparing the value of $P(\dot{\delta}_e)$ for the 2.0 rad/sec and the 1.0 rad/sec controllers in Table 5.2 shows that $P(\dot{\delta}_e)$ decreases for elevator rate, meaning the actuator rate or movement is higher for 2.0 rad/sec controllers. A similar result exists for rudder rate using $P(\dot{\delta}_r)$. However, there is a trade-off between tracking performance and bandwidth. The controllers with the lowest bandwidth have less actuator movement, but the yaw and pitch reference tracking is worse than the controllers with the highest bandwidth. In Table 5.2, the value of $P(\theta_e)$ for 2.0 rad/sec controllers is smaller than for the 1.0 rad/sec controllers, meaning there is less pitch tracking error. The same conclusion can be drawn for the yaw tracking error by using $P(\psi_e)$.

From Figure 5.12a, 5.13a and Table 5.2, the steady-state results for 1.0 rad/sec one and two degree of freedom controllers can be compared. The 1.0 rad/sec one degree of freedom pitch steady-state error is smaller than the two degree of freedom pitch steady-state error. Recall that the two degree of freedom ρ chosen for this design emphasized robust stability instead of reference tracking. For more reference control, ρ can be increased and T_{ref} can be changed, but this reduces the importance of robust stability.

The 690S AUV is given a depth command that generates the pitch command input for the H_∞ attitude controller. Step pitch commands were not attempted. A 2.0 meter depth

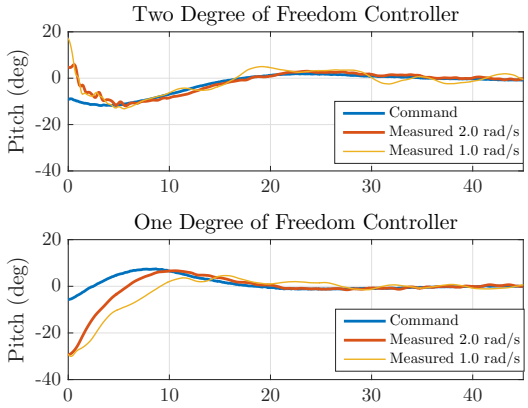

(a) Transient pitch tracking for one and two degree of freedom controllers.

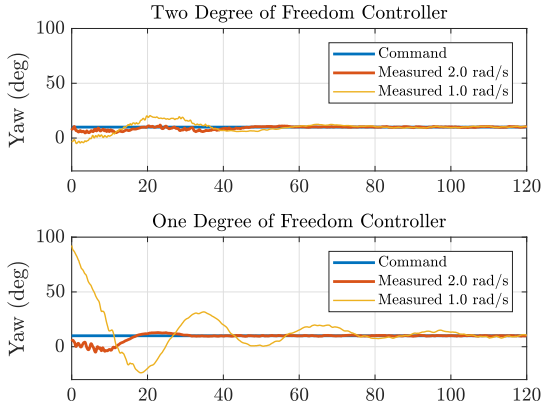

(b) Transient yaw tracking for one and two degree of freedom controllers.

Figure 5.14: Transient attitude tracking for one and two degree of freedom controllers.

command generated the transient pitch commands and measured pitch angles in Figure 5.14a. The pitch commands are not step inputs, but the tracking performance for the controllers is shown. As expected, the 2.0 rad/sec one degree of freedom controller has a faster rise time and smaller steady-state error compared to the 1.0 rad/sec controller. For the two degree of freedom controllers, both of the controllers appear to have similar rise times, but the 2.0 rad/sec controller has smaller steady-state error. A plot of the yaw angle transient is shown in Figure 5.14b.

5.8 Conclusion

The loop-shaping design procedure provides a way to produce stabilizing robust H_∞ attitude controllers for AUVs using classical loop-shaping techniques. We confirm through our results that a controller with a lower bandwidth reduces actuator movement compared to a controller with a higher bandwidth. The experimental results also show the trade-off between reference tracking performance and control effort.

Chapter 6

Receding Horizon H_∞ Control of Hidden Markov Jump Linear Systems

In this chapter, we consider the scenario of an autonomous vehicle operating in a high-disturbance environment where the disturbances are stochastic and non-stationary. We assume that we have probabilistic information about future disturbances. We seek a control algorithm that incorporates future probabilistic information and provides a formal robustness guarantee. To investigate this problem, we consider the control framework of model predictive control and Markov jump linear systems.

Model predictive control originated in the late seventies and has been used in various industries [7, 58]. The basic idea of model predictive control is three-fold: 1) make explicit use of a model to predict the output at future time instants; 2) calculate the control sequence that minimizes a cost function; and 3) use a receding horizon strategy where only the first control signal is applied. In a model predictive control framework, it is natural to incorporate feed forward control, and the framework is useful when future references are known in advance. However, model predictive control is computationally intensive at each time step and needs an appropriate model of the process and disturbances in order to optimize the cost function.

Markov jump linear systems (MJLS) have been used in applications ranging from finance, communication, and robotics due to their ability to model abrupt changes in system dynamics [16]. A MJLS is a discrete-time linear state equation whose coefficient matrices are indexed by a Markov chain. The MJLS framework can incorporate probabilistic knowl-

Figure 6.1: Virginia Tech 690 AUV conducting surveys near the Coleman Memorial Bridge in Yorktown, Virginia.

edge of future disturbances using transition probability matrices. Additionally, theoretical guarantees regarding stability and expected performance can be derived using a large body of literature. For this chapter, we employ a Markov jump linear system framework to model the stochastic and non-stationary disturbances experienced by the vehicle.

6.1 Introduction

Our main contribution is for time-inhomogeneous MJLS with partial observations of the Markov chain where the Markov parameter transition probabilities are non-stationary, such as in the practical case of robots operating in high disturbance environments where the disturbances are non-stationary. Additionally, we assume the transition probabilities vary in a finite set and consider the case where a finite sequence of future transition probabilities is known.

Control of switched systems with a receding horizon knowledge of modal information has

been investigated by Essick, Lee, and Dullerud in [20, 21]. In their formulation, the controller has access to past modal information and future modal information in a receding horizon sense. The critical component of the formulation depends on the existence of a Lyapunov function that depends on a finite sequence of past system parameters (finite-path dependent) [39]. We adapt this idea to seek finite-future dependent Lyapunov functions that depend on a sequence of future transition probabilities and an estimate of the current Markov chain state.

Time-inhomogenous MJLS have been studied in the literature. Aberkane [1] gives necessary and sufficient conditions for stochastic disturbance attenuation using an infinite set of linear matrix inequalities (LMIs). Lutz and Stilwell [44] provide stability and disturbance attenuation results in the form of a finite set of LMIs given that the set of transition probabilities is finite and that a finite-path dependent Lyapunov function exists. However, both papers depend on the assumption that the Markov chain is known.

Some previous work involving hidden or partial observation of the Markov chain include [12, 13, 17, 65]. In [13], the Markov chain is assumed to be inaccessible, and the authors develop a mode-independent solution. Robust mode-independent controllers yield conservative results when compared to a mode-dependent controller. Another approach is proposed in [12, 17] where there is a detector that provides an estimate of the Markov chain state. In this approach, the controller has access to the output of the detector instead of the true Markov chain state. The effectiveness of the detector-based approach is highly dependent on the estimation performance of the detector.

In this work, we use a detector-based approach and derive sufficient conditions for a new Bounded Real Lemma for a discrete-time time-inhomogeneous MJLS with receding horizon knowledge of the sequence of future transition probabilities. We provide an output feedback H_∞ control synthesis algorithm expressed as a finite set of linear matrix inequalities that can be efficiently solved. A numerical simulation example is presented followed by some

concluding remarks.

6.2 Preliminaries

A Markov jump linear system is a discrete-time linear state equation whose coefficient matrices are indexed by a Markov chain,

$$\begin{bmatrix} x(k+1) \\ z(k) \\ y(k) \end{bmatrix} = \begin{bmatrix} A(\vartheta_k) & B_1(\vartheta_k) & B_2(\vartheta_k) \\ C_1(\vartheta_k) & D_{11}(\vartheta_k) & D_{12}(\vartheta_k) \\ C_2(\vartheta_k) & D_{21}(\vartheta_k) & 0 \end{bmatrix} \begin{bmatrix} x(k) \\ w(k) \\ u(k) \end{bmatrix} \tag{6.1}$$

where k is the discrete-time index, $x(k) \in \mathbb{R}^n$ is the state vector, $z(k) \in \mathbb{R}^{p_1}$ is the error output, $y(k) \in \mathbb{R}^{p_2}$ is the output, $w(k) \in \mathbb{R}^{m_1}$ is the disturbance input, $u(k) \in \mathbb{R}^{m_2}$ is the control input, and $\vartheta(k) \in \mathcal{N}$ is the scheduling parameter that varies with time in a finite set $\mathcal{N} = \{1, 2, \ldots, N\}$. For notational convenience, let $\vartheta(k) = \vartheta_k$ and $\vartheta(k+1) = \vartheta_{k+1}$.

From Chapter 2, we define $r_M(k) := [\varphi(k+1), \varphi(k+2), \ldots, \varphi(k+M)]$ to be the next M values of the switching sequence at time k and Ψ_M to be the set of all sequences of length M. In this chapter, we assume that we have a receding horizon knowledge the sequence of transition probabilities. Specifically, at time k, we know the next M values of the switching sequence, $r_M(k)$.

In this chapter, we assume that the scheduling parameter ϑ_k is not directly observed. We employ a detector-based approach proposed in [17] where there is a signal $\hat{\vartheta}_k \in \mathcal{N}$ that depends only on ϑ_k. This assumption implies

$$\mathbf{P}\left\{\hat{\vartheta}_k = l \,\middle|\, \hat{\mathcal{F}}_k\right\} = \mathbf{P}\left\{\hat{\vartheta}_k = l \,\middle|\, \vartheta_k\right\} = \alpha_{\vartheta_k l}$$

where $\hat{\mathcal{F}}_k := \{x(0), w(0), \vartheta(0), \hat{\vartheta}(0), \ldots, x(k), w(k), \vartheta(k)\}$, $l \in \mathcal{N}$, and $\{\alpha_{\vartheta_k l} \geq 0;\ \vartheta_k, l \in \mathcal{N}\}$

such that $\sum_l^N \alpha_{\vartheta_k l} = 1$.

Stability of time-inhomogeneous Markov jump linear systems is established in [44] using a finite-future dependent Lyapunov function. Let $\mathbb{S}_n^+$ be the set of symmetric positive-definite matrices.

Theorem 6.1. *(See [44, Theorem 4]) System (6.1) is UEMSS if and only if there exists $M \in \mathbb{N}_0$ and a function $X : \mathcal{N} \times \Psi_M \to \mathbb{S}_n^+$ such that*

$$A^\mathsf{T}(i) \sum_{j=1}^{N} \pi_{ij}(r_1(k)) X(j, r_M(k+1)) A(i) - X(i, r_M(k)) < 0 \tag{6.2}$$

for any $r_M(k), r_M(k+1) \in \Psi_M$ and $i \in \mathcal{N}$.

6.3 Stability and H_∞ Analysis

To simplify notation in this section, let $r_M(k) = r_M$, $\vartheta_k = i$, and $\hat{\vartheta}_k = l$. Consider the dynamic output feedback controller that is dependent on the detector signal l and the future M values of the switching sequence

$$\begin{bmatrix} \hat{x}(k+1) \\ u(k) \end{bmatrix} = \begin{bmatrix} \hat{A}(l, r_M) & \hat{B}(l, r_M) \\ \hat{C}(l, r_M) & \hat{D}(l, r_M) \end{bmatrix} \begin{bmatrix} \hat{x}(k) \\ y(k) \end{bmatrix} \tag{6.3}$$

where $\hat{x}(k) \in \mathbb{R}^n$ is the controller state, and $\{\hat{A}, \hat{B}, \hat{C}, \hat{D}\}$ are the controller matrices. Define $\bar{x}(k) = [x^\mathsf{T}(k)\ \hat{x}^\mathsf{T}(k)]^\mathsf{T}$ and the closed-loop system of equations $\mathbb{G}$ using (6.1) and (6.3) are

$$\begin{bmatrix} \bar{x}(k+1) \\ z(k) \end{bmatrix} = \begin{bmatrix} A(i, l, r_M) & B(i, l, r_M) \\ C(i, l, r_M) & D(i, l, r_M) \end{bmatrix} \begin{bmatrix} \bar{x}(k) \\ w(k) \end{bmatrix} \tag{6.4}$$

where

$$
\begin{aligned}
A(i,l,r_M) &= \begin{bmatrix} A(i) + B_2(i)\hat{D}(l,r_M)C_2(i) & B_2(i)\hat{C}(l,r_M) \\ \hat{B}(l,r_M)C_2(i) & \hat{A}(l,r_M) \end{bmatrix} \\
B(i,l,r_M) &= \begin{bmatrix} B_1(i) + B_2(i)\hat{D}(l,r_M)D_{21}(i) \\ \hat{B}(l,r_M)D_{21}(i) \end{bmatrix} \\
C(i,l,r_M) &= \begin{bmatrix} C_1(i) + D_{12}(i)\hat{D}(l,r_M)C_2(i) & D_{12}(i)\hat{C}(l,r_M) \end{bmatrix} \\
D(i,l,r_M) &= D_{11}(i) + D_{12}(i)\hat{D}(l,r_M)D_{21}(i).
\end{aligned}
$$

The closed-loop equations can be written to depend affinely on the controller matrices as

$$A(i,l,r_M) = \mathcal{A}(i) + \mathcal{B}_2(i)K(l,r_M)\mathcal{C}_2(i) \tag{6.5a}$$

$$B(i,l,r_M) = \mathcal{B}_1(i) + \mathcal{B}_2(i)K(l,r_M)\mathcal{D}_{21}(i) \tag{6.5b}$$

$$C(i,l,r_M) = \mathcal{C}_1(i) + \mathcal{D}_{12}(i)K(l,r_M)\mathcal{C}_2(i) \tag{6.5c}$$

$$D(i,l,r_M) = D_{11}(i) + \mathcal{D}_{12}(i)K(l,r_M)\mathcal{D}_{21}(i) \tag{6.5d}$$

and

$$
\mathcal{A}(i) = \begin{bmatrix} A(i) & 0 \\ 0 & 0 \end{bmatrix}, \quad
\mathcal{B}_1(i) = \begin{bmatrix} B_1(i) \\ 0 \end{bmatrix}, \quad
\mathcal{B}_2(i) = \begin{bmatrix} 0 & B_2(i) \\ I & 0 \end{bmatrix},
$$

$$
\mathcal{C}_1(i) = \begin{bmatrix} C_1(i) & 0 \end{bmatrix}, \quad
\mathcal{C}_2(i) = \begin{bmatrix} 0 & I \\ C_2(i) & 0 \end{bmatrix}, \quad
\mathcal{D}_{12}(i) = \begin{bmatrix} 0 & D_{12}(i) \end{bmatrix},
$$

$$
\mathcal{D}_{21}(i) = \begin{bmatrix} 0 \\ D_{21}(i) \end{bmatrix}, \quad
K(l,r_M) = \begin{bmatrix} \hat{A}(l,r_M) & \hat{B}(l,r_M) \\ \hat{C}(l,r_M) & \hat{D}(l,r_M) \end{bmatrix}.
$$

The following stability analysis theorem for a system that depends on the detector signal and the future M values of the switching sequence is inspired by Theorem 6.1.

Theorem 6.2. *System (6.4) is UEMSS if there exist a receding horizon dynamic output feedback controller (6.3), $M \in \mathbb{N}_0$, and a function $X : \mathcal{N} \times \Psi_M \to \mathbb{S}^+_{2n}$ such that*

$$\sum_{l\in\mathcal{N}} \alpha_{il} A^{\mathsf{T}}(i,l,r_M(k))\tilde{X}(i,r)A(i,l,r_M(k)) - X(i,r_M(k)) < 0 \tag{6.6}$$

for any $r_M(k) \in \Psi_M$ and $i \in \mathcal{N}$ where $r = [r_1(k), r_M(k+1)] \in \Psi_{M+1}$ and $\tilde{X}(i,r) = \sum_{j=1}^{N} \pi_{ij}(r_1(k))X(j,r_M(k+1))$.

Proof. Assume there exists a receding horizon dynamic output feedback controller (6.3), $M \in \mathbb{N}_0$, and function X such that the linear matrix inequalities (LMIs) in (6.6) are satisfied. Since the scheduling parameter varies in a finite set $\mathcal{N}$, the LMI (6.6) can be expressed

$$\bar{A}^{\mathsf{T}}(i,r_M(k)) \left[I_{N\times N} \otimes \tilde{X}(i,r)\right] \bar{A}(i,r_M(k)) - X(i,r_M(k)) < 0 \tag{6.7}$$

where $\otimes$ is the Kronecker product, $I_{N\times N}$ is the identity matrix of size $N \times N$, and

$$\bar{A}(i,r_M(k)) = \begin{bmatrix} \sqrt{\alpha_{i1}}A(i,1,r_M(k)) \\ \sqrt{\alpha_{i2}}A(i,2,r_M(k)) \\ \vdots \\ \sqrt{\alpha_{iN}}A(i,N,r_M(k)) \end{bmatrix}.$$

From Theorem 6.1, system (6.4) is UEMSS. □

We extend the results found in [44] and [65] to use a detector-based approach for a system that uses future probabilistic information of the scheduling parameter for time inhomogeneous MJLS and present a new Bounded Real Lemma. We define the following function to

simplify notation

$$\mathcal{B}_{ilr}\left(\tilde{X}(i,r)\right) \triangleq \begin{bmatrix} A(i,l,r_M(k)) & B(i,l,r_M(k)) \\ C(i,l,r_M(k)) & D(i,l,r_M(k)) \end{bmatrix}^{\mathsf{T}} \begin{bmatrix} \tilde{X}(i,r) & 0 \\ 0 & I \end{bmatrix} \begin{bmatrix} A(i,l,r_M(k)) & B(i,l,r_M(k)) \\ C(i,l,r_M(k)) & D(i,l,r_M(k)) \end{bmatrix}$$

where $r = [r_1(k), r_M(k+1)]$, $\pi_{ij}(r_1(k)) = \mathbf{P}\{\vartheta_{k+1} = j | \vartheta_k = i\}$, and

$$\tilde{X}(i,r) = \sum_{j=1}^{N} \pi_{ij}(r_1(k)) X(j, r_M(k+1)).$$

Theorem 6.3. *The system (6.4) is UEMSS with $\|\mathbb{G}\|_\infty < \gamma$ if there exist a receding horizon dynamic output feedback controller (6.3), $M \in \mathbb{N}_0$, and a function $X : \mathcal{N} \times \Psi_M \to \mathbb{S}_{2n}^+$ such that*

$$\sum_{l \in \mathcal{N}} \alpha_{il} \mathcal{B}_{ilr}\left(\tilde{X}(i,r)\right) < \begin{bmatrix} X(i, r_M(k)) & 0 \\ 0 & \gamma^2 I \end{bmatrix} \tag{6.8}$$

for any $r_M(k), r_M(k+1) \in \Psi_M$ and $i \in \mathcal{N}$ where $\vartheta_k = i$, $\hat{\vartheta}_k = l$.

Proof. Let $r_M(k) \in \Psi_M$ be arbitrary and assume that M and X exist such that the LMIs in (6.8) are satisfied. From the first diagonal entry in (6.8), we get

$$\sum_{l \in \mathcal{N}} \alpha_{il} A^{\mathsf{T}}(i,l,r_M(k)) \tilde{X}(i,r) A(i,l,r_M(k)) + C^{\mathsf{T}}(i,l,r_M(k)) C(i,l,r_M(k)) < X(i, r_M(k))$$

$$\sum_{l \in \mathcal{N}} \alpha_{il} A^{\mathsf{T}}(i,l,r_M(k)) \tilde{X}(i,r) A(i,l,r_M(k)) < X(i, r_M(k)).$$

So the system is UEMSS by applying Theorem 6.2. For notational convenience, let

$$\mathcal{M}(i,l,r_M) = \begin{bmatrix} A(i,l,r_M) & B(i,l,r_M) \\ C(i,l,r_M) & D(i,l,r_M) \end{bmatrix}. \tag{6.9}$$

Define

$$V(\vartheta_k, r_M(k), x(k)) = x^{\mathsf{T}}(k)X(i, r_M(k))x(k).$$

Assume that $x(0) = 0$ which implies that $V(\vartheta_0, r_M(0), x(0)) = 0$. Define $z_L(k)$ such that $z_L(k) = z(k)$ for $0 \leq k \leq L$ and $z_L(k) = 0$ for $k > L$. For notational convenience, let $r_M(k) = r_M$. Consider the telescoping sum

$$\sum_{k=0}^{L} \mathbf{E}\left[V(\vartheta_{k+1}, r_M(k+1), x(k+1)) - V(i, r_M, x(k))\right] = \mathbf{E}\left[V(\vartheta_{L+1}, r_M(L+1), x(L+1))\right] \geq 0. \tag{6.10}$$

Using (6.4) and (6.10)

$$\begin{aligned}
\|z_L\|_{l_2}^2 - \gamma^2\|w_L\|_{l_2}^2 &= \sum_{k=0}^{L} \mathbf{E}\left[z^{\mathsf{T}}(k)z(k) - \gamma^2 w^{\mathsf{T}}(k)w(k)\right] \\
&\leq \sum_{k=0}^{L} \mathbf{E}\left[z^{\mathsf{T}}(k)z(k) - \gamma^2 w^{\mathsf{T}}(k)w(k)\right. \\
&\quad \left. + V(\vartheta_{k+1}, r_M(k+1), x(k+1)) - V(i, r_M, x(k))\right]. \\
&= \sum_{k=0}^{L} \mathbf{E}\left\{\begin{bmatrix}\bar{x}(k)\\ w(k)\end{bmatrix}^{\mathsf{T}} \left(\mathcal{M}(i,l,r_M)^{\mathsf{T}} \begin{bmatrix} X(\vartheta_{k+1}, r_M(k+1)) & 0 \\ 0 & I\end{bmatrix}\right.\right. \\
&\quad \left.\left. \times \mathcal{M}(i,l,r_M) - \begin{bmatrix} X(i, r_M) & 0 \\ 0 & \gamma^2 I\end{bmatrix}\right) \begin{bmatrix}\bar{x}(k)\\ w(k)\end{bmatrix}\right\}
\end{aligned} \tag{6.11}$$

where (6.11) follows by substituting in the system dynamics. Using the law of iterated

expectation yields the following inequalities

$$\|z_L\|_{l_2}^2 - \gamma^2\|w_L\|_{l_2}^2 \leq \sum_{k=0}^{L} \mathbf{E}\left\{ \begin{bmatrix} \bar{x}(k) \\ w(k) \end{bmatrix}^{\mathsf{T}} \mathbf{E}\left(\mathcal{M}(i,l,r_M)^{\mathsf{T}} \begin{bmatrix} X(\vartheta_{k+1}, r_M(k+1)) & 0 \\ 0 & I \end{bmatrix} \right.\right.$$
$$\left.\left. \times \mathcal{M}(i,l,r_M) - \begin{bmatrix} X(i,r_M) & 0 \\ 0 & \gamma^2 I \end{bmatrix} \middle| \hat{\mathcal{F}}_k \right) \begin{bmatrix} \bar{x}(k) \\ w(k) \end{bmatrix} \right\} \tag{6.12}$$
$$= \sum_{k=0}^{L} \mathbf{E}\left\{ \begin{bmatrix} \bar{x}(k) \\ w(k) \end{bmatrix}^{\mathsf{T}} \sum_{l\in\mathcal{N}} \alpha_{il} \mathbf{E}\left(\mathcal{M}(i,l,r_M)^{\mathsf{T}} \begin{bmatrix} X(\vartheta_{k+1}, r_M(k+1)) & 0 \\ 0 & I \end{bmatrix} \right.\right.$$
$$\left.\left. \times \mathcal{M}(i,l,r_M) - \begin{bmatrix} X(i,r_M) & 0 \\ 0 & \gamma^2 I \end{bmatrix} \middle| \hat{\mathcal{F}}_k, l \right) \begin{bmatrix} \bar{x}(k) \\ w(k) \end{bmatrix} \right\}. \tag{6.13}$$

Using the properties of the expectation, (6.13) can be expressed

$$\|z_L\|_{l_2}^2 - \gamma^2\|w_L\|_{l_2}^2 \leq \sum_{k=0}^{L} \mathbf{E}\left\{ \begin{bmatrix} \bar{x}(k) \\ w(k) \end{bmatrix}^{\mathsf{T}} \sum_{l\in\mathcal{N}} \alpha_{il} \left(\begin{bmatrix} A(i,l,r_M) & B(i,l,r_M) \\ C(i,l,r_M) & D(i,l,r_M) \end{bmatrix}^{\mathsf{T}} \right.\right.$$
$$\times \begin{bmatrix} \mathbf{E}\left[X(\vartheta_{k+1}, r_M(k+1)) | \, \hat{\mathcal{F}}_k, l \right] & 0 \\ 0 & I \end{bmatrix} \begin{bmatrix} A(i,l,r_M) & B(i,l,r_M) \\ C(i,l,r_M) & D(i,l,r_M) \end{bmatrix}$$
$$\left.\left. - \begin{bmatrix} X(i,r_M) & 0 \\ 0 & \gamma^2 I \end{bmatrix} \right) \begin{bmatrix} \bar{x}(k) \\ w(k) \end{bmatrix} \right\} \tag{6.14}$$
$$= \sum_{k=0}^{L} \mathbf{E}\left\{ \begin{bmatrix} \bar{x}(k) \\ w(k) \end{bmatrix}^{\mathsf{T}} \sum_{l\in\mathcal{N}} \alpha_{il} \left(\begin{bmatrix} A(i,l,r_M) & B(i,l,r_M) \\ C(i,l,r_M) & D(i,l,r_M) \end{bmatrix}^{\mathsf{T}} \begin{bmatrix} \tilde{X}(i,r) & 0 \\ 0 & I \end{bmatrix} \right.\right.$$
$$\left.\left. \times \begin{bmatrix} A(i,l,r_M) & B(i,l,r_M) \\ C(i,l,r_M) & D(i,l,r_M) \end{bmatrix} - \begin{bmatrix} X(i,r_M) & 0 \\ 0 & \gamma^2 I \end{bmatrix} \right) \begin{bmatrix} \bar{x}(k) \\ w(k) \end{bmatrix} \right\}. \tag{6.15}$$

By assumption, the expectation in (6.15) is negative when $w(k) \neq 0$. Therefore, there exists an $\epsilon > 0$ such that $\|z_L\|_{l_2}^2 - \gamma^2\|w_L\|_{l_2}^2 < -\epsilon$. Taking the limit as $L \to \infty$ yields the desired result $\|z\|_{l_2}^2 < \gamma^2\|w\|_{l_2}^2$. □

Remark 6.4. If the detector has perfect observations of the scheduling parameter ϑ_k, our stability and Bounded Real Lemma results are the same as in [44].

6.4 Output Feedback H_∞ Control Synthesis

In this section, we consider the problem of synthesizing a dynamic output feedback controller that is dependent on the detector signal and the future M values of the switching sequence (6.3). The resulting controller will render the closed-loop system (6.4) UEMSS with an expected l_2 performance. The LMI methodology proposed follows the well-known LMI solution by Gahinet and Apkarian [24] and the more recent H_∞ contol results for time-inhomogeneous MJLS presented by Lutz and Stilwell [43]. The following synthesis theorem is inspired from [43, Theorem 6.17]. To simplify notation in this section, let $\vartheta_k = i$ and $\hat{\vartheta}_k = l$.

Theorem 6.5. *There exists a receding horizon dynamic output feedback controller as in (6.3) such that the closed-loop system in (6.4) is UEMSS with an H_∞ norm of $\|\mathbb{G}\|_\infty < \gamma$ if there exist $M \in \mathbb{N}_0$, $K(i, r_M) = \sum_l \alpha_{il} K(l, r_M)$, and functions $S, U : \mathcal{N} \times \Psi_M \to \mathbb{S}_n^+$ such that*

$$\begin{bmatrix} W_1(i) & 0 \\ W_2(i) & 0 \\ 0 & I \end{bmatrix}^{\mathsf{T}} \begin{bmatrix} A(i)U(i,r_M)A^{\mathsf{T}}(i) - \mathcal{U}(i,r) & A(i)U(i,r_M)C_1^{\mathsf{T}}(i) & B_1(i) \\ C_1(i)U(i,r_M)A^{\mathsf{T}}(i) & -I + C_1(i)U(i,r_M)C_1^{\mathsf{T}}(i) & D_{11}(i) \\ B_1^{\mathsf{T}}(i) & D_{11}^{\mathsf{T}}(i) & -\gamma^2 I \end{bmatrix} \begin{bmatrix} W_1(i) & 0 \\ W_2(i) & 0 \\ 0 & I \end{bmatrix} < 0 \quad (6.16a)$$

$$\begin{bmatrix} V_1(i) & 0 \\ V_2(i) & 0 \\ 0 & I \end{bmatrix}^{\mathsf{T}} \begin{bmatrix} A^{\mathsf{T}}(i)\tilde{S}(i,r)A(i) - S(i,r_M) & A^{\mathsf{T}}(i)\tilde{S}(i,r)B_1(i) & C_1^{\mathsf{T}}(i) \\ B_1^{\mathsf{T}}(i)\tilde{S}(i,r)A(i) & -\gamma^2 I + B_1^{\mathsf{T}}(i)\tilde{S}(i,r)B_1(i) & D_{11}^{\mathsf{T}}(i) \\ C_1(i) & D_{11}(i) & -I \end{bmatrix} \begin{bmatrix} V_1(i) & 0 \\ V_2(i) & 0 \\ 0 & I \end{bmatrix} < 0 \quad (6.16b)$$

$$\begin{bmatrix} S(i,r_M) & I \\ I & U(i,r_M) \end{bmatrix} > 0 \quad (6.16c)$$

for all $i \in \mathcal{N}$ and any $r_M(k) \in \Psi_M$, where $r = [r_1(k), r_M(k+1)] \in \Psi_{M+1}$; $[W_1^{\mathsf{T}}(i)\ W_2^{\mathsf{T}}(i)]^{\mathsf{T}}$

is any basis of $\ker[B_2^\mathsf{T}(i)\ D_{12}^\mathsf{T}(i)]$; $[V_1^\mathsf{T}(i)\ V_2^\mathsf{T}(i)]^\mathsf{T}$ *is any basis of* $\ker[C_2(i)\ D_{21}(i)]$; *and*

$$\tilde{S}(i,r) := \sum_{j=1}^{N} \pi_{ij}(r_1(k))S(j, r_M(k+1)),$$
$$\mathcal{U}(i,r) := \left(\sum_{j=1}^{N} \pi_{ij}(r_1(k))U^{-1}(j, r_M(k+1))\right)^{-1}.$$

Proof. Suppose that there exist $M \in \mathbb{N}_0$ and $U,\ S$ that satisfy (6.16). Define

$$X(i, r_M) = \begin{bmatrix} S(i,r_M) & U^{-1}(i,r_M) - S(i,r_M) \\ U^{-1}(i,r_M) - S(i,r_M) & S(i,r_M) - U^{-1}(i,r_M) \end{bmatrix} \tag{6.17}$$

$$\tilde{X}(i,r) = \begin{bmatrix} \tilde{S}(i,r) & \mathcal{U}(i,r) - \tilde{S}(i,r) \\ \mathcal{U}(i,r) - \tilde{S}(i,r) & \tilde{S}(i,r) - \mathcal{U}(i,r) \end{bmatrix} \tag{6.18}$$

where $i \in \mathcal{N}$, $r_M \in \Psi_M$, and $r = [r_1(k), r_M(k+1)] \in \Psi_{M+1}$. By the Schur complement, inequality (6.16c) implies $S(i,r_M) - U^{-1}(i,r_M) > 0$. The Schur complement of (6.17) ensures that $X(i,r_M) > 0$. Taking the inverse of the partitioned Lyapunov function (6.17) and the partitioned matrix (6.18) yields

$$X^{-1}(i,r_M) = \begin{bmatrix} U(i,r_M) & U(i,r_M) \\ U(i,r_M) & U(i,r_M)(U(i,r_M) - S^{-1}(i,r_M))^{-1}U(i,r_M) \end{bmatrix} \tag{6.19}$$

$$\left(\tilde{X}(i,r)\right)^{-1} = \begin{bmatrix} \mathcal{U}(i,r) & \mathcal{U}(i,r) \\ \mathcal{U}(i,r) & \mathcal{U}(i,r)\left(\mathcal{U}(i,r) - \left(\tilde{S}(i,r)\right)^{-1}\right)^{-1}\mathcal{U}(i,r) \end{bmatrix}. \tag{6.20}$$

With the first constraint (6.16a) and by following the same procedure in [24], we can construct the equivalent condition

$$\begin{bmatrix} W_1(i) & 0 \\ 0 & I \\ W_2(i) & 0 \end{bmatrix}^\mathsf{T} \begin{bmatrix} A(i)U(i,r_M)A^\mathsf{T}(i) - \mathcal{U}(i,r) & B_1(i) & A(i)U(i,r_M)C_1^\mathsf{T}(i) \\ B_1^\mathsf{T}(i) & -\gamma^2 I & D_{11}^\mathsf{T}(i) \\ C_1(i)U(i,r_M)A^\mathsf{T}(i) & D_{11}(i) & -I + C_1(i)U(i,r_M)C_1^\mathsf{T}(i) \end{bmatrix} \begin{bmatrix} W_1(i) & 0 \\ 0 & I \\ W_2(i) & 0 \end{bmatrix} < 0. \tag{6.21}$$

By matrix manipulation and (6.19), the matrix inequality (6.21) is expressed

$$\begin{bmatrix} W_1(i) & 0 \\ 0 & I \\ W_2(i) & 0 \end{bmatrix}^{\mathsf{T}} \left\{ \begin{bmatrix} -\mathcal{U}(i,r) & B_1(i) & 0 \\ B_1^{\mathsf{T}}(i) & -\gamma^2 I & D_{11}^{\mathsf{T}}(i) \\ 0 & D_{11}(i) & -I \end{bmatrix} + \begin{bmatrix} A(i)U(i,r_M)A^{\mathsf{T}}(i) & 0 & A(i)U(i,r_M)C_1^{\mathsf{T}}(i) \\ 0 & 0 & 0 \\ C_1(i)U(i,r_M)A^{\mathsf{T}}(i) & 0 & C_1(i)U(i,r_M)C_1^{\mathsf{T}}(i) \end{bmatrix} \right\} \begin{bmatrix} W_1(i) & 0 \\ 0 & I \\ W_2(i) & 0 \end{bmatrix} < 0$$

$$\begin{bmatrix} W_1(i) & 0 \\ 0 & I \\ W_2(i) & 0 \end{bmatrix}^{\mathsf{T}} \left\{ \begin{bmatrix} -\mathcal{U}(i,r) & B_1(i) & 0 \\ B_1^{\mathsf{T}}(i) & -\gamma^2 I & D_{11}^{\mathsf{T}}(i) \\ 0 & D_{11}(i) & -I \end{bmatrix} + \begin{bmatrix} A(i) & 0 \\ 0 & 0 \\ C_1(i) & 0 \end{bmatrix} X^{-1}(i,r_M) \begin{bmatrix} A(i) & 0 \\ 0 & 0 \\ C_1(i) & 0 \end{bmatrix}^{\mathsf{T}} \right\} \begin{bmatrix} W_1(i) & 0 \\ 0 & I \\ W_2(i) & 0 \end{bmatrix} < 0. \tag{6.22}$$

By the Schur complement, inequality (6.22) becomes

$$\left[\begin{array}{c|c|c} W_1(i) & 0 & 0 \\ \hline 0 & I & 0 \\ \hline 0 & 0 & I \\ W_2(i) & 0 & 0 \end{array}\right]^{\mathsf{T}} \left[\begin{array}{c|cc|cc} -\mathcal{U}(i,r) & A(i) & 0 & B_1(i) & 0 \\ \hline A^{\mathsf{T}}(i) & \multicolumn{2}{c|}{\multirow{2}{*}{$-X(i,r_M)$}} & 0 & C_1^{\mathsf{T}}(i) \\ 0 & & & 0 & 0 \\ \hline B_1^{\mathsf{T}}(i) & 0 & 0 & -\gamma^2 I & D_{11}^{\mathsf{T}}(i) \\ 0 & C_1(i) & 0 & D_{11}(i) & -I \end{array}\right] \left[\begin{array}{c|c|c} W_1(i) & 0 & 0 \\ \hline 0 & I & 0 \\ \hline 0 & 0 & I \\ W_2(i) & 0 & 0 \end{array}\right] < 0. \tag{6.23}$$

Adding a row of zeros to the basis null space matrices, we can express (6.23) as

$$\left[\begin{array}{c:cc} W_1(i) & 0 & 0 \\ 0 & 0 & 0 \\ \hdashline 0 & I & 0 \\ \hdashline 0 & 0 & I \\ W_2(i) & 0 & 0 \end{array}\right]^{\mathsf{T}} \left[\begin{array}{cc:cc:cc} -\mathcal{U}(i,r) & -\mathcal{U}(i,r) & A(i) & 0 & B_1(i) & 0 \\ -\mathcal{U}(i,r) & -\mathcal{R}(i,r) & 0 & 0 & 0 & 0 \\ \hdashline A^{\mathsf{T}}(i) & 0 & \multicolumn{2}{c:}{\multirow{2}{*}{$-X(i,r_M)$}} & 0 & C_1^{\mathsf{T}}(i) \\ 0 & 0 & & & 0 & 0 \\ \hdashline B_1^{\mathsf{T}}(i) & 0 & 0 & 0 & -\gamma^2 I & D_{11}^{\mathsf{T}}(i) \\ 0 & 0 & C_1(i) & 0 & D_{11}(i) & -I \end{array}\right] \left[\begin{array}{c:cc} W_1(i) & 0 & 0 \\ 0 & 0 & 0 \\ \hdashline 0 & I & 0 \\ \hdashline 0 & 0 & I \\ W_2(i) & 0 & 0 \end{array}\right] < 0. \quad (6.24)$$

Then (6.24) is equivalent to

$$W_{\mathcal{P}(i)}^{\mathsf{T}} \mathcal{H}(i,r) W_{\mathcal{P}(i)} < 0 \quad (6.25)$$

where

$$\mathcal{H}(i,r) = \begin{bmatrix} -\left(\tilde{X}(i,r)\right)^{-1} & \mathcal{A}(i) & \mathcal{B}_1(i) & 0 \\ \mathcal{A}^{\mathsf{T}}(i) & -X(i,r_M) & 0 & \mathcal{C}_1^{\mathsf{T}}(i) \\ \mathcal{B}_1^{\mathsf{T}}(i) & 0 & -\gamma^2 I & \mathcal{D}_{11}^{\mathsf{T}}(i) \\ 0 & \mathcal{C}_1(i) & \mathcal{D}_{11}(i) & -I \end{bmatrix},$$

$$\mathcal{P}(i) = \begin{bmatrix} \mathcal{B}_2^{\mathsf{T}}(i) & 0 & 0 & \mathcal{D}_{12}^{\mathsf{T}}(i) \end{bmatrix},$$

$$\mathcal{Q}(i) = \begin{bmatrix} 0 & \mathcal{C}_2(i) & \mathcal{D}_{21}(i) & 0 \end{bmatrix}.$$

Following the same procedure with the second constraint (6.16b), we can construct the

equivalent condition using matrix manipulation and (6.18)

$$\begin{bmatrix} V_1(i) & 0 \\ V_2(i) & 0 \\ 0 & I \end{bmatrix}^{\mathsf{T}} \left\{ \begin{bmatrix} -S(i,r_M) & 0 & C_1^{\mathsf{T}}(i) \\ 0 & -\gamma^2 I & D_{11}^{\mathsf{T}}(i) \\ C_1(i) & D_{11}(i) & -I \end{bmatrix} + \begin{bmatrix} A^{\mathsf{T}}(i)\tilde{S}(i,r)A(i) & A^{\mathsf{T}}(i)\tilde{S}(i,r)B_1(i) & 0 \\ B_1^{\mathsf{T}}(i)\tilde{S}(i,r)A(i) & B_1^{\mathsf{T}}(i)\tilde{S}(i,r)B_1(i) & 0 \\ 0 & 0 & 0 \end{bmatrix} \right\} \begin{bmatrix} V_1(i) & 0 \\ V_2(i) & 0 \\ 0 & I \end{bmatrix} < 0$$

$$\begin{bmatrix} V_1(i) & 0 \\ V_2(i) & 0 \\ 0 & I \end{bmatrix}^{\mathsf{T}} \left\{ \begin{bmatrix} -S(i,r_M) & 0 & C_1^{\mathsf{T}}(i) \\ 0 & -\gamma^2 I & D_{11}^{\mathsf{T}}(i) \\ C_1(i) & D_{11}(i) & -I \end{bmatrix} + \begin{bmatrix} A(i) & B_1(i) & 0 \\ 0 & 0 & 0 \end{bmatrix}^{\mathsf{T}} \tilde{X}(i,r) \begin{bmatrix} A(i) & B_1(i) & 0 \\ 0 & 0 & 0 \end{bmatrix} \right\} \begin{bmatrix} V_1(i) & 0 \\ V_2(i) & 0 \\ 0 & I \end{bmatrix} < 0. \quad (6.26)$$

By the Schur complement, inequality (6.26) becomes

$$\left[\begin{array}{c|c|c} 0 & I & 0 \\ \hline V_1(i) & 0 & 0 \\ \hline V_2(i) & 0 & 0 \\ 0 & 0 & I \end{array}\right]^{\mathsf{T}} \left[\begin{array}{c|c|cc} -\left(\tilde{X}(i,r)\right)^{-1} & A(i) & B_1(i) & 0 \\ & 0 & 0 & 0 \\ \hline A^{\mathsf{T}}(i) \quad 0 & -S(i,r_M) & 0 & C_1^{\mathsf{T}}(i) \\ \hline B_1^{\mathsf{T}}(i) \quad 0 & 0 & -\gamma^2 I & D_{11}^{\mathsf{T}}(i) \\ 0 \quad 0 & C_1(i) & D_{11}(i) & -I \end{array}\right] \left[\begin{array}{c|c|c} 0 & I & 0 \\ \hline V_1(i) & 0 & 0 \\ \hline V_2(i) & 0 & 0 \\ 0 & 0 & I \end{array}\right] < 0. \quad (6.27)$$

Adding a row of zeros to the basis null space matrices, we can express (6.27) as

$$\left[\begin{array}{c|c|c} 0 & I & 0 \\ \hline V_1(i) & 0 & 0 \\ 0 & 0 & 0 \\ \hline V_2(i) & 0 & 0 \\ 0 & 0 & I \end{array}\right]^{\mathsf{T}} \left[\begin{array}{c|cc|cc} -\left(\tilde{X}(i,r)\right)^{-1} & A(i) & 0 & B_1(i) & 0 \\ & 0 & 0 & 0 & 0 \\ \hline A^{\mathsf{T}}(i) & 0 & & 0 & C_1^{\mathsf{T}}(i) \\ 0 & 0 & -X(i,r_M) & 0 & 0 \\ \hline B_1^{\mathsf{T}}(i) & 0 & 0 & 0 & -\gamma^2 I \quad D_{11}^{\mathsf{T}}(i) \\ 0 & 0 & C_1(i) & 0 & D_{11}(i) \quad -I \end{array}\right] \left[\begin{array}{c|c|c} 0 & I & 0 \\ \hline V_1(i) & 0 & 0 \\ 0 & 0 & 0 \\ \hline V_2(i) & 0 & 0 \\ 0 & 0 & I \end{array}\right] < 0. \quad (6.28)$$

Then (6.28) is equivalent to

$$W_{\mathcal{Q}(i)}^{\mathsf{T}} \mathcal{H}(i,r) W_{\mathcal{Q}(i)} < 0. \quad (6.29)$$

If the constraints (6.25) and (6.29) are satisfied, then the following inequality is feasible in $K(i,r_M)$ by the Projection Lemma (see Lemma 2.6)

$$\mathcal{H}(i,r) + \mathcal{Q}^{\mathsf{T}}(i) K^{\mathsf{T}}(i,r_M) \mathcal{P}(i) + \mathcal{P}^{\mathsf{T}}(i) K(i,r_M) \mathcal{Q}(i) < 0 \quad (6.30)$$

where

$$\mathcal{H}(i,r) + \mathcal{Q}^{\mathsf{T}}(i) \sum_{l \in \mathcal{N}} \left[\alpha_{il} K^{\mathsf{T}}(l,r_M)\right] \mathcal{P}(i) + \mathcal{P}^{\mathsf{T}}(i) \sum_{l \in \mathcal{N}} \left[\alpha_{il} K(l,r_M)\right] \mathcal{Q}(i) < 0$$

follows by assumption. Then

$$\sum_{l \in \mathcal{N}} \alpha_{il} \left[\mathcal{H}(i,r) + \mathcal{Q}^{\mathsf{T}}(i) K^{\mathsf{T}}(l,r_M) \mathcal{P}(i) + \mathcal{P}^{\mathsf{T}}(i) K(l,r_M) \mathcal{Q}(i)\right] < 0 \quad (6.31)$$

follows by linearity. Equation (6.31) can be expressed

$$\sum_{l\in\mathcal{N}} \alpha_{il} \begin{bmatrix} -\left(\tilde{X}(i,r)\right)^{-1} & A(i,l,r_M) & B(i,l,r_M) & 0 \\ A^{\mathsf{T}}(i,l,r_M) & -X(i,r_M) & 0 & C^{\mathsf{T}}(i,l,r_M) \\ B^{\mathsf{T}}(i,l,r_M) & 0 & -\gamma^2 I & D^{\mathsf{T}}(i,l,r_M) \\ 0 & C(i,l,r_M) & D(i,l,r_M) & -I \end{bmatrix} < 0 \tag{6.32}$$

where $A(i,l,r_M)$, $B(i,l,r_M)$, $C(i,l,r_M)$, and $D(i,l,r_M)$ are defined by (6.5). By the Schur complement, the inequality (6.32) implies

$$\sum_{l\in\mathcal{N}} \alpha_{il} \begin{bmatrix} A(i,l,r_M) & B(i,l,r_M) \\ C(i,l,r_M) & D(i,l,r_M) \end{bmatrix}^{\mathsf{T}} \begin{bmatrix} \tilde{X}(i,r) & 0 \\ 0 & I \end{bmatrix} \begin{bmatrix} A(i,l,r_M) & B(i,l,r_M) \\ C(i,l,r_M) & D(i,l,r_M) \end{bmatrix} - \begin{bmatrix} X(i,r_M) & 0 \\ 0 & \gamma^2 I \end{bmatrix} < 0 \tag{6.33}$$

The result follows from Theorem 6.3. □

Remark 6.6. The matrix inequality constraints in (6.16) are not LMIs due to the term $\mathcal{U}(i,r)$. They can be converted to an equivalent LMI form using a trick from [25, Section 2] or [43, Lemma 6.15] which is omitted from this work.

Remark 6.7. If the detector is a perfect estimator of the scheduling parameter ϑ_k, Theorem 6.5 is the same as the synthesis theorem from [43, Theorem 6.17].

Remark 6.8. Suppose that U, S, and M are given and satisfy (6.16). A detector-dependent controller can be generated by constructing X from (6.17) and numerically solving an LMI problem using the LMI from (6.31).

Remark 6.9. If all other assumptions hold for Theorem 6.5, the assumption $K(i,r_M) = \sum_l \alpha_{il} K(l,r_M)$ guarantees the existence of a receding horizon dynamic output feedback controller that has the form (6.3). The probability of the detector indicating the scheduling

parameter is $\hat{\vartheta}_k = l$ with a true parameter of $\vartheta_k = i$ is denoted by $\alpha_{il} = \mathbf{P}\left\{\hat{\vartheta}_k = l \,\middle|\, \vartheta_k = i\right\}$ where $\sum_l^N \alpha_{il} = 1$. We define the matrix $\mathbf{A}$ as

$$\mathbf{A} = \begin{bmatrix} \alpha_{11} & \alpha_{12} & \cdots & \alpha_{1N} \\ \alpha_{21} & \alpha_{22} & \cdots & \alpha_{2N} \\ \vdots & \vdots & \ddots & \vdots \\ \alpha_{N1} & \alpha_{N2} & \cdots & \alpha_{NN} \end{bmatrix} \in \mathbb{R}^{N\times N}.$$

A good detector would have $\alpha_{il} \approx 1$ for $i = j$, and a perfect detector would be an identity matrix of size $N \times N$. The assumption can be rewritten as

$$\begin{bmatrix} K(\vartheta_k = 1, r_M) \\ K(\vartheta_k = 2, r_M) \\ \vdots \\ K(\vartheta_k = N, r_M) \end{bmatrix} = \mathbf{A} \begin{bmatrix} K(\hat{\vartheta}_k = 1, r_M) \\ K(\hat{\vartheta}_k = 2, r_M) \\ \vdots \\ K(\hat{\vartheta}_k = N, r_M) \end{bmatrix} \tag{6.34}$$

by using block matrix multiplication. For a unique set of controller matrices satisfying (6.34), $\mathbf{A}$ must be invertible and the controller matrices dependent on the detector can be calculated by

$$\mathbf{A}^{-1} \begin{bmatrix} K(\vartheta_k = 1, r_M) \\ K(\vartheta_k = 2, r_M) \\ \vdots \\ K(\vartheta_k = N, r_M) \end{bmatrix} = \begin{bmatrix} K(\hat{\vartheta}_k = 1, r_M) \\ K(\hat{\vartheta}_k = 2, r_M) \\ \vdots \\ K(\hat{\vartheta}_k = N, r_M) \end{bmatrix}.$$

As the rows of $\mathbf{A}$ sum to 1 and $\alpha_{il} \approx 1$ for $i = j$ for a good detector, the invertibility of $\mathbf{A}$ is guaranteed by the unique rows and unique columns of $\mathbf{A}$.

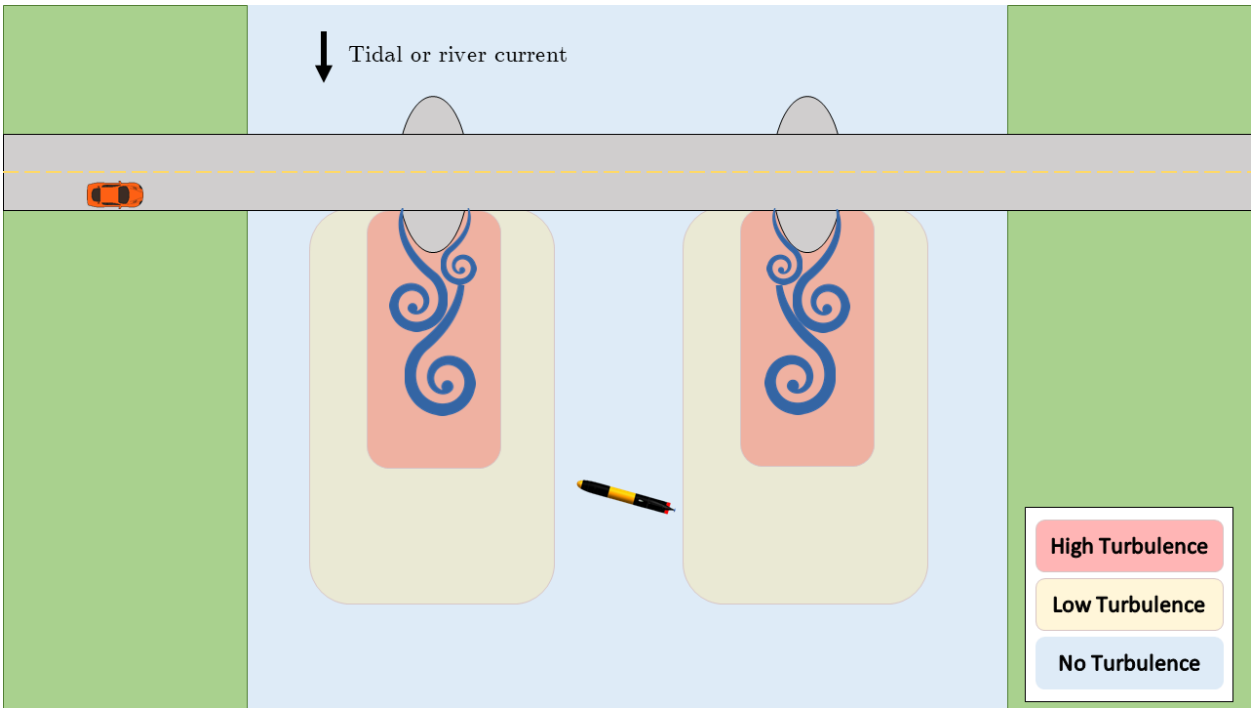

Figure 6.2: Prior map of estimated turbulence locations near a bridge where an AUV conducts surveys.

6.5 Numerical Simulations

We consider the scenario of an autonomous underwater vehicle (AUV) conducting an underwater inspection of a bridge. In a tidal or river current, a bridge pier sheds vortices that disturb the water downstream of the pier. The AUV conducting surveys of the piers will experience additional forces and moments due to the water disturbances in the wake of the pier. Let $\vartheta(t)$ be location dependent where $\vartheta(t) = 1$ represents the state where the AUV does not experience additional disturbances and $\vartheta(t) = 2$ represents the state where the AUV experiences additional disturbances from the wake of the pier. We assume that we have a detector in the form of a prior map of estimated turbulence locations in Figure 6.2. Let the output of our detector $\hat{\vartheta}(t)$ be location dependent where $\hat{\vartheta}(t) = 1$ represents the blue no turbulence region in Figure 6.2 and $\hat{\vartheta}(t) = 2$ represents the red and yellow turbulence region in Figure 6.2. Note that our prior map is only an estimate of turbulence locations.

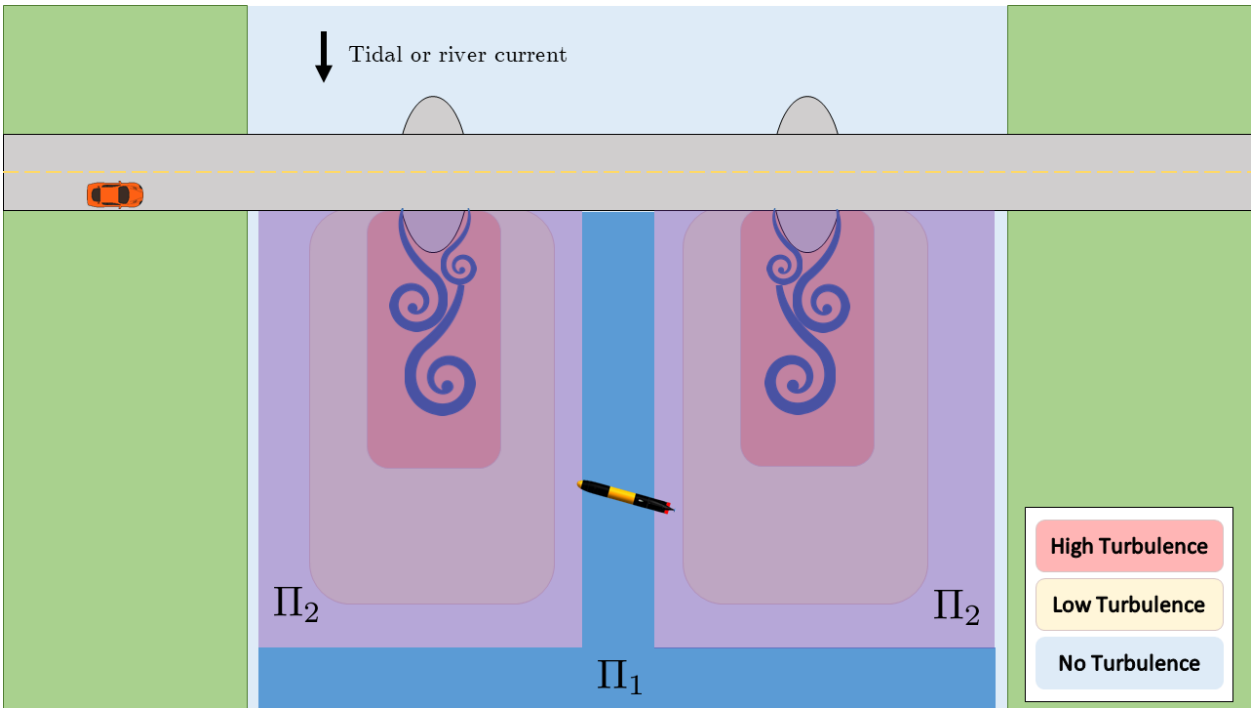

Figure 6.3: Prior map of location based transition probability areas of turbulence near a bridge.

For our example, we explore the three different detector performances

$$\mathbf{A}_1 = \begin{bmatrix} 1.0 & 0.0 \\ 0.0 & 1.0 \end{bmatrix}, \qquad \mathbf{A}_2 = \begin{bmatrix} 0.9 & 0.1 \\ 0.1 & 0.9 \end{bmatrix}, \qquad \mathbf{A}_3 = \begin{bmatrix} 0.9 & 0.1 \\ 0.3 & 0.7 \end{bmatrix}. \tag{6.35}$$

The detector performance $\mathbf{A}_1$ assumes that the detector, the prior map, is perfect while $\mathbf{A}_2$ and $\mathbf{A}_3$ assume the detector is imperfect. For our numerical simulation, we assume that the finite set of transition probabilities are given by

$$\Pi(\varphi(k) = 1) = \begin{bmatrix} 0.9 & 0.1 \\ 0.9 & 0.1 \end{bmatrix}, \qquad \Pi(\varphi(k) = 2) = \begin{bmatrix} 0.1 & 0.9 \\ 0.1 & 0.9 \end{bmatrix}. \tag{6.36}$$

Note that when $\varphi(k) = 1$ the scheduling parameter is more likely to be in the state with no disturbances while $\varphi(k) = 2$ indicates a higher likelihood to be in a state with disturbances.

From the prior map, we generate a location based map of transition probability matrices in Figure 6.3.

Suppose that the simplified continuous-time, open-loop AUV pitch-axis dynamics can be modeled as

$$\begin{bmatrix} \dot{q}(t) \\ \dot{\theta}(t) \end{bmatrix} = \begin{bmatrix} a_{11} & a_{12} \\ 1 & 0 \end{bmatrix} \begin{bmatrix} q(t) \\ \theta(t) \end{bmatrix} + \begin{bmatrix} b_{11} \\ 0 \end{bmatrix} \delta_e(t) + \begin{bmatrix} 0 & 0 & d_q[\vartheta(t)-1] \\ 0 & 0 & 0 \end{bmatrix} w(t) \tag{6.37}$$

where q is vehicle pitch rate, θ is vehicle pitch angle, δ_e is elevator deflection angle, and d_q is scaling for pitch rate disturbances. When the scheduling parameter $\vartheta(t) = 1$, the AUV does not experience pitch rate disturbances, and when the scheduling parameter $\vartheta(t) = 2$, the AUV experiences pitch rate disturbances. The open-loop system (6.37) is discretized using a zero-order hold on the inputs and a sampling time of 0.02 s. The performance error output is

$$z(k) = \begin{bmatrix} \beta_q & 0 \\ 0 & \beta_\theta \\ 0 & 0 \end{bmatrix} \begin{bmatrix} q(k) \\ \theta(k) \end{bmatrix} + \begin{bmatrix} 0 \\ 0 \\ 1 \end{bmatrix} u(k) \tag{6.38}$$

where β_q and β_θ are the relative weights on pitch rate and pitch angle, respectively, and $u(k)$ is the discretized control signal $\delta_e(t)$. The control input is included in the performance error output to penalize control effort. The measurement output equation is

$$y(k) = \begin{bmatrix} 1 & 0 \\ 0 & 1 \end{bmatrix} \begin{bmatrix} q(k) \\ \theta(k) \end{bmatrix} + \begin{bmatrix} \eta_q & 0 & 0 \\ 0 & \eta_\theta & 0 \end{bmatrix} w(k) \tag{6.39}$$

where η_q and η_θ are the measurement noise weights and $w(k) = [w_1(k)\ w_2(k)\ w_3(k)]^\mathsf{T}$ where $w_3(k)$ represents the pitch rate disturbance.

Table 6.1: Parameter values for the simplified AUV pitch system

Parameter	Value
a_{11}	-0.336
a_{12}	-0.060
b_{11}	-0.594
d_q	0.150
β_q	1.000
β_θ	10.000
η_q	0.025
η_θ	0.050

A detector-independent robust output-feedback controller is given by

$$\begin{bmatrix} \hat{x}(k+1) \\ u(k) \end{bmatrix} = \begin{bmatrix} \hat{A} & \hat{B} \\ \hat{C} & \hat{D} \end{bmatrix} \begin{bmatrix} \hat{x}(k) \\ y(k) \end{bmatrix} \tag{6.40}$$

where the controller matrices $\{\hat{A}, \hat{B}, \hat{C}, \hat{D}\}$ are constant. In this numerical simulation, we consider a detector-independent robust controller (6.40), three detector-dependent robust controllers (6.3) where $M = 0$, and three receding horizon detector-dependent controllers (6.3) where $M = 8$. All detector-dependent controllers are designed with a single detector performance (6.35). For this work, YALMIP [41] is used with MOSEK [3] to solve the feasibility problem. Using Theorem 6.5 and the parameters from Table 6.1, seven controllers are synthesized with an H_∞ norm of $\gamma = 0.6$. Seven different closed-loop systems are constructed using one of the seven controllers.

A simulation of each closed-loop system is performed 10,000 times, where

- each simulation is 200 time steps,
- $w(k)$ is sampled from a continuous uniform distribution on the interval $(-1, 1)$,
- $\varphi(k)$ is sampled from a discrete uniform distribution $\{1, 2\}$,
- $x(0) = [-10.0\frac{\pi}{180}\ 10.0\frac{\pi}{180}]^\mathsf{T}$,

Table 6.2: Gains for all closed-loop systems where the detector performance and receding horizon length are specified.

Quantity	Detector-independent	$\mathbf{A}_1$ $M=0$	$\mathbf{A}_2$ $M=0$	$\mathbf{A}_3$ $M=0$	$\mathbf{A}_1$ $M=8$	$\mathbf{A}_2$ $M=8$	$\mathbf{A}_3$ $M=8$
$\frac{\left(\text{mean}\left(\sum_{k=0}^{200} z^{\mathsf{T}}(k)z(k)\right)\right)^{1/2}}{\left(\text{mean}\left(\sum_{k=0}^{200} w^{\mathsf{T}}(k)w(k)\right)\right)^{1/2}}$	0.5609	0.5599	0.5598	0.5746	0.5541	0.5542	0.5634
$\max \frac{\left(\sum_{k=0}^{200} z^{\mathsf{T}}(k)z(k)\right)^{1/2}}{\left(\sum_{k=0}^{200} w^{\mathsf{T}}(k)w(k)\right)^{1/2}}$	0.6039	0.6029	0.6026	0.6238	0.5941	0.5941	0.6127

- $\vartheta(0) = 1$,
- $\hat{\vartheta}(0) = 1$,
- $\vartheta(k)$ is sampled from the appropriate transition probability matrix Π,
- and $\hat{\vartheta}(k)$ is sampled from the appropriate detector matrix $\mathbf{A}$.

For each simulation, the same realizations for w, φ, ϑ, and $\hat{\vartheta}$ are applied to each closed-loop system. Table 6.2 shows the average and maximum gains from the disturbance input to the error output for all controllers where the gain from disturbance input w to error output z is

$$\frac{\left(\sum_{k=0}^{200} z^{\mathsf{T}}(k)z(k)\right)^{1/2}}{\left(\sum_{k=0}^{200} w^{\mathsf{T}}(k)w(k)\right)^{1/2}}. \tag{6.41}$$

From Table 6.2, the average gains for controllers with a detector performance described by $\mathbf{A}_1$ or $\mathbf{A}_2$ are smaller than the detector-independent controller. In situations with good detector performance, a detector-dependent controller may be employed to achieve a smaller average gain. However, the detector-independent controller has a smaller average or max gain when compared to controllers with a detector performance characterized by $\mathbf{A}_3$. In situations where the detector performance is very poor and it is difficult to estimate the state of the Markov chain, a detector-independent controller may be preferred. Figure 6.4 and Figure 6.5 show steady state plots and state response to non-zero initial conditions for a detector-independent and receding horizon detector-dependent controller, respectively.

6.6 Conclusions

Sufficient conditions to analyze and synthesize receding horizon H_∞ controllers for time-inhomogeneous discrete-time MJLS with partial observations of the Markov chain are provided in this chapter. The conditions are a set of linear matrix inequalities that can be efficiently solved.

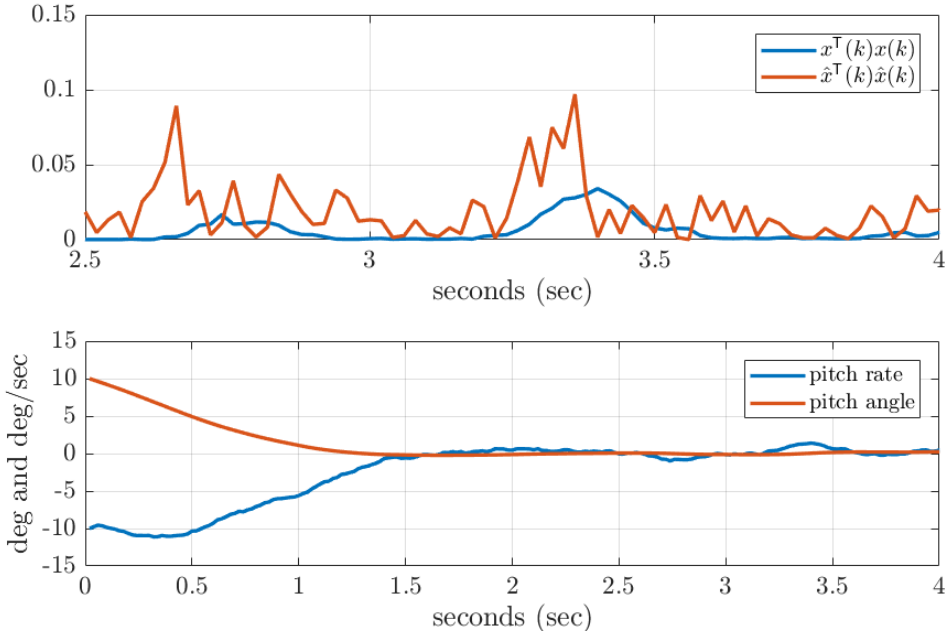

Figure 6.4: Steady state plots of $x^\mathsf{T}(k)x(k)$ and $\hat{x}^\mathsf{T}(k)\hat{x}(k)$ (top) and state response to non-zero initial conditions (bottom) using a detector-independent controller (6.40).

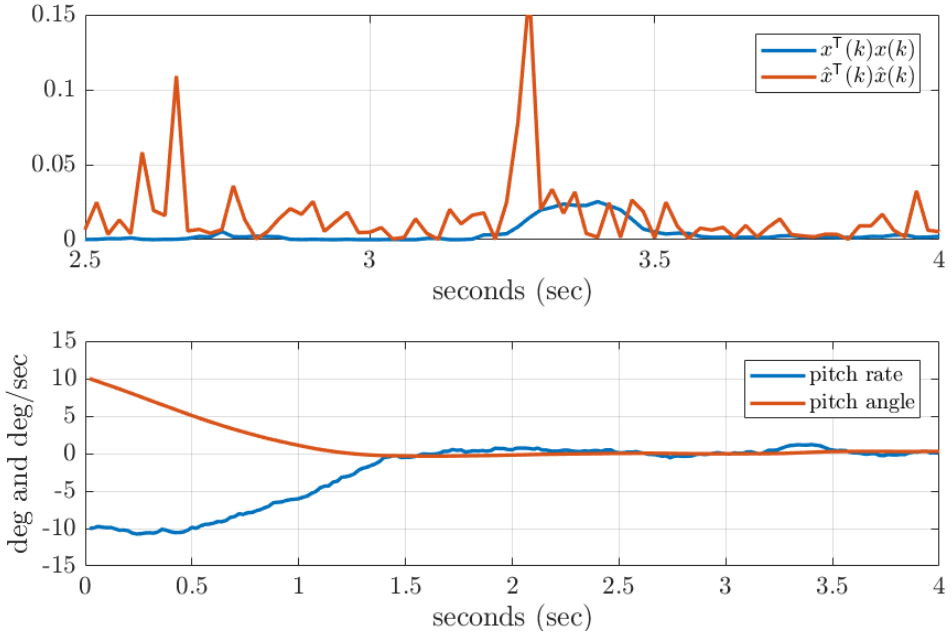

Figure 6.5: Steady state plots of $x^\mathsf{T}(k)x(k)$ and $\hat{x}^\mathsf{T}(k)\hat{x}(k)$ (top) and state response to non-zero initial conditions (bottom) using an $M = 8$ receding horizon controller (6.3) with a detector performance of $\mathbf{A}_3$.

Chapter 7

Conclusion and Future Work

In this dissertation, we address the dynamic modeling and robust control of AUVs. We analyze various hydrodynamic parameter models using experimental data from multiple AUVs. We show that for vehicle velocity estimation the least-squares and adaptive identifier methods produce similar results and either method is a suitable estimation technique. We conclude that the McFarland-Whitcomb and Gertler-Hagen hydrodynamic damping models give the most accurate velocity predictions for the data sets analyzed in this work but have the most number of model coefficients. The linear damping model, with significantly fewer model coefficients than the McFarland-Whitcomb and Gertler-Hagen models, performs well and can be a compromise between model complexity and accuracy. By assessing the velocity error of the simple control surface model and the high-fidelity DSSP tool, we show that a relatively simple control surface model sufficiently describes the vehicle velocity.

We derive several dynamic models for the TRSMAUV employing varying sets of simplifying assumptions. We experimentally assess the efficacy of invoking typical assumptions to simplify the equations of motion. Using data acquired during field trials, we confirm that conventional simplifying model assumptions used for torpedo-shaped AUVs are appropriate for the non-traditionally shaped TRSMAUV performing decoupled motions in the dive plane or steering plane. Future work includes performing multiple identification maneuvers, investigating model performance for coupled motion, and designing improved controllers from the identified dynamic models.

For the case of designing robust controllers, the loop-shaping design procedure presented

in this work provides a way to produce stabilizing robust H_∞ attitude controllers for AUVs using classical loop-shaping techniques. We confirm through our results that a controller with a lower bandwidth reduces actuator movement compared to a controller with a higher bandwidth. The experimental results also show the trade-off between reference tracking performance and control effort.

We present a novel receding horizon H_∞ control algorithm to improve the control of autonomous vehicle systems working in high-disturbance environments. We address stability analysis and control synthesis for time-inhomogeneous Markov jump linear systems with partial observations of the Markov chain where the Markov parameter transition probabilities are non-stationary. We use a detector-based approach to formally guarantee stability and expected l_2 performance where the Markov chain state or scheduling parameter is indirectly measured through a detector. We present a new Bounded Real Lemma for stability analysis and an output feedback H_∞ control synthesis algorithm expressed as a finite set of linear matrix inequalities that can be efficiently solved.

The theory presented in Chapter 6 depends on a detector to estimate the state of the Markov chain. Instead of assuming that a prior map of the Markov states is given, future work could include the design of a suitable disturbance detector with guarantees on performance that can be used with the synthesis algorithm presented in Theorem 6.5. Additionally, sufficient conditions on a time-varying detector performance would lead to a generalization of the Bounded Real Lemma and control synthesis algorithm presented herein. Future work also includes the online estimation or generation of the transition probability distributions which would be useful in scenarios where prior statistical disturbance information is unavailable.

Bibliography

[1] Samir Aberkane. Bounded real lemma for nonhomogeneous Markovian jump linear systems. In *2011 50th IEEE Conference on Decision and Control and European Control Conference*, pages 4692–4697, Dec 2011. doi: 10.1109/CDC.2011.6160918.

[2] Kamil H. M. Ali and Othman Karim. Simulation of flow around piers. *Journal of Hydraulic Research*, 40(2):161–174, 2002. doi: 10.1080/00221680209499859.

[3] MOSEK ApS. *MOSEK Optimization Toolbox for MATLAB 8.1.0.38*, 2015. URL https://docs.mosek.com/8.1/toolbox/index.html.

[4] Haider N. Arafat, Daniel J. Stilwell, and Wayne L. Neu. Development of a dynamic model of a small high-speed autonomous underwater vehicle. In *OCEANS 2006*, pages 1–6, Sept 2006. doi: 10.1109/OCEANS.2006.306895.

[5] Randal W. Beard and Timothy W. McLain. *Small Unmanned Aircraft - Theory and Practice*. Princeton University Press, 2012. ISBN 978-0-691-14921-9. URL https://app.knovel.com/hotlink/toc/id:kpSUATP001/small-unmanned-aircraft/small-unmanned-aircraft.

[6] Dennis S. Bernstein. *Matrix mathematics: Theory, facts, and formulas with application to linear systems theory*, volume 41. Princeton University Press Princeton, 2005.

[7] Eduardo F. Camacho and Carlos Bordons Alba. *Model predictive control*. Springer Science & Business Media, 2013.

[8] Ryan Geoffrey Coe. *Improved Underwater Vehicle Control and Maneuvering Analysis*

with Computational Fluid Dynamics Simulations. PhD thesis, Virginia Polytechnic Institute and State University, Blacksburg, Virginia, 2013.

[9] John P. Comstock. *Principles of naval architecture*. Society of Naval Architects and Marine Engineers, 1967.

[10] Roberto Cristi and Anthony J. Healey. Adaptive identification and control of an autonomous underwater vehicle. In *Proceedings of the 6th International Symposium on Unmanned Untethered Submersible Technology,*, pages 563–572, Jun 1989. doi: 10.1109/UUST.1989.754748.

[11] Roberto Cristi, Fotis A. Papoulias, and Anthony J. Healey. Adaptive sliding mode control of autonomous underwater vehicles in the dive plane. *IEEE Journal of Oceanic Engineering*, 15(3):152–160, Jul 1990. ISSN 0364-9059. doi: 10.1109/48.107143.

[12] André Marcorin de Oliveira and Oswaldo Luiz do Valle Costa. Mixed H_2/H_∞ control of hidden Markov jump systems. *International Journal of Robust and Nonlinear Control*, 28(4):1261–1280, 2018. ISSN 1099-1239. doi: 10.1002/rnc.3952.

[13] Carlos E. de Souza, Alexandre Trofino, and Karina A. Barbosa. Mode-independent H_∞ filters for Markovian jump linear systems. *IEEE Transactions on Automatic Control*, 51(11):1837–1841, Nov 2006. ISSN 0018-9286. doi: 10.1109/TAC.2006.883060.

[14] Jean G. Dessureault and Donald J. Belliveau. A trawl-proof housing for bottom mounted instruments. In *OCEANS '87*, pages 658–660, Sept 1987. doi: 10.1109/OCEANS.1987.1160829.

[15] Jean G. Dessureault, Donald J. Belliveau, and Scott W. Young. Design and tests of a trawl-resistant package for an acoustic doppler current profiler. *IEEE Journal of Oceanic Engineering*, 16(4):397–401, Oct 1991. ISSN 0364-9059. doi: 10.1109/48.90904.

[16] Oswaldo Luiz do Valle Costa, Marcelo D. Fragoso, and Ricardo P. Marques. *Discrete-time Markov jump linear systems*. Springer Science & Business Media, 2006.

[17] Oswaldo Luiz do Valle Costa, Marcelo D. Fragoso, and Marcos Garcia Todorov. A detector-based approach for the H_2 control of Markov jump linear systems with partial information. *IEEE Transactions on Automatic Control*, 60(5):1219–1234, May 2015. ISSN 0018-9286. doi: 10.1109/TAC.2014.2366253.

[18] Richard S. Duelley. Autonomous underwater vehicle propulsion design. Master's thesis, Virginia Polytechnic Institute and State University, Blacksburg, Virginia, 2010.

[19] Geir E. Dullerud and Fernando Paganini. *A course in robust control theory: a convex approach*, volume 36. Springer Science & Business Media, 2013.

[20] Ray Essick, Ji-Woong Lee, and Geir E. Dullerud. An exact convex solution to receding horizon control. In *2012 American Control Conference (ACC)*, pages 5955–5960, June 2012. doi: 10.1109/ACC.2012.6315646.

[21] Ray Essick, Ji-Woong Lee, and Geir E. Dullerud. Control of linear switched systems with receding horizon modal information. *IEEE Transactions on Automatic Control*, 59(9):2340–2352, Sept 2014. ISSN 0018-9286. doi: 10.1109/TAC.2014.2321251.

[22] Zhengping Feng and Robert Allen. Reduced order H_∞ control of an autonomous underwater vehicle . *Control Engineering Practice*, 12(12):1511–1520, 2004.

[23] Thor I. Fossen. *Guidance and control of ocean vehicles*. Wiley, Chichester; New York, 1994. ISBN 9780471941132; 0471941131.

[24] Pascal Gahinet and Pierre Apkarian. A linear matrix inequality approach to H_∞ control. *International Journal of Robust and Nonlinear Control*, 4(4):421–448, 1994. ISSN 1099-1239. doi: 10.1002/rnc.4590040403.

[25] José C. Geromel, Alim P. C. Gonçalves, and André R. Fioravanti. Dynamic output feedback control of discrete-time Markov jump linear systems through linear matrix inequalities. *SIAM Journal on Control and Optimization*, 48(2):573–593, 2009.

[26] Morton Gertler and Grant R. Hagen. Standard equations of motion for submarine simulation. Technical report, DTIC Document, 1967.

[27] Scott B. Gibson, Brian McCarter, Daniel J. Stilwell, and Wayne L. Neu. A comparison of hydrodynamic damping models using least-squares and adaptive identifier methods for autonomous underwater vehicles. In *OCEANS 2015 - MTS/IEEE Washington*, pages 1–7, Oct 2015.

[28] Keith Glover and Duncan McFarlane. Robust stabilization of normalized coprime factor plant descriptions with H_∞-bounded uncertainty. *IEEE Transactions on Automatic Control*, 34(8):821–830, Aug 1989. ISSN 0018-9286. doi: 10.1109/9.29424.

[29] D. J. Hoyle, Richard A. Hyde, and David J. N. Limebeer. An H_∞ approach to two degree of freedom design. In *Decision and Control, 1991., Proceedings of the 30th IEEE Conference on*, pages 1581–1585 vol.2, Dec 1991. doi: 10.1109/CDC.1991.261671.

[30] Wenrui Huang, Qiping Yang, and Hong Xiao. CFD modeling of scale effects on turbulence flow and scour around bridge piers. *Computers and Fluids*, 38(5):1050 – 1058, 2009. ISSN 0045-7930. doi: https://doi.org/10.1016/j.compfluid.2008.01.029. URL http://www.sciencedirect.com/science/article/pii/S0045793008000704. Advances in Computational Fluid Dynamics.

[31] D. E. Humphreys and K. W. Watkinson. Prediction of acceleration hydrodynamic coefficients for underwater vehicles from geometric parameters. Technical report, DTIC Document, 1978.

[32] Richard A. Hyde and Keith Glover. The application of scheduled H_∞ controllers to a VSTOL aircraft. *IEEE Transactions on Automatic Control*, 38(7):1021–1039, Jul 1993. ISSN 0018-9286. doi: 10.1109/9.231458.

[33] Pablo A. Iglesias and Thomas J. Urban. Loop Shaping Design for Missile Autopilots: Controller Configurations and Weighting Filter Selection. *Journal of Guidance, Control, and Dynamics*, 23(3):516–525, 2000. ISSN 0731-5090. doi: 10.2514/2.4558.

[34] Frederick H. Imlay. The complete expressions for added mass of a rigid body moving in an ideal fluid. Technical report, DTIC Document, 1961.

[35] Petros A. Ioannou and Jing Sun. *Robust adaptive control*. PTR Prentice-Hall, 1996.

[36] Issac Kaminer, António M. Pascoal, Carlos J. Silvestre, and Pramod P. Khargonekar. Control of an underwater vehicle using H_∞ synthesis. In *Decision and Control, 1991., Proceedings of the 30th IEEE Conference on*, pages 2350–2355 vol.3, Dec 1991. doi: 10.1109/CDC.1991.261601.

[37] Hassan K. Khalil. Noninear systems. *Prentice-Hall, New Jersey*, 2(5):5–1, 1996.

[38] Jeffrey C. Lagarias, James A. Reeds, Margaret H. Wright, and Paul E. Wright. Convergence properties of the nelder–mead simplex method in low dimensions. *SIAM Journal on Optimization*, 9(1):112–147, 1998. doi: 10.1137/S1052623496303470.

[39] Ji-Woong Lee and Geir E. Dullerud. Uniform stabilization of discrete-time switched and Markovian jump linear systems. *Automatica*, 42(2):205 – 218, 2006. ISSN 0005-1098. doi: https://doi.org/10.1016/j.automatica.2005.08.019.

[40] David J. N. Limebeer, Ebrahim M. Kasenally, and John D. Perkins. On the design of robust two degree of freedom controllers. *Automatica*, 29(1):157–168, Jan 1993. doi: 10.1016/0005-1098(93)90179-W.

[41] Johan Löfberg. YALMIP : A toolbox for modeling and optimization in MATLAB. In *In Proceedings of the CACSD Conference*, Taipei, Taiwan, 2004. URL https://yalmip.github.io/download/.

[42] Cedric L. Logan. A comparison between H-infinity/Mu-synthesis control and sliding-mode control for robust control of a small autonomous underwater vehicle. In *Autonomous Underwater Vehicle Technology, 1994. AUV '94., Proceedings of the 1994 Symposium on*, pages 399–416, Jul 1994. doi: 10.1109/AUV.1994.518653.

[43] Collin C. Lutz. *Switched Markov Jump Linear Systems: Analysis and Control Synthesis*. PhD thesis, Virginia Polytechnic Institute and State University, Blacksburg, Virginia, 2014.

[44] Collin C. Lutz and Daniel J. Stilwell. Stability and disturbance attenuation for Markov jump linear systems with time-varying transition probabilities. *IEEE Transactions on Automatic Control*, 61(5):1413–1418, May 2016. ISSN 0018-9286. doi: 10.1109/TAC.2015.2476196.

[45] Michael Mackay. Dssp50 build 090910 documentation, part 1: Guide and tutorial. Technical report, DRDC Atlantic TM 2009-226, 2009.

[46] Brian McCarter, Stephen Portner, Wayne L. Neu, Daniel J. Stilwell, Dexter Malley, and Jason Mims. Design elements of a small AUV for bathymetric surveys. In *Autonomous Underwater Vehicles (AUV), 2014 IEEE/OES*, pages 1–5. IEEE, 2014.

[47] Brian Raymond McCarter. Experimental evaluation of viscous hydrodynamic force models for autonomous underwater vehicles. Master's thesis, Virginia Polytechnic Institute and State University, Blacksburg, Virginia, 2014.

[48] Christopher J. McFarland and Louis L. Whitcomb. Comparative experimental evaluation of a new adaptive identifier for underwater vehicles. In *Robotics and Automation (ICRA), 2013 IEEE International Conference on*, pages 4614–4620, May 2013. doi: 10.1109/ICRA.2013.6631233.

[49] Duncan McFarlane and Keith Glover. A loop-shaping design procedure using H_∞ synthesis. *IEEE Transactions on Automatic Control*, 37(6):759–769, Jun 1992. ISSN 0018-9286. doi: 10.1109/9.256330.

[50] Bruce W. Melville and Arved J. Raudkivi. Flow characteristics in local scour at bridge piers. *Journal of Hydraulic Research*, 15(4):373–380, 1977. doi: 10.1080/00221687709499641.

[51] Jan Petrich. *Improved Guidance, Navigation, and Control for Autonomous Underwater Vehicles: Theory and Experiment*. PhD thesis, Virginia Polytechnic Institute and State University, Blacksburg, Virginia, 2009.

[52] Jan Petrich and Daniel J. Stilwell. Model simplification for AUV pitch-axis control design. *Ocean Engineering*, 37(7):638 – 651, 2010. ISSN 0029-8018.

[53] Jan Petrich and Daniel J. Stilwell. Robust control for an autonomous underwater vehicle that suppresses pitch and yaw coupling. *Ocean Engineering*, 38(1):197–204, 2011.

[54] Jan Petrich, Wayne L. Neu, and Daniel J. Stilwell. Identification of a simplified AUV pitch axis model for control design: Theory and experiments. In *OCEANS 2007*, pages 1–7, Sept 2007. doi: 10.1109/OCEANS.2007.4449350.

[55] Stephen Michael Portner. Design of a low reynolds number propulsion system for an autonomous underwater vehicle. Master's thesis, Virginia Polytechnic Institute and State University, Blacksburg, Virginia, 2014.

[56] Timothy Prestero. Development of a six-degree of freedom simulation model for the REMUS autonomous underwater vehicle. In *OCEANS, 2001. MTS/IEEE Conference and Exhibition*, volume 1, pages 450–455. IEEE, 2001.

[57] Timothy Jason Prestero. Verification of a six-degree of freedom simulation model for the REMUS autonomous underwater vehicle. Master's thesis, Massachusetts institute of technology, 2001.

[58] J. Anthony Rossiter. *Model-based predictive control: a practical approach*. CRC press, 2003.

[59] Peter Seiler and Raja Sengupta. A bounded real lemma for jump systems. *IEEE Transactions on Automatic Control*, 48(9):1651–1654, Sept 2003. ISSN 0018-9286. doi: 10.1109/TAC.2003.817010.

[60] I. Sharf, M. Nahon, A. Harmat, W. Khan, M. Michini, N. Speal, M. Trentini, T. Tsadok, and T. Wang. Ground effect experiments and model validation with draganflyer x8 rotorcraft. In *2014 International Conference on Unmanned Aircraft Systems (ICUAS)*, pages 1158–1166, May 2014. doi: 10.1109/ICUAS.2014.6842370.

[61] Shaojie Shen, Nathan Michael, and Vijay Kumar. Obtaining liftoff indoors: Autonomous navigation in confined indoor environments. *IEEE Robotics Automation Magazine*, 20(4):40–48, Dec 2013. ISSN 1070-9932. doi: 10.1109/MRA.2013.2253172.

[62] Carlos Silvestre and António Pascoal. Control of an AUV in the vertical and horizontal planes: system design and tests at sea. *Transactions of the Institute of Measurement and Control*, 19(3):126–138, 1997. doi: 10.1177/014233129701900303.

[63] Sigurd Skogestad and Ian Postlethwaite. *Multivariable feedback control: anal-*

ysis and design. John Wiley, Hoboken, NJ, 2nd edition, 2005. ISBN 047001167X;9780470011676;0470011688;9780470011683;.

[64] Vahram Stepanyan, Naira Hovakimyan, and Craig A. Woolsey. Adaptive output feedback control of a spheroidal underactuated underwater vehicle. In *Proceedings of OCEANS 2005 MTS/IEEE*, pages 278–284 Vol. 1, Sept 2005. doi: 10.1109/OCEANS.2005.1639776.

[65] Marcos Garcia Todorov, Marcelo D. Fragoso, and Oswaldo Luiz do Valle Costa. A new approach for the H_∞ control of Markov jump linear systems with partial information. In *2015 54th IEEE Conference on Decision and Control (CDC)*, pages 3592–3597, Dec 2015. doi: 10.1109/CDC.2015.7402775.

[66] Cyrille Vuilmet. High order sliding mode control applied to a heavyweight torpedo. In *Proceedings of 2005 IEEE Conference on Control Applications, 2005. CCA 2005.*, pages 61–66, Aug 2005. doi: 10.1109/CCA.2005.1507101.

[67] B. A. White, J. King, Y. Patel, and B. A. Stacey. Robust Control Design of an ROV. In *1995 European Control Conference, September 5 - September 8, Roma, Italy*, 1995.

[68] Taylor Boyde Wilson. Mechanical design of a trawl-resistant self-mooring autonomous underwater vehicle. Master's thesis, Virginia Polytechnic Institute and State University, Blacksburg, Virginia, 2016.

[69] Dana R. Yoerger, John G. Cooke, and Jean J. E. Slotine. The influence of thruster dynamics on underwater vehicle behavior and their incorporation into control system design. *IEEE Journal of Oceanic Engineering*, 15(3):167–178, Jul 1990. ISSN 0364-9059. doi: 10.1109/48.107145.

Appendices

Appendix A

690 AUV and 690S AUV Model Parameters

Table A.1: AUV model parameters

Parameter	Description	690 Value	690S Value	Unit
d	diameter	0.175	0.175	m
m	mass	41.5	27.5	kg
∇	displacement	41.7	28.2	kg
l	length	2.1	1.5	m
d_{prop}	propeller diameter	0.12	0.10	m
w	wake fraction	0.3	0.3	

Table A.2: 690 AUV inertia tensor

$$I_{690} = \begin{bmatrix} 0.17 & 0.00 & 0.14 \\ 0.00 & 10.37 & 0.00 \\ 0.14 & 0.00 & 10.35 \end{bmatrix}$$

Table A.3: 690S AUV inertia tensor

$$I_{690S} = \begin{bmatrix} 0.09 & -0.04 & -0.01 \\ -0.04 & 4.49 & 0.00 \\ -0.01 & 0.00 & 4.50 \end{bmatrix}$$

Table A.4: Added mass model for a prolate spheroid with same volume and aspect ratios as the 690 AUV.

$$M_{a_{690}} = \text{diag}([0.67\ 40.17\ 40.17\ 0.0\ 8.02\ 8.02])$$

Table A.5: Added mass model for a prolate spheroid with same volume and aspect ratios as the 690S AUV.

$$M_{a_{690S}} = \text{diag}([0.63\ 23.48\ 23.48\ 0.0\ 2.53\ 2.53])$$

Table A.6: 690 AUV propeller model equations where J is the advance ratio.

$$K_{T_{690}} = -0.07J^2 - 0.13J + 0.10$$
$$K_{Q_{690}} = -0.02J^2 + 0.01J + 0.00$$

Table A.7: 690S AUV propeller model equations where J is the advance ratio.

$$K_{T_{690S}} = -0.14J^2 - 0.07J + 0.18$$
$$K_{Q_{690S}} = -0.02J^2 + 0.01J + 0.02$$

Table A.8: DSSP control surface model coefficients for the 690 AUV and the 690S AUV.

$$K_\delta = \begin{bmatrix} 0.00000 & 0.00000 & 0.00000 & 0.00000 \\ 0.00000 & 0.00000 & 0.00191 & -0.00207 \\ -0.00208 & 0.00195 & 0.00000 & 0.00000 \\ -0.00002 & -0.00002 & -0.00002 & -0.00002 \\ -0.00108 & 0.00083 & 0.00000 & 0.00000 \\ -0.00001 & 0.00000 & -0.00088 & 0.00097 \end{bmatrix}$$

$$K_{\delta^2} = \begin{bmatrix} -0.00121 & -0.00095 & -0.00092 & -0.00105 \\ 0.00031 & -0.00015 & -0.00016 & -0.00001 \\ -0.00018 & -0.00015 & 0.00025 & -0.00030 \\ 0.00000 & 0.00000 & 0.00000 & 0.00000 \\ 0.00014 & 0.00014 & 0.00012 & -0.00013 \\ -0.00016 & 0.00006 & 0.00004 & 0.00001 \end{bmatrix}$$

Appendix B

Linear State Space AUV Models

B.1 Virginia Tech 690 AUV

The system identification technique presented in [54] is used to generate the 690 AUV system model using a series of zig-zag maneuvers. The linear state space model for the 690 AUV is given by

$$A = \begin{bmatrix} -1000.00 & -48.65 & -8.67 & 0.00 & 0.00 & 0.00 \\ 1.00 & -0.34 & -0.06 & 0.00 & 0.00 & 0.00 \\ 0.00 & 1.00 & 0.00 & 0.00 & 0.00 & 0.00 \\ 0.00 & 0.00 & 0.00 & -1000.00 & -48.65 & -8.67 \\ 0.00 & 0.00 & 0.00 & 1.00 & -0.34 & 0.00 \\ 0.00 & 0.00 & 0.00 & 0.00 & 1.00 & 0.00 \end{bmatrix}, \quad B = \begin{bmatrix} -0.10 & 0.00 \\ -0.59 & 0.00 \\ 0.00 & 0.00 \\ 0.00 & -0.10 \\ 0.00 & -0.59 \\ 0.00 & 0.00 \end{bmatrix}, \tag{B.1a}$$

$$C = \begin{bmatrix} 0.00 & 1.00 & 0.00 & 0.00 & 0.00 & 0.00 \\ 0.00 & 0.00 & 1.00 & 0.00 & 0.00 & 0.00 \\ 0.00 & 0.00 & 0.00 & 0.00 & 1.00 & 0.00 \\ 0.00 & 0.00 & 0.00 & 0.00 & 0.00 & 1.00 \end{bmatrix}, \qquad D = \begin{bmatrix} 0.00 & 0.00 \\ 0.00 & 0.00 \\ 0.00 & 0.00 \\ 0.00 & 0.00 \end{bmatrix}, \tag{B.1b}$$

where the state vector is $x = [\alpha, q, \theta, \beta, r, \psi]^\mathsf{T}$, the control input vector is $u = [\delta_e \ \delta_r]^\mathsf{T}$, the measurements are $y = [q \ \theta \ r \ \psi]^\mathsf{T}$, the elevator deflection is δ_e, the rudder deflection is δ_r, the AUV body pitch rate is q, the AUV pitch angle is θ, the AUV body yaw rate is r, and the AUV heading or yaw angle is ψ. The 690 state space model (B.1) is in units of degrees

and degrees/second.

B.2 Virginia Tech 690S AUV

The linear state space model for the 690S AUV is given by

$$A = \begin{bmatrix} 0.43 & -0.38 & -0.31 & 0.00 & 0.00 & 0.00 \\ 1.00 & -1.76 & -0.53 & 0.00 & 0.00 & 0.00 \\ 0.00 & 1.00 & 0.00 & 0.00 & 0.00 & 0.00 \\ 0.00 & 0.00 & 0.00 & 0.43 & -0.38 & -0.31 \\ 0.00 & 0.00 & 0.00 & 1.00 & -1.76 & 0.00 \\ 0.00 & 0.00 & 0.00 & 0.00 & 1.00 & 0.00 \end{bmatrix}, \quad B = \begin{bmatrix} -0.59 & 0.00 \\ -0.77 & 0.00 \\ 0.00 & 0.00 \\ 0.00 & -0.59 \\ 0.00 & -0.77 \\ 0.00 & 0.00 \end{bmatrix}, \tag{B.2a}$$

$$C = \begin{bmatrix} 0.00 & 1.00 & 0.00 & 0.00 & 0.00 & 0.00 \\ 0.00 & 0.00 & 1.00 & 0.00 & 0.00 & 0.00 \\ 0.00 & 0.00 & 0.00 & 0.00 & 1.00 & 0.00 \\ 0.00 & 0.00 & 0.00 & 0.00 & 0.00 & 1.00 \end{bmatrix}, \quad D = \begin{bmatrix} 0.00 & 0.00 \\ 0.00 & 0.00 \\ 0.00 & 0.00 \\ 0.00 & 0.00 \end{bmatrix}. \tag{B.2b}$$

The 690S state space model (B.2) is in units of degrees and degrees/second.